Doctoral Dissertation

博士論文

Spectroscopic study of epsilon iron oxide nanoparticles in the millimeter- and terahertz-wave regions

（イプシロン酸化鉄ナノ粒子のミリ波および
テラヘルツ波領域の分光学的研究）

Marie Yoshikiyo

吉清　まりえ

Abstract

ε-Fe_2O_3 is a magnetic material that is now attracting worldwide attention due to its large magnetic anisotropy. The magnetic anisotropy of ε-Fe_2O_3 could be controlled by metal substitution. In this thesis, I studied the spectroscopic properties of ε-Fe_2O_3 and its metal-substituted series (ε-$M_xFe_{2-x}O_3$) in a wide frequency range from millimeter-wave to terahertz-wave region (30 GHz – 30 THz) using terahertz time-domain spectroscopy (THz-TDS), far-infrared (far-IR) spectroscopy, and Raman spectroscopy. To understand the obtained spectroscopic data, first-principles periodic calculations and phonon mode calculations were also performed.

Chapter 1 shows the background of this thesis. Especially, the magnetic properties including the huge coercive field of ε-Fe_2O_3 and its mechanism is described. In chapters 2 and 3, the lattice vibration of ε-Fe_2O_3 in the low frequency region is described. Phonon mode calculation showed the frequencies of the optical phonon modes of ε-Fe_2O_3. The calculated spectrum well reproduced the far-IR spectrum. Phonon mode calculation of ε-$Ga_{0.5}Fe_{1.5}O_3$ was also carried out. Far-IR, mid-IR, and Raman spectra of ε-$Ga_{0.48}Fe_{1.52}O_3$ showed good agreement with the spectra obtained by the first-principles phonon mode calculations. In addition, a magnetically oriented film of ε-$Ga_{0.45}Fe_{1.55}O_3$ was prepared to investigate the relation between the crystallographic direction and the magnetic anisotropy. The film showed a high degree of orientation of the crystallographic *a*-axis, exhibiting a rectangular magnetic hysteresis loop. In chapters 4 and 5, from the viewpoint of zero-field ferromagnetic resonance, indium-substituted ε-Fe_2O_3 (ε-$In_xFe_{2-x}O_3$) nanoparticles were prepared. From the results of the X-ray diffraction (XRD) measurement, indium ion was found to selectively replace the octahedral Fe_B site among

the four different of iron sites (Fe_A–Fe_D). THz-TDS measurements showed that ε-$In_xFe_{2-x}O_3$ has absorption peaks at 182 GHz (x = 0), 160 GHz (x = 0.04), 143 GHz (x = 0.09), 123 GHz (x = 0.13), and 110 GHz (x = 0.18). Furthermore, to measure millimeter-wave rotation, ε-$Al_{0.47}Fe_{1.53}O_3$, which has an absorption peak at 100 GHz, was synthesized. The magnetic rotational characteristics were measured using wire grid polarizers. The frequency dependence of the rotation angle showed a dispersive spectrum centered at the resonance frequency with a large Faraday rotation performance. In this thesis, I report the spectroscopic properties of ε-Fe_2O_3 and series of ε-$M_xFe_{2-x}O_3$ (M = Ga, In, and Al) in the millimeter-wave and terahertz-wave regions.

Contents

Chapter 1

Introduction

1.1. Background

Red rust is a well known ferric oxide. Ferric oxide is composed of trivalent iron cations Fe^{3+} and oxygen anions O^{2-}, i.e., Fe_2O_3. Red rust, which is called α-Fe_2O_3, has a corundum crystal structure with a space group of $R\,\bar{3}\,c$ and shows weak ferromagnetism.[1.1,1.2] In addition to α-Fe_2O_3, three more phases are known, γ-Fe_2O_3, β-Fe_2O_3, and ε-Fe_2O_3 (Figure 1.1).[1.3–1.6] γ-Fe_2O_3, which has a spinel structure with a space group of $Fd\bar{3}m$, shows ferromagnetic properties, and is used for magnetic fluids for example.[1.7,1.8] γ-Fe_2O_3 and α-Fe_2O_3 are abundant in nature.

ε-Fe_2O_3 and β-Fe_2O_3 are artificially prepared in the laboratory. In 2004, Ohkoshi et al. first synthesized pure ε-Fe_2O_3 phase using a combination method of reverse-micelle and sol-gel techniques.[1.9–1.12] In nature, γ-Fe_2O_3 phase changes to α-Fe_2O_3 phase when the sintering temperature is increased. However, it was clarified that γ-Fe_2O_3 phase transforms to ε-Fe_2O_3 phase in the case of nanometer size particles of 5–40 nm, and then α-Fe_2O_3 phase appears above 40 nm (Figure 1.2). From the result of the magnetic measurements, ε-Fe_2O_3 was found to exhibit an extremely large coercive field value of 20 kOe at room temperature, which is the largest among metal oxide based magnets.[1.13,1.14] Additionally, ε-Fe_2O_3 shows a spin reorientation phenomenon.[1.15-1.21] Focusing on these unique magnetic properties, various studies such as X-ray magnetic circular dichroism, neutron diffraction, and Mössbauer spectroscopy have been carried out.[1.17–1.30] Furthermore, our group has proposed the industrial application of ε-Fe_2O_3 as

a high-frequency millimeter-wave absorber.[1.31–1.34]

1.2. Epsilon iron oxide (ε-Fe_2O_3)

Since ε-Fe_2O_3 and its analogues are the main topics of this doctoral thesis, the synthetic method, magnetic properties, and millimeter-wave absorption properties are described in this section.

1.2.1 Synthetic methods to obtain ε-Fe_2O_3

A pure ε-Fe_2O_3 was obtained by a wet process via a combination of reverse-micelle and sol–gel methods, using iron nitrate as the starting material.[1.24] Afterwards, a synthesis using mesoporous silica as a template was developed, in which the starting material was iron sulfate or ferrocenecarbaldehyde.[1.5] Furthermore, in 2015, ferrihydride was used as the starting material, and ε-Fe_2O_3 nanoparticles were obtained by the sol-gel method.[1.35] In 2018, a direct method to obtain ε-Fe_2O_3 from magnetite Fe_3O_4 has also been reported.[1.36] Among these synthetic methods, I will detail the synthetic procedure of the combined method of reverse-micelle and sol-gel techniques. To prepare nanometer-sized Fe_2O_3, our group synthesized a ε-Fe_2O_3/SiO_2 composite as follows: reverse-micelle I containing $Fe(NO_3)_3$ (aqueous, (aq.)) and $Ba(NO_3)_2$ aq. solutions was mixed with reverse-micelle II containing NH_4OH aq. solution while stirred rapidly. Then tetraethoxysilane (TEOS) was added into this solution. Finally, the precipitate was sintered in air at three different temperatures (Figure 1.3). The crystal structures of the obtained samples were characterized by X-ray diffraction (XRD) to be γ-Fe_2O_3 (900 ºC sintered), ε-Fe_2O_3 (1000 ºC), and α-Fe_2O_3 (1100 ºC) in SiO_2 (Figure 1.4). Transmission electron microscopy (TEM) image of ε-Fe_2O_3 nanorods is shown in Figure 1.5. The energy dispersive X-ray analysis (EDX) shows Fe_2O_3 surrounded by a silica matrix. The high-resolution TEM

image recorded on an individual nanoparticle shows lattice fringes (Fig. 1.5b). The Fourier transform image confirms that the long axis of the nanorod corresponds to the *a*-axis of the ε-Fe_2O_3 crystal structure.

1.2.2 Thermodynamical mechanism of the ε-Fe_2O_3 formation

In the case of the combined method of reverse-micelle and sol-gel techniques, ε-Fe_2O_3 phase appears between γ-Fe_2O_3 and α-Fe_2O_3, corresponding to a narrow sintering temperature range of 980–1030 °C. From the viewpoint of thermodynamics, the Gibbs energy per volume (G/V) of a system is described as follows:

$$G/V = \mu/V_m + 6s/d \qquad (1.1)$$

, where μ is the chemical potential, V_m is the molar volume, s is the surface energy, and d is the nanoparticle diameter. This equation suggests that G is mainly determined by the chemical potential when the particle size is significantly large, whereas the contribution of the surface energy increases when d is small.[1.37–1.39] When the parameters in Eq. (1.1) satisfy the following relationships: $\mu_\gamma > \mu_\varepsilon > \mu_\alpha$, $s_\gamma < s_\varepsilon < s_\alpha$, and $(s_\varepsilon - s_\gamma)/(s_\alpha - s_\varepsilon) < (\mu_\varepsilon - \mu_\gamma)/(\mu_\alpha - \mu_\varepsilon)$, the Gibbs energy curves of G_γ/V, G_ε/V, and G_α/V intersect (Figure 1.6), and ε-Fe_2O_3 exists as a stable phase within an intermediate d value range. The threshold particle sizes (d_{th}) of γ → ε and ε → α are described by $d_{th}{}^{\gamma \to \varepsilon} = -6V_m(s_\varepsilon - s_\gamma)/(\mu_\varepsilon - \mu_\gamma)$ and $d_{th}{}^{\varepsilon \to \alpha} = -6V_m(s_\alpha - s_\varepsilon)/(\mu_\alpha - \mu_\varepsilon)$, respectively. Therefore, the ε-Fe_2O_3 phase can exist if the size of the Fe_2O_3 particle is $-6v(\sigma_\varepsilon - \sigma_\gamma)/(\mu_\varepsilon - \mu_\gamma) < d < -6v\,(\sigma_\varepsilon - \sigma_\alpha)/(\mu_\varepsilon - \mu_\alpha)$.

1.2.3 Huge coercive field of ε-Fe_2O_3

The magnetization (M) versus external magnetic field (H_{ex}) plots of γ-Fe_2O_3, ε-Fe_2O_3, and α-Fe_2O_3 phases are shown in Figure 1.7. γ-Fe_2O_3 shows superparamagnetism with a blocking temperature of 25 K, while α-Fe_2O_3 shows weak antiferromagnetism.

Conversely, ε-Fe_2O_3 shows a Néel temperature (T_N) of 500 K. The magnetic hysteresis loop indicates that this sample exhibits a surprisingly large H_c value of 20 kOe at room temperature, and the magnetization value at 7 Tesla (T) is 15 emu g^{-1} (15 A m^2 kg^{-1}) for a given mass of ε-Fe_2O_3 (Figure 1.7b). It is noted that a recent work reports the presence of another T_N at 850 K, raising a controversy among scientists.[1.40]

Multiple factors contribute to the gigantic H_c of ε-Fe_2O_3. One is the small ε-Fe_2O_3 crystal size. A large H_c value is expected when the particle size is sufficiently small to form a single magnetic domain.[1.41,1.42] A particle size of less than 50 nm is the suitable size for a single magnetic domain. Another factor is the intrinsic magnetic properties of the ε-Fe_2O_3 phase. The H_c value depends on the magnetocrystalline anisotropy constant (K).[1.43] The K value is estimated to be 7.7×10^6 erg cm^{-3}.[1.35] Therefore, it is considered that the large H_c value of ε-Fe_2O_3 is now considered to be due to (1) the suitable nanoscale size of particles to form a single magnetic domain and (2) the large K value.

As a further investigation of the magnetic anisotropy, the study of a crystallographically oriented ε-Fe_2O_3 film was reported. The XRD pattern of the film shows one sharp peak of (2 0 0) (Figure 1.8a). The crystallographic a-axis (longitudinal direction) of the ε-Fe_2O_3 rod is well oriented along the out-of-plane direction of the film. The magnetic hysteresis loop of the film shows an H_c value of 25.2 kOe along the a-axis at 300 K and a saturation magnetization value of 16.2 emu g^{-1} at 7 T (Figure 1.8b).

Additionally, the particle size dependence of the magnetic properties is also reported. The magnetic hysteresis loops of spherical-shaped ε-Fe_2O_3 nanoparticles of different sizes in random orientation at 300 K are shown in Figure 1.9. The H_c value decreases towards zero with decreasing d as shown in the H_c versus d plot of Figure 1.9b. As references, the particle size dependences of the H_c values of $BaFe_{12}O_{19}$, $SrFe_{12}O_{19}$,

and $CoFe_2O_4$ reported so far are also plotted.

1.3. Electronic structure of ε-Fe_2O_3 by first-principles calculation and molecular orbital calculations

Theoretical calculations of the electronic structure of ε-Fe_2O_3 have been reported.[1.44] Figure 1.11 shows the density of states (DOS) of ε-Fe_2O_3 by first-principles calculations. The occupied and unoccupied Fe3*d* bands are largely split, and the occupied Fe3*d* band has a lower energy compared to the O2*p* band, and the band gap is 1.6 eV between the O2*p* valence band and the Fe3*d* conduction band. From this calculation, ε-Fe_2O_3 is classified as a charge-transfer insulator, not a Mott-Hubbard insulator.[1.45]

The partial DOSs of the four iron sites (Fe_A–Fe_D) are shown in Figure 1.12. Below the E_F level, the 3*d* band of Fe_A is occupied by β spins, that of Fe_B is occupied by α spins, that of Fe_C is occupied by α spins, and that of Fe_D is occupied by β spins. The spin configuration of (Fe_A, Fe_B, Fe_C, Fe_D) = (β, α, α, β) corresponds to the reported collinear ferromagnetic structure with a negative sublattice magnetization at Fe_A site, positive sublattice magnetization at Fe_B site, positive sublattice magnetization at Fe_C site, and negative sublattice magnetization at Fe_D site.[1.19–1.21,1.46]

From the calculation of the band structure of ε-Fe_2O_3, the optical transition of the band gap is assigned as an indirect optical transition of 1.6 eV, i.e., Γ point → *S* point (Figure 1.13). Charge density maps of the bottom of the conduction band and the top of the valence band are shown in Figure 1.14. As an example, Figure 1.15 shows one of the occupied Fe3*d* states. In this state, the electron charge is distributed mainly on Fe_B, Fe_C, and O6, showing a strong hybridization between Fe_B3*d* and O2*p* (Figure 1.15b). To confirm the strong hybridization between Fe and O, DV-Xα molecular orbital calculations

were performed for each FeO_6 site. As shown in Figure 1.16, hybridization between Fe3*d* orbital and O2*p* orbital is observed for all of the t_{2g} molecular orbitals of FeO_6 clusters (Table 1.1), e.g., Fe_BO_6 possesses a large hybridization with 81 % of the charge distribution on $3d_{zx}$ of Fe_B and 19 % on $2p_x$ of O.

On the basis of the information presented above, the large magnetic anisotropy of ε-Fe_2O_3 is explained by the following. The classical valence state of the Fe ion in ε-Fe_2O_3 is +3, and the orbital angular momentum (***L***) is zero due to the half-filled high spin Fe^{3+} (d^5). However, both the periodic structure calculation and cluster calculation suggest a strong hybridization between Fe3*d* and O2*p* orbitals. This means that the electron is partially transferred from O2*p* to Fe3*d*, and the electron configuration of Fe becomes d^{5+q}, where q is the transferred charge. This partially transferred charge generates nonzero ***L*** and induces the magnetic anisotropy via spin-orbit interaction.[1.21,1.47,1.48] This nonzero ***L*** induces a large magnetic anisotropy,[1.43] which produces the huge H_c value.

1.4. Millimeter-wave absorption by zero-field ferromagnetic resonance

Electromagnetic (EM) waves called millimeter-waves with frequencies between 30 and 300 GHz have received much attention as EM waves for next-generation wireless communications such as Wireless Gigabit (WiGig), which sends heavy data including high-resolution images at an efficient speed. Additionally, car radars and advanced driver-assistance systems (ADAS) also employ millimeter-waves.[1.49–1.53] In the millimeter-wave era, millimeter-wave absorbers need to be developed to avoid EM wave interference problems. For this purpose, magnetic ferrites are important because they can absorb EM waves.[1.54–1.57] However, common magnetic ferrites such as spinel ferrite exhibit EM wave absorption at a few GHz, and even barium ferrite only has a resonance frequency of

several tens of GHz. On the other hand, ε-Fe_2O_3 shows high-frequency millimeter-wave absorption at 182 GHz due to zero-field ferromagnetic resonance (so-called natural resonance), which is quantum mechanically explained as Kittel-mode magnon.[1.32] This high resonance frequency of ε-Fe_2O_3 originates from the material's strong magnetic anisotropy.

1.5. Metal-substituted ε-Fe_2O_3

The Fe^{3+} ions of ε-Fe_2O_3 can be replaced by other transition metal ions, and several series of metal-substituted ε-Fe_2O_3 have been reported. In Ga-substituted ε-Fe_2O_3, the nonmagnetic Ga^{3+} ions selectively replace the Fe^{3+} ions at the tetrahedral Fe_D site. By Ga-substitution, the magnetization value increases, and the coercive field value decreases, causing a decrease of the resonance frequency.[1.31] A similar tendency is observed for the case of Al-substituted ε-Fe_2O_3. [1.32] In contrast, In^{3+} ions prefer to occupy the distorted octahedral Fe_B site. In-substitution reduces the coercive field value, but an additional characteristic of this series is that it exhibits a temperature-induced ferri-antiferromagnetic phase transition.[1.58] Another example is Rh-substituted ε-Fe_2O_3, in which the Rh^{3+} ions selectively occupy the octahedral Fe_C site. Different from other metal-substitution, Rh-substitution decreases the magnetization and increases the coercive field. Consequently, the resonance frequency of millimeter-wave absorption increases.[1.59,1.60] The site selectivity originates from the ionic radius of the substituting metal ion. By selecting the type of the transition metal ion and tuning the substitution ratio, the magnetic properties and millimeter-wave absorption properties of ε-Fe_2O_3 could be controlled.

1.6. Overview of this thesis

In the present doctoral thesis, the following aspects are described for the purpose of understanding the fundamental properties of ε-Fe_2O_3 and its analogue materials: introduction of the electronic structure of ε-Fe_2O_3 (Chapter 1), optical properties and phonon modes of ε-Fe_2O_3 (Chapter 2), magnetic properties, optical properties, and phonon modes of Ga-substituted ε-Fe_2O_3 (Chapter 3), and millimeter-wave absorption and rotation properties of metal-substituted ε-Fe_2O_3 (Chapters 4 and 5). Figure 1.18 shows a diagram of the wavelength and frequency of electromagnetic waves and the fundamental properties that correlate with each wavelength/frequency range.

References

[1.1] I. Dzyaloshinsky, *J. Phys. Chem. Solids* 4, 241 (1958).

[1.2] T. Moriya, *Phys. Rev. Lett.* 4, 228 (1960).

[1.3] R. M. Cornell, U. Schwertmann, *The Iron Oxide: Structure, Properties, Reactions, Occurrence and Uses*, Wiely-VCH, Weinheim (1999).

[1.4] R. Zbořil, M. Mashlan, D. Petridis, *Chem. Mater.* 14, 969 (2002).

[1.5] S. Sakurai, A. Namai, K. Hashimoto, S. Ohkoshi, *J. Am. Chem. Soc*. 131, 18299 (2009).

[1.6] J. Tuček, R. Zbořil, A. Namai, S. Ohkoshi, *Chem. Mater*. 22, 6483 (2010).

[1.7] W. D. Chang, T. S. Chin, *IEEE Trans. Magn*. 32, 3620 (1996).

[1.8] E. T. Lacheisserie, D. Gignoux, M. Schlenker, *Magnetism: II-Materials & Applications*, Kluwer, Norwell (2002).

[1.9] H. Forestier, G. Guiot-Guillain, *Compt. Rend.* 199, 720 (1934).

[1.10] M. Bonnevie-Svendsen, *Naturwissenschaften*, 45, 542 (1958).

[1.11] L. Ben-dor, E. Fischbein, *Acta Cryst. B* 32, 667 (1976).

[1.12] E. Tronc, C. Chanéac, J. P. Jolivet, *J. Solid State Chem.* 139, 93 (1998).

[1.13] J. Jin, S. Ohkoshi, K. Hashimoto, *Adv. Mater.* 16, 48 (2004).

[1.14] S. Ohkoshi, S. Sakurai, J. Jin, K. Hashimoto, *J. Appl. Phys.* 97, 10K312 (2005).

[1.15] S. Sakurai, J. Jin, K. Hashimoto, S. Ohkoshi, *J. Phys. Soc. Jpn.* 74, 1946 (2005).

[1.16] M. Gich, A. Roig, C. Frontera, E. Molins, J. Sort, M. Popovici, G. Chouteau, D. M. Y. Marero, J. Nogues, *J. Appl. Phys.* 98, 044307 (2005).

[1.17] E. Tronc, C. Chaneac, J. P. Jolivet, J. M. Greneche, *J. Appl. Phys*. 98, 053901 (2005).

[1.18] M. Kurmoo, J. -L. Rehspringer, A. Hutlova, C. D'Orléans, S. Vilminot, C. Estournès, *Chem. Mater.* 17, 1106 (2005).

[1.19] J. Tuček, S. Ohkoshi, R. Zbořil, *Appl. Phys. Lett.* 99, 253108 (2011).

[1.20] M. Gich, C. Frontera, A. Roig, E. Taboada, E. Molins, *Chem. Mater.* 18, 3889 (2006).

[1.21] Y. -C. Tseng, N. M. Souza-Neto, D. Haskel, M. Gich, C. Frontera, A. Roig, M. Veenendaal, J. Nogués, *Phys. Rev. B* 79, 094404 (2009).

[1.22] M. Popovici, M. Gich, D. Niznansky, A. Roig, C. Savii, L. Casas, E. Molins, K. Zaveta, C. Enache, J. Sort, *Chem. Mater*. 16, 55428 (2004).

[1.23] K. Kelm, W. Mader, *Z. Anorg. Allg. Chem.* 631, 2383 (2005).

[1.24] J. Jin, K. Hashimoto, S. Ohkoshi, *J. Mater. Chem.* 15, 1067 (2005).

[1.25] J. L. Morber, Y. Ding, M. S. Haluska, Y. Li, J. P. Liu, Z. L. Wang, R. L. Snyder, *J. Phys. Chem. B* 110, 21672 (2006).

[1.26] M. Gich, C. Frontera, A. Roig, J. Fontcuberta, E. Molins, N. Bellido, C. Simon, C. Fleta, *Nanotechnology* 17, 687 (2006).

[1.27] T. Nakamura, Y. Yamada, K. Yano, *J. Mater. Chem.* 16, 2417 (2006).

[1.28] M. Gich, A. Roig, E. Taboada, E. Molins, C. Bonafos, E. Snoeck, *Faraday Discuss.* 136, 345 (2007).

[1.29] Y. Ding, J. R. Morber, R. L. Snyder, Z. L. Wang, *Adv. Funct. Mater.* 17, 1172 (2007).

[1.30] Y. Kusano, T. Fujii, J. Takada, M. Fukuhara, A. Doi, Y. Ikeda, M. Takano, *Chem. Mater*. 20, 151 (2008).

[1.31] S. Ohkoshi, S. Kuroki, S. Sakurai, K. Matsumoto, K. Sato, S. Sasaki, *Angew. Chem. Int. Ed.* 46, 8392 (2007).

[1.32] A. Namai, S. Sakurai, M. Nakajima, T. Suemoto, K. Matsumoto, M. Goto, S. Sasaki, S. Ohkoshi, *J. Am. Chem. Soc.* 131, 1170 (2009).

[1.33] M. N. Afsar, Z. Li, K. A. Korolev, A. Namai, S. Ohkoshi, *J. Appl. Phys.* 109, 07E316 (2011).

[1.34] Z. Li, K. A. Korolev, M. N. Afsar, A. Namai, S. Ohkoshi, *IEEE Trans. Magn.* 47, 333 (2011).

[1.35] S. Ohkoshi, A. Namai, K. Imoto, M. Yoshikiyo, W. Tarora, K. Nakagawa, M. Komine, Y. Miyamoto, T. Nasu, S. Oka, H. Tokoro, *Sci. Rep.* 5, 14414 (2015).

[1.36] H. Tokoro, W. Tarora, A. Namai, M. Yoshikiyo, S. Ohkoshi, *Chem. Mater.* 30, 2888 (2018).

[1.37] J. M. McHale, A. Auroux, A. J. Perrotta, A. Navrotsky, *Science* 277, 788 (1997).

[1.38] H. L.Wen, Y. Y. Chen, F. S.Yen, C. H. Huang, *Nanostruct. Mater.* 11, 89 (1999).

[1.39] H. Zhang, J. F. Banfield, *J. Mater. Chem.* 8, 2073 (1998).

[1.40] J. L. García-Muñoz, A. Romaguera, F. Fauth, J. Nogués, M. Gich, *Chem. Mater.* 29, 9705 (2017).

[1.41] B. D. Cullity, *Introduction to Magnetic Materials,* Addison-Wesley Publ. Co., Reding (1972).

[1.42] D. Fiorani, G. Sberveglieri, *Fundamental Properties of Nanostructured Materials*, World Scientific Publishing, Singapore (1993).

[1.43] S. Chikazumi, *Physics of Ferromagnetism*, Oxford University Press, New York (1997).

[1.44] M. Yoshikiyo, K. Yamada, A. Namai, S. Ohkoshi, *J. Phys. Chem. C* 116, 8688 (2012).

[1.45] P. A. Cox, *The Electronic Structure of Solids*; Oxford University Press: U.S.A., (1987).

[1.46] S. Ohkoshi, A. Namai, S. Sakurai, *J. Phys. Chem. C* 113, 11235 (2009).

[1.47] J. -Y. Kim, T. Y. Koo, J. -H. Park, *Phys. Rev. Lett.* 96, 047205 (2006).

[1.48] J. -Y. Kim, T. Y. Koo, B. -G. Park, J. -H. Park, *J. Magn. Magn. Mater.* 310, 1180 (2007).

[1.49] A. Vilcot, B. Cabon, J. Chazelas, *Microwave Photonics* Kluwer, Boston (1996).

[1.50] M. J. W. Rodwell, *High Speed Integrated Circuit Technology, towards 100 GHz Logic*, World Scientific, Singapore (2001).

[1.51] C. H. Doan, S. Emami, A. M. Niknejad, R. W. Brodersen, *IEEE J. Solid-State Circuits* 40, 144 (*2005*).

[1.52] S. Yong, P. Xia, A. V. Garcia, *60 GHz Technology for Gbps WLAN and WPAN: From Theory to Practice*, Wiely, Oxford (2011).

[1.53] K. -C. Huang, Z. Wang, *Millimeter Wave Communication Systems*, Wiley-IEEE Press, Piscataway (2011).

[1.54] J. L. Snoek, *Physica* 14, 207 (1948).

[1.55] J. Helszajn, *Principles of microwave ferrite engineering*, Wiley-Interscience, London (1969).

[1.56] K. J. Vinoy, R. M. Jha, *Radar Absorbing Materials*, Kluwer, Boston (1996).

[1.57] Y. Naito, K. Suetake, *IEEE Trans. Microwave Theory Tech.* 19, 65 (1971).

[1.58] S. Sakurai, S. Kuroki, H. Tokoro, K. Hashimoto, S. Ohkoshi, *Adv. Funct. Mater.* 17, 2278 (2007).

[1.59] A. Namai, M. Yoshikiyo, K. Yamada, S. Sakurai, T. Goto, T. Yoshida, T. Miyazaki, M. Nakajima, T. Suemoto, H. Tokoro, S. Ohkoshi, *Nat. Commun.* 3, 1035 (2012).

[1.60] A. Namai, M. Yoshikiyo, S. Umeda, T. Yoshida, T. Miyazaki, M. Nakajima, K. Yamaguchi, T. Suemoto, S. Ohkoshi, *J. Mater. Chem. C* 1, 5200 (2013).

Figures and Tables

Table 1.1 Charge distribution of the t_{2g} molecular orbitals of the FeO_6 sites in ε-Fe_2O_3. [Adapted with permission from J. Phys. Chem. C, 116, 8688 (2012). Copyright 2012 American Chemical Society.]

		Fe_AO_6	Fe_BO_6	Fe_CO_6
d_{xy}	Fe (%)	83	86	88
	O (%)	17	14	12
d_{yz}	Fe (%)	87	83	91
	O (%)	13	17	9
d_{zx}	Fe (%)	88	81	88
	O (%)	12	19	12

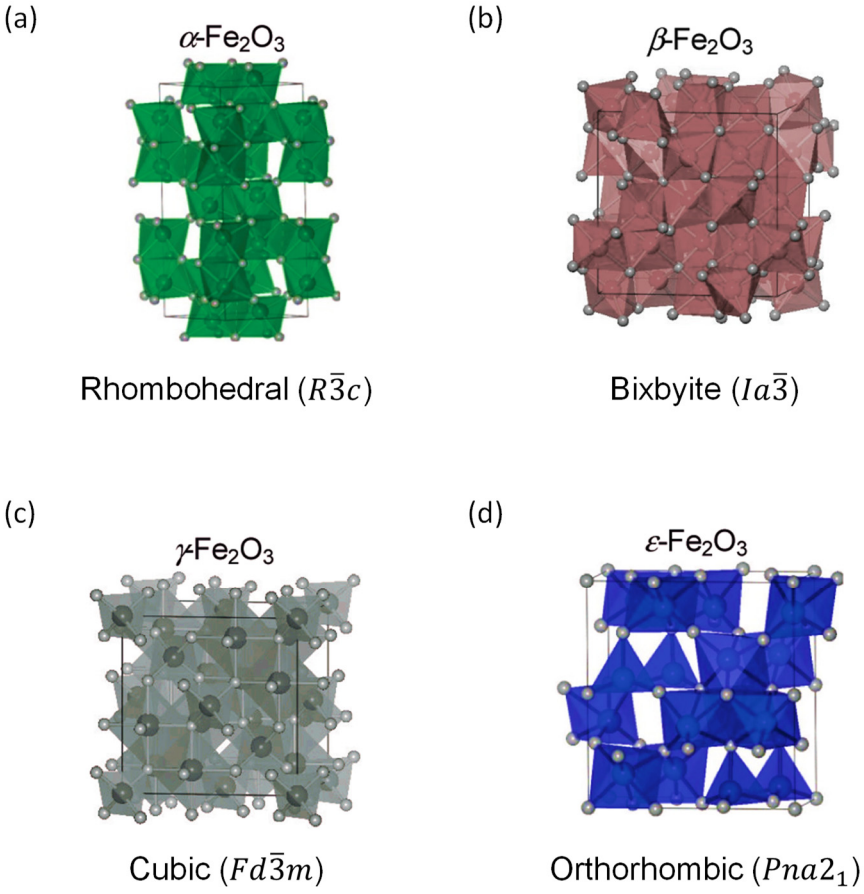

Figure 1.1 Crystal structures of (a) α-Fe_2O_3, (b) β-Fe_2O_3, (c) γ-Fe_2O_3, and (d) ε-Fe_2O_3. [Adapted with permission from J. Am. Chem. Soc., 131, 18299 (2009). Copyright 2009 American Chemical Society.]

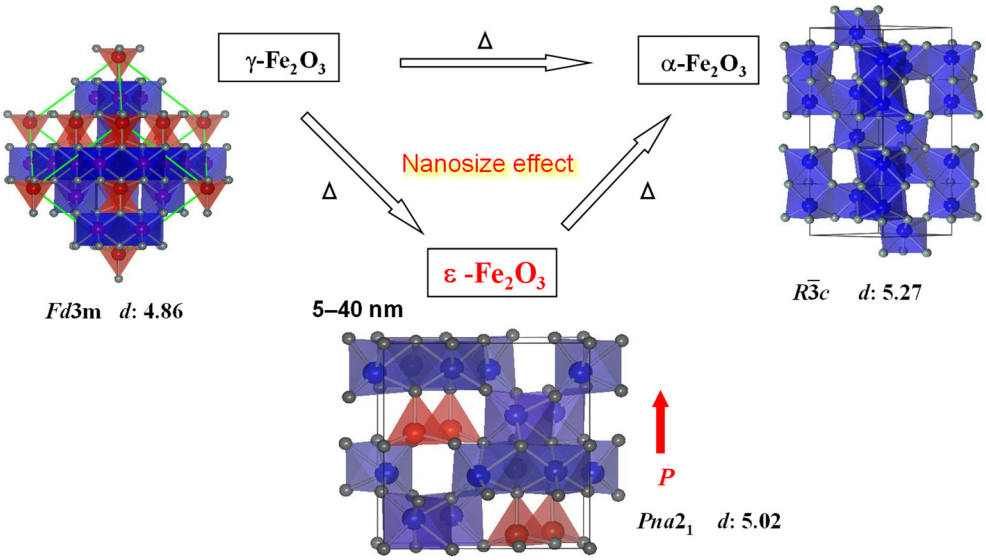

Figure 1.2 Phase transformation of iron oxide Fe_2O_3.

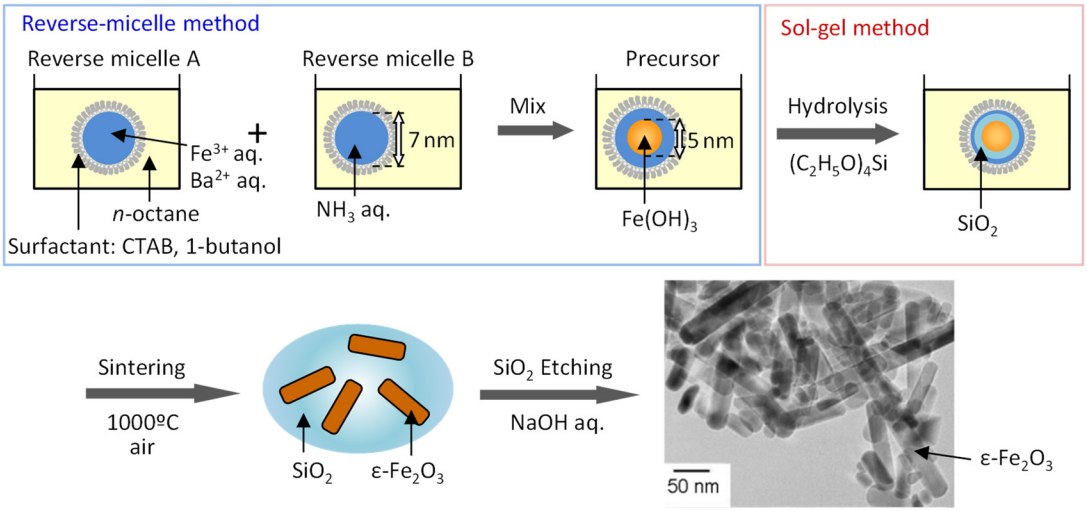

Figure 1.3 Synthetic procedure of ε-Fe_2O_3 nanomagnets using a combined method of reverse-micelle and sol-gel techniques.

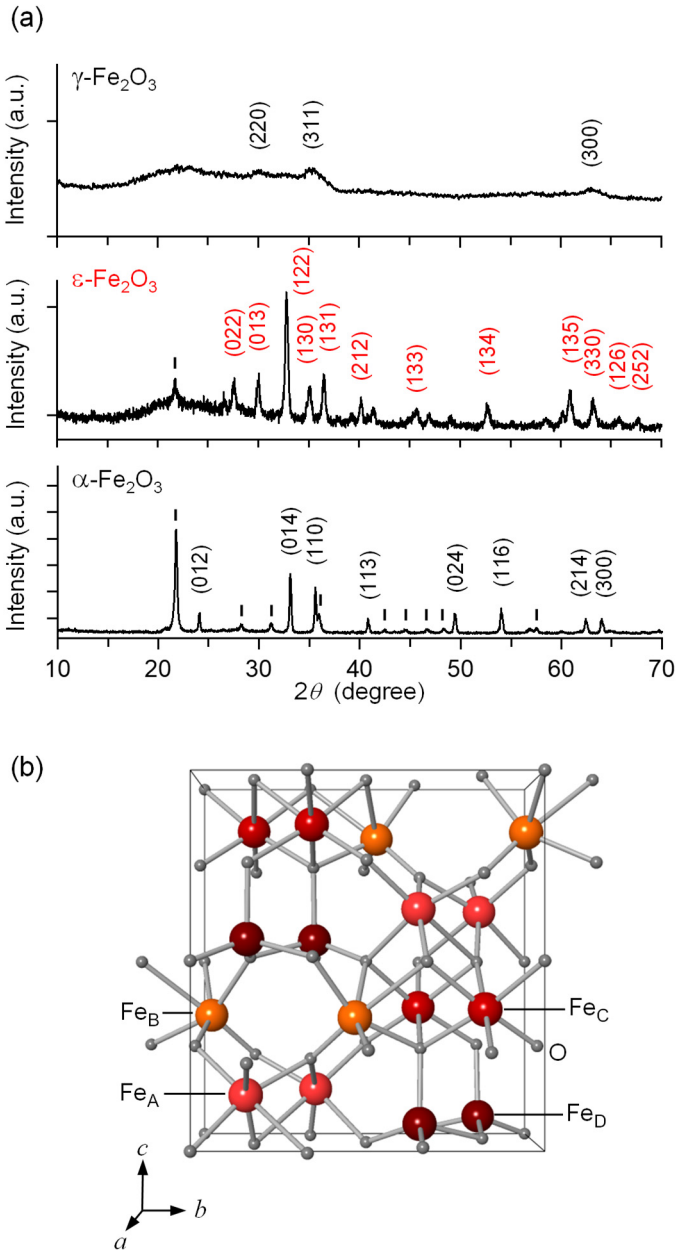

Figure 1.4 (a) XRD patterns of samples sintered at 900 °C (upper), 1000 °C (middle), and 1100 °C (lower). Diffraction peaks are indicated by Miller indices corresponding to the space groups of γ-Fe_2O_3, ε-Fe_2O_3, and α-Fe_2O_3 phases. Black bars represent the peaks of cristobalite (SiO_2). (b) Crystal structure of orthorhombic unit cell of ε-Fe_2O_3. [Adapted with permission from Bull. Chem. Soc. Jpn., 86, 897 (2013). © 2013 The Chemical Society of Japan.]

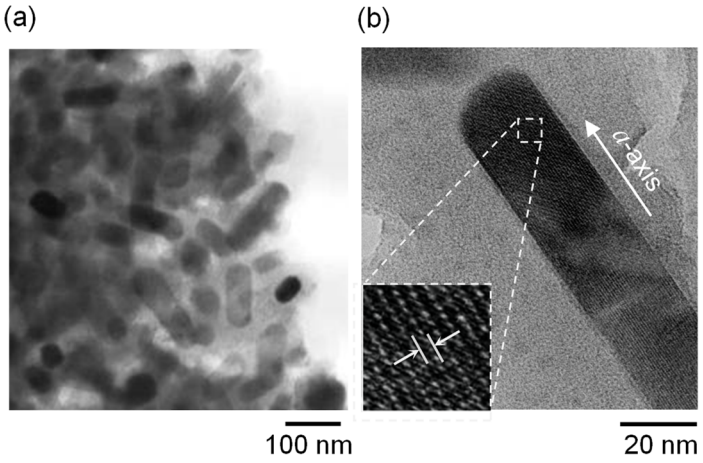

Figure 1.5 TEM images of ε-Fe_2O_3. (a) TEM image of ε-Fe_2O_3 sample obtained by 1000 ºC sintering. (b) Enlarged TEM image of a single particle sample showing ε-Fe_2O_3 in silica matrix. Inset is a high resolution TEM image of the particle with its lattice planes. [Adapted with permission from Bull. Chem. Soc. Jpn., 86, 897 (2013). © 2013 The Chemical Society of Japan.]

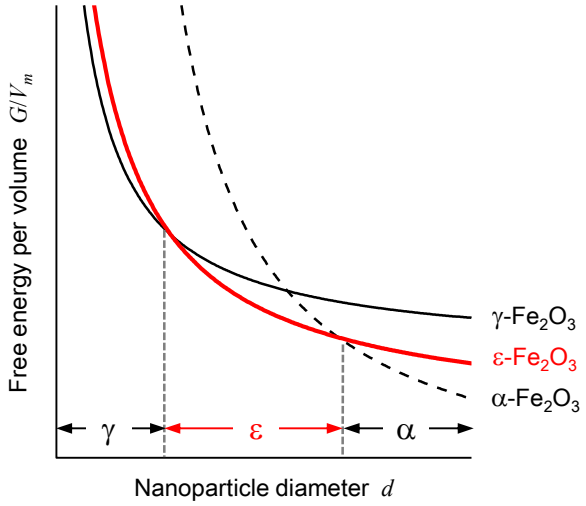

Figure 1.6 Calculated G/V_m versus d curves for three iron oxide phases: γ-Fe_2O_3 (solid black line), ε-Fe_2O_3 (red line), α-Fe_2O_3 (dotted black line). These curves are based on Eq. (1) under the condition of $\mu_\gamma > \mu_\varepsilon > \mu_\alpha$, $s_\gamma < s_\varepsilon < s_\alpha$, and $(s_\varepsilon - s_\gamma)/(m_\varepsilon - m_\gamma) > (s_\varepsilon - s_\alpha)/(\mu_\varepsilon - \mu_\alpha)$. [Adapted with permission from Bull. Chem. Soc. Jpn., 86, 897 (2013). © 2013 The Chemical Society of Japan.]

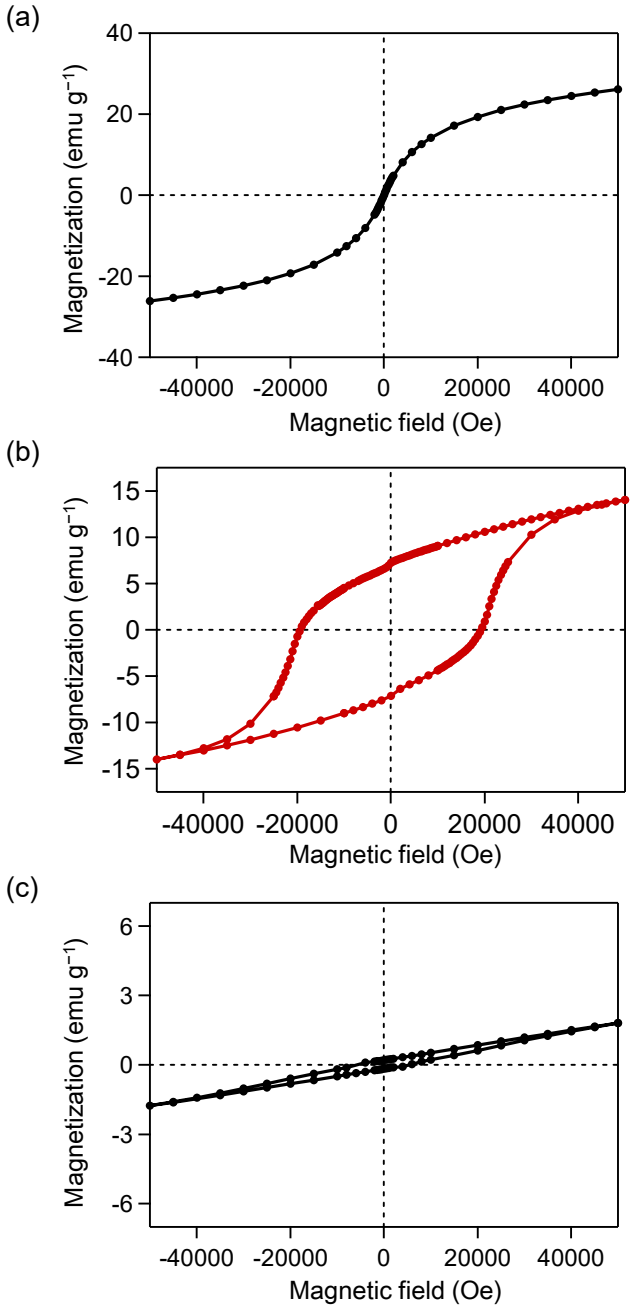

Figure 1.7 Magnetization versus field plots at room temperature for γ-Fe_2O_3, (b) ε-Fe_2O_3, and (c) α-Fe_2O_3. [Adapted with permission from Bull. Chem. Soc. Jpn., 86, 897 (2013). © 2013 The Chemical Society of Japan.]

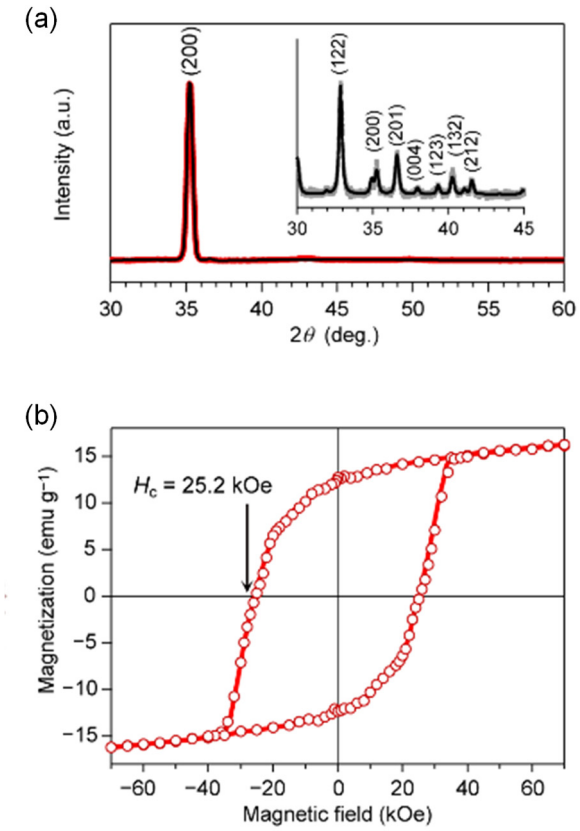

Figure 1.8 (a) XRD pattern of the film based on crystallographically oriented ε-Fe_2O_3 rods and XRD pattern of the nonoriented ε-Fe_2O_3 rods (inset). Red line, gray line, and black lines indicate the observed pattern of oriented ε-Fe_2O_3 rods, observed pattern of nonoriented ε-Fe_2O_3 rods, and calculated patterns, respectively. (b) Magnetization versus external field plot of the ε-Fe_2O_3-rod oriented film measured at room temperature along a single in-plane direction. [Adapted with permission from Sci. Rep., 6, 27212 (2016). Copyright 2016 Springer Nature.]

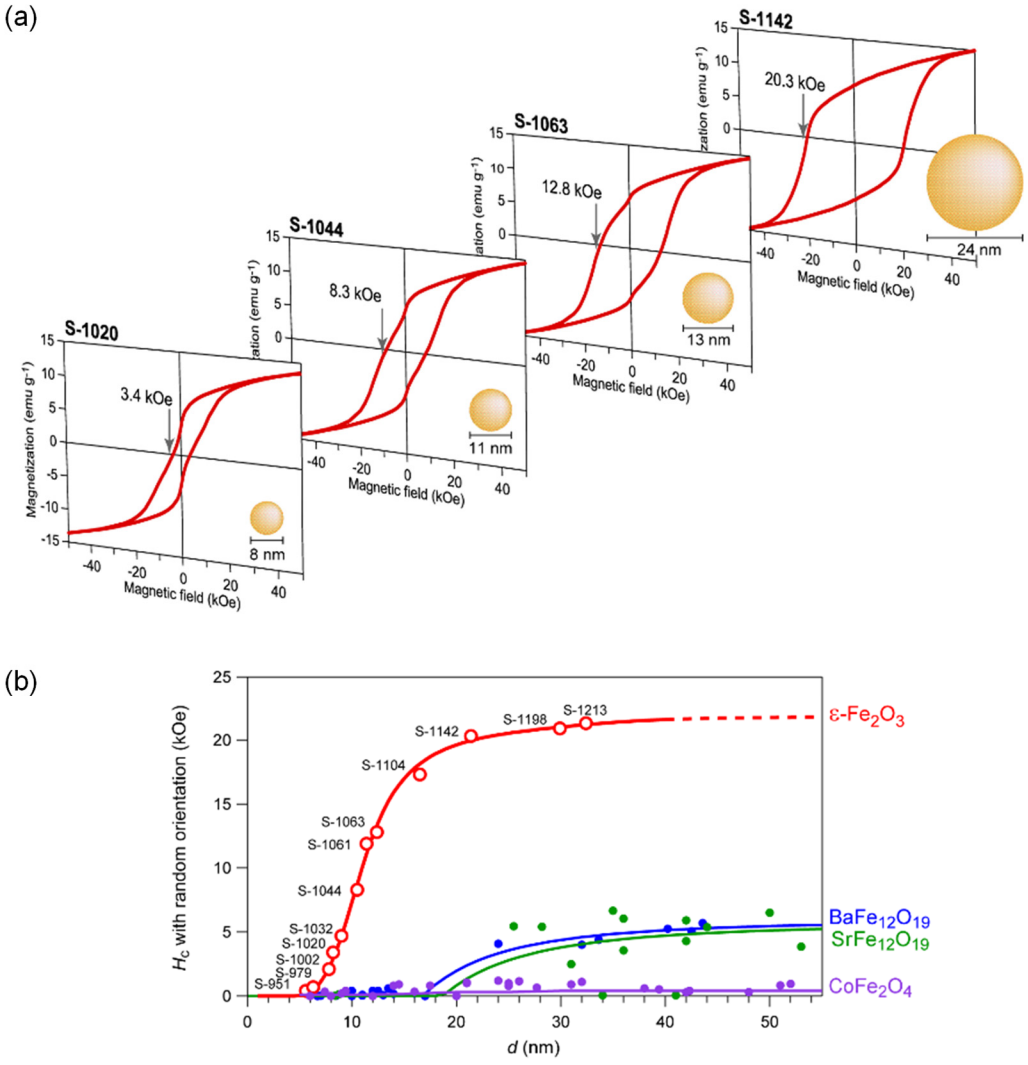

Figure 1.9 Particle size dependence of the magnetic properties. (a) Magnetic hysteresis loops of samples sintered at 1020 ºC (S-1020), 1044 ºC (S-1044), 1063 ºC (S-1063), and 1142 ºC (S-1142) measured at 300 K with an illustration of the average particle size. (b) H_c value at 300 K with random orientation versus d plot. The red line is a guide for the eye, which was drawn based on the d dependence equation of H_c, taking into account the random orientation and particle size distribution. The d_p (superparamagnetic limit) value was calculated to be 7.5 nm. The H_c versus d plots at room temperature of $BaFe_{12}O_{19}$ (blue), $SrFe_{12}O_{19}$ (green), and $CoFe_2O_4$ (purple) are also shown. [Adapted with permission from Sci. Rep., 5, 14414 (2015). Copyright 2015 Springer Nature.]

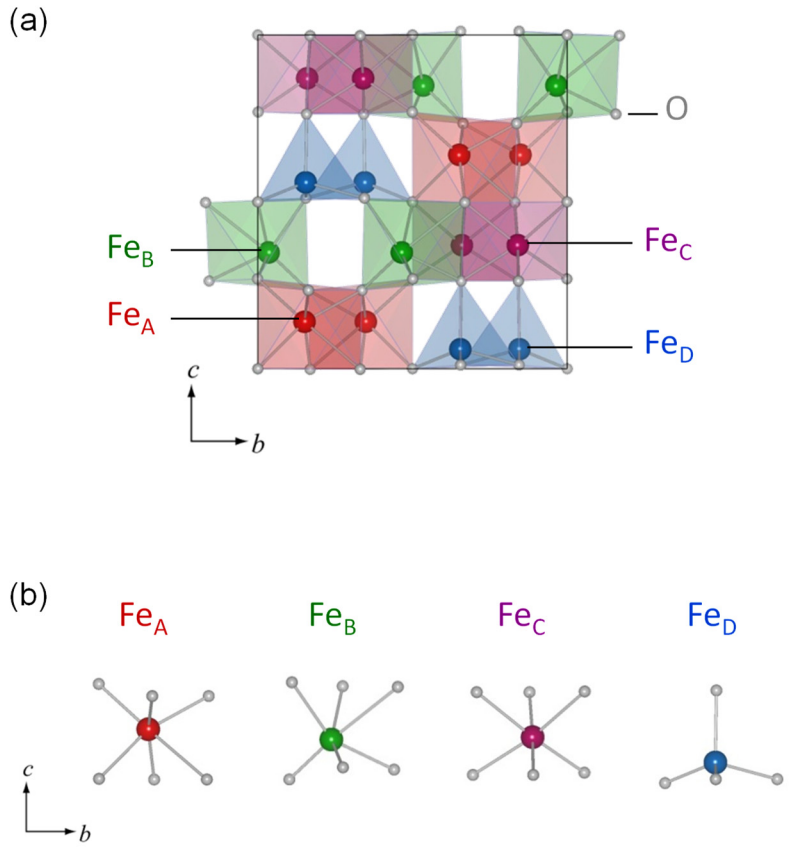

Figure 1.10 (a) Crystal structure of the ε-Fe_2O_3 unit cell used in the periodic structure calculation. Unit cell is composed of four asymmetrical units and is expressed as $Fe_{16}O_{24}$. (b) Coordination geometries of FeO_6 for Fe_A-Fe_C and FeO_4 for Fe_D used in the cluster calculation. [Adapted with permission from J. Phys. Chem. C, 116, 8688 (2012). Copyright 2012 American Chemical Society.]

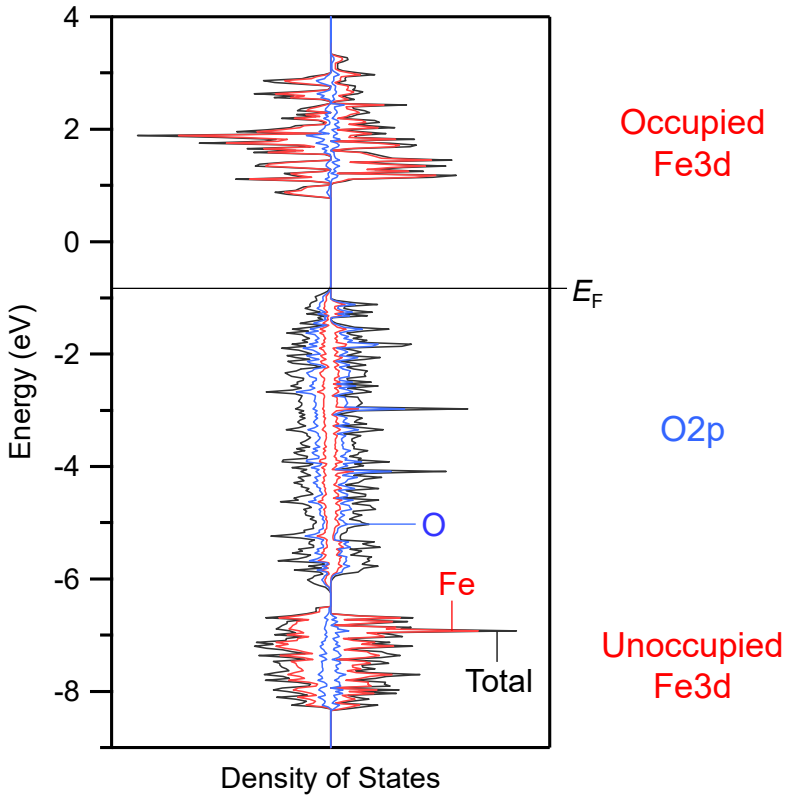

Figure 1.11 Density of states (DOS) of ε-Fe_2O_3. Total DOS (black lines), iron DOS (red lines), and oxygen DOS (blue lines) are shown. [Adapted with permission from J. Phys. Chem. C, 116, 8688 (2012). Copyright 2012 American Chemical Society.]

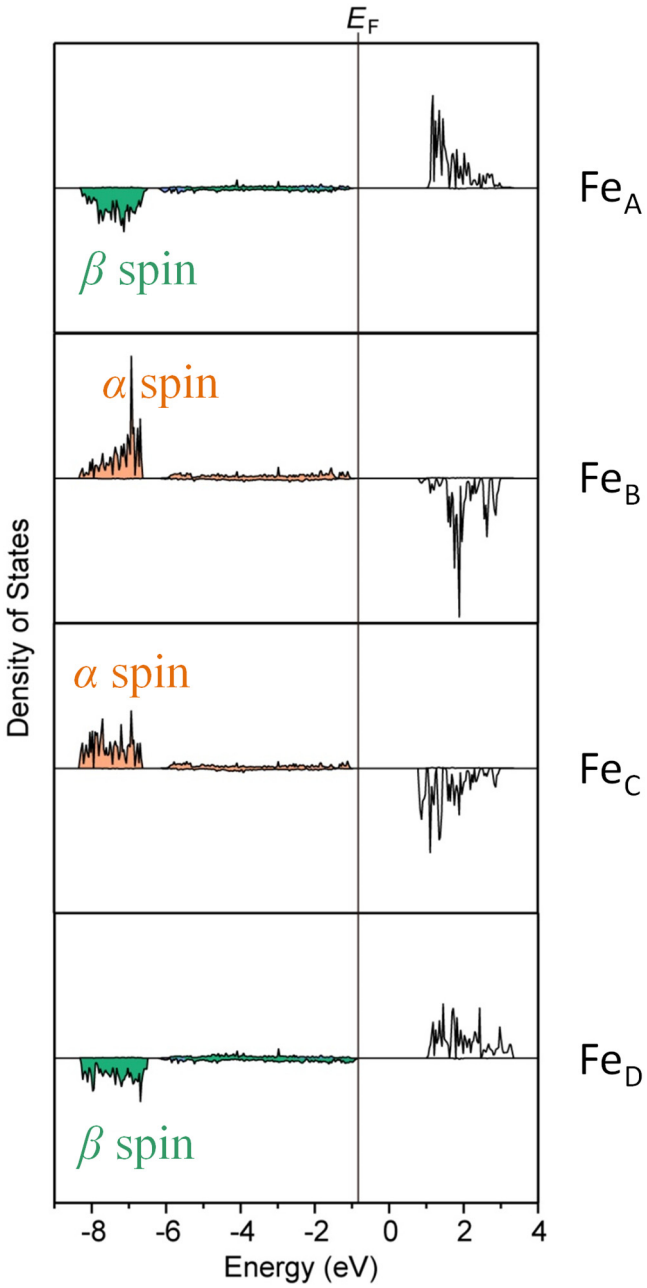

Figure 1.12 DOS of each Fe site for the spin configuration (β, α, α, β). The upper half of each DOS indicates α spin, and the lower half indicates β spin. Colored regions denote occupied regions. [Adapted with permission from J. Phys. Chem. C, 116, 8688 (2012). Copyright 2012 American Chemical Society.]

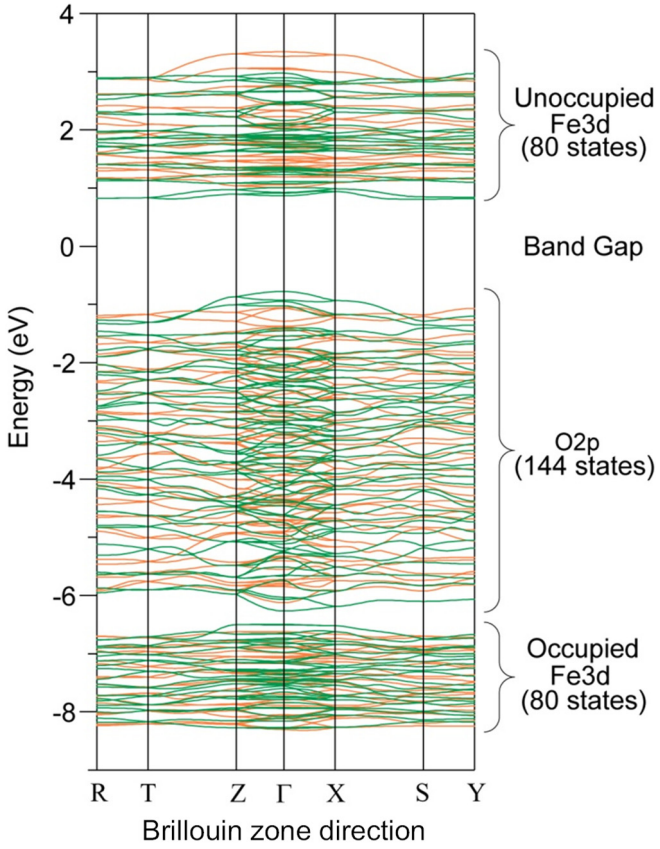

Figure 1.13 The band structure of ε-Fe_2O_3 in the energy range between –9 to +4 eV. There are three bands corresponding to occupied Fe3*d* band, O2*p* band, and unoccupied Fe3*d* band, which consist of 80, 144, and 80 states, respectively. Each unit cell has 16 Fe atoms and 24 O atoms, resulting in 80 Fe3*d* states and 144 O2*p* states. [Adapted with permission from J. Phys. Chem. C, 116, 8688 (2012). Copyright 2012 American Chemical Society.]

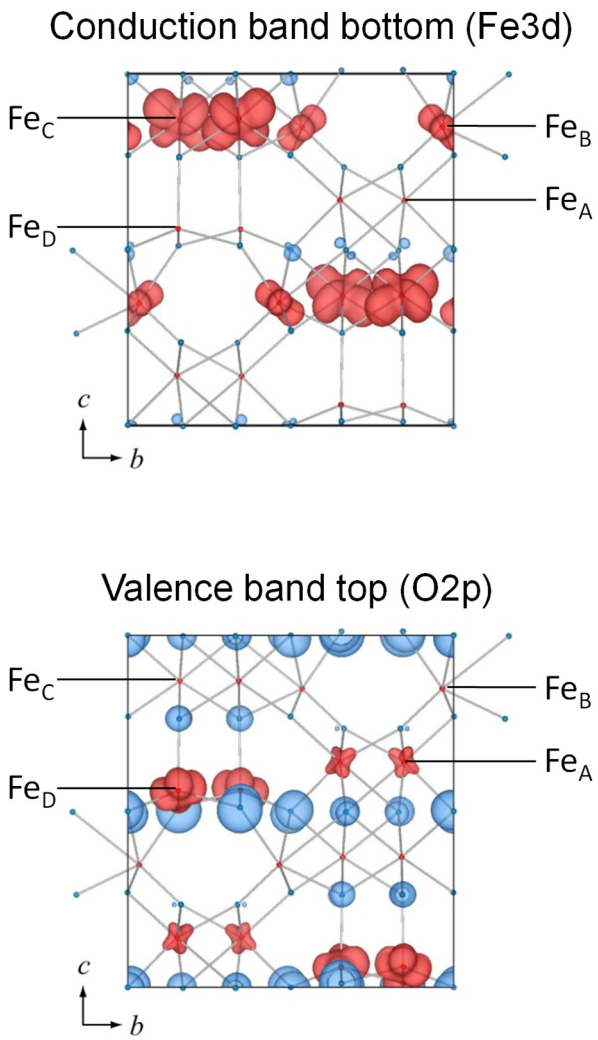

Figure 1.14 Charge density maps of the bottom of the conduction band and top of the valence band (isosurface, 0.0018 a_0^{-3}). Red and blue indicate the charge densities of Fe and O, respectively. [Adapted with permission from J. Phys. Chem. C, 116, 8688 (2012). Copyright 2012 American Chemical Society.]

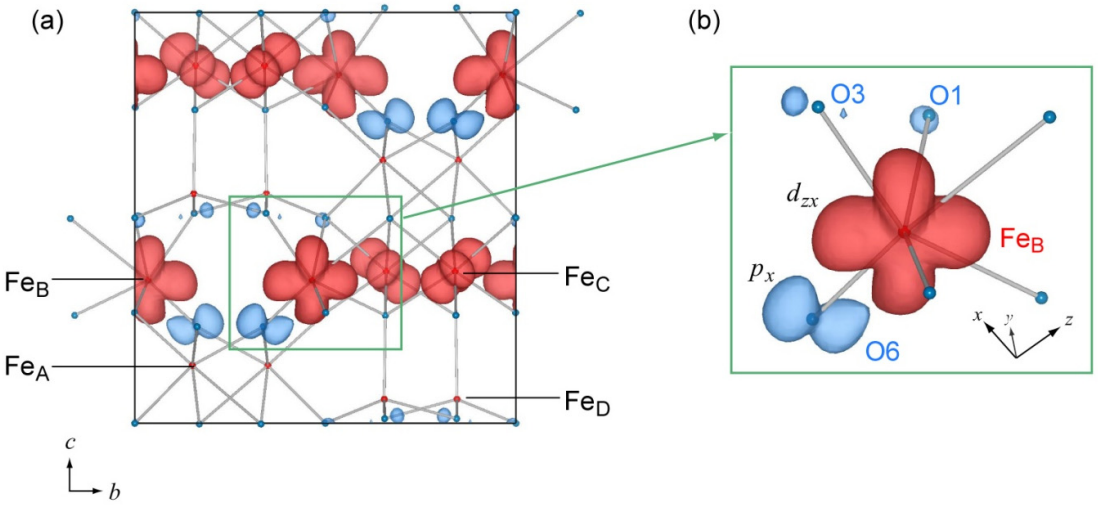

Figure 1.15 (a) Representative charge density map from the occupied Fe3*d* band (isosurface, 0.00154 a_0^{-3}). Red and blue indicate the charge densities of Fe and O, respectively. (b) Close up of the charge density around Fe_B in panel a, which indicates the Fe3d_{zx} and O2p_x orbitals. [Adapted with permission from J. Phys. Chem. C, 116, 8688 (2012). Copyright 2012 American Chemical Society.]

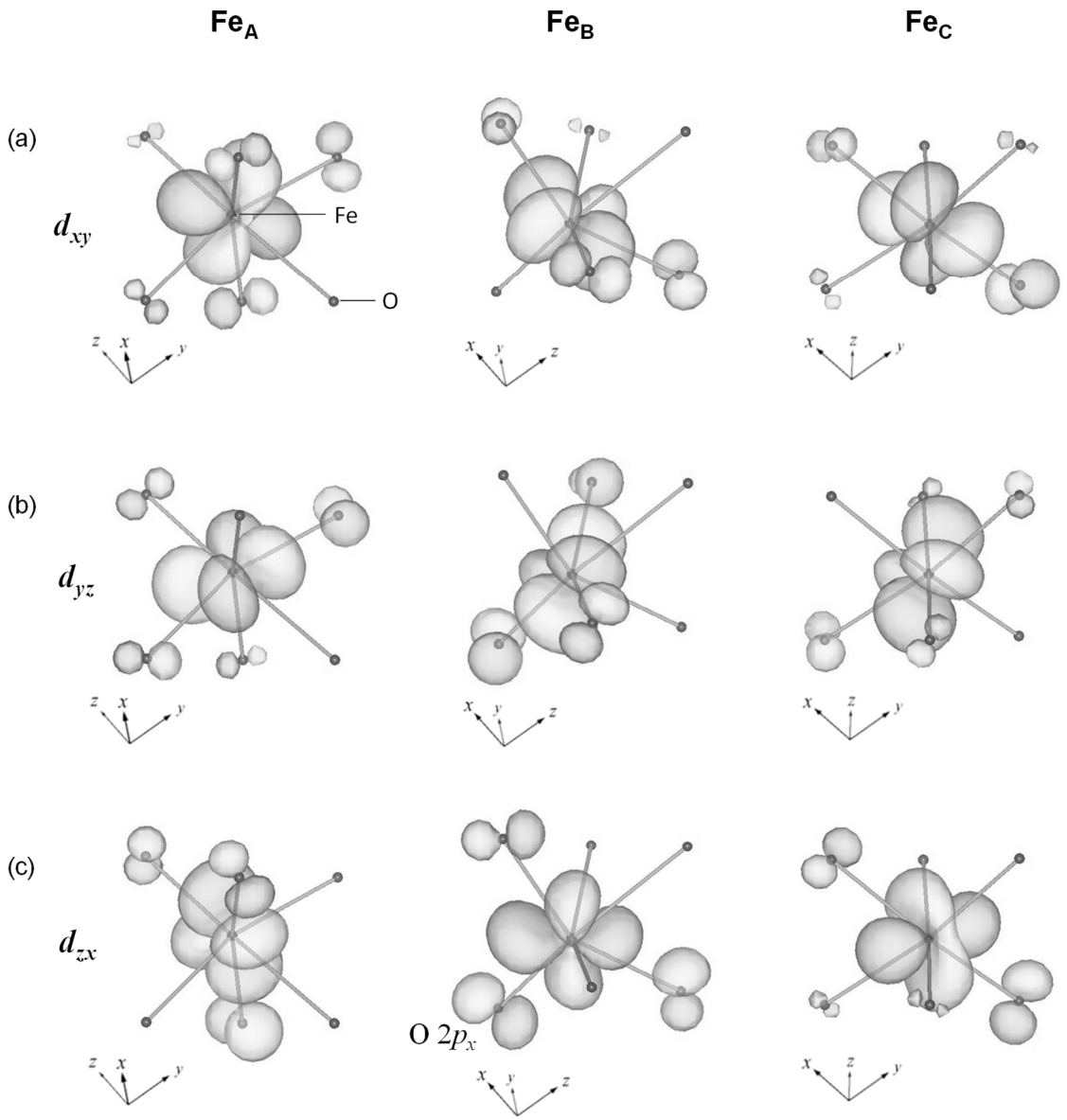

Figure 1.16 Molecular orbitals of the Fe3*d* t_{2g} orbitals, (a) d_{xy}, (b) d_{yz}, and (c) d_{zx}, for Fe_A, Fe_B, and Fe_C. The t_{2g} orbitals are focused since they are assumed to contribute to the magnetic properties. [Adapted with permission from J. Phys. Chem. C, 116, 8688 (2012). Copyright 2012 American Chemical Society.]

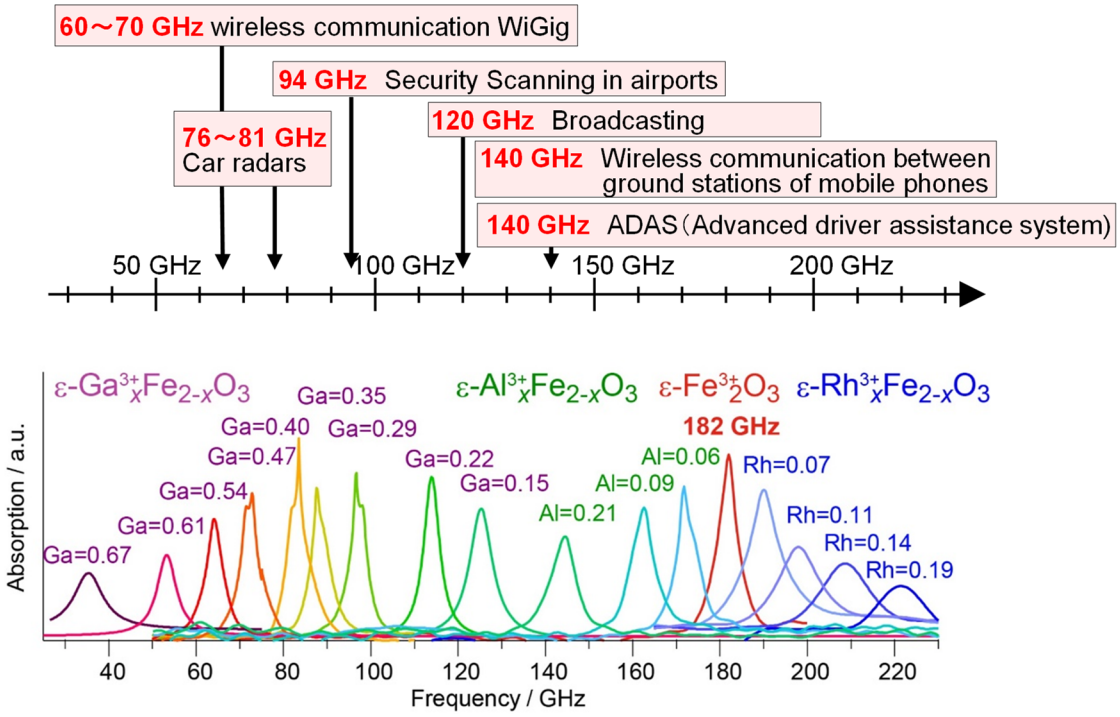

Figure 1.17 Various applications of millimeter-waves (upper) and millimeter-wave absorption spectra of ε-Fe_2O_3, ε-$Ga_xFe_{2-x}O_3$, ε-$Al_xFe_{2-x}O_3$, and ε-$Rh_xFe_{2-x}O_3$ (lower).

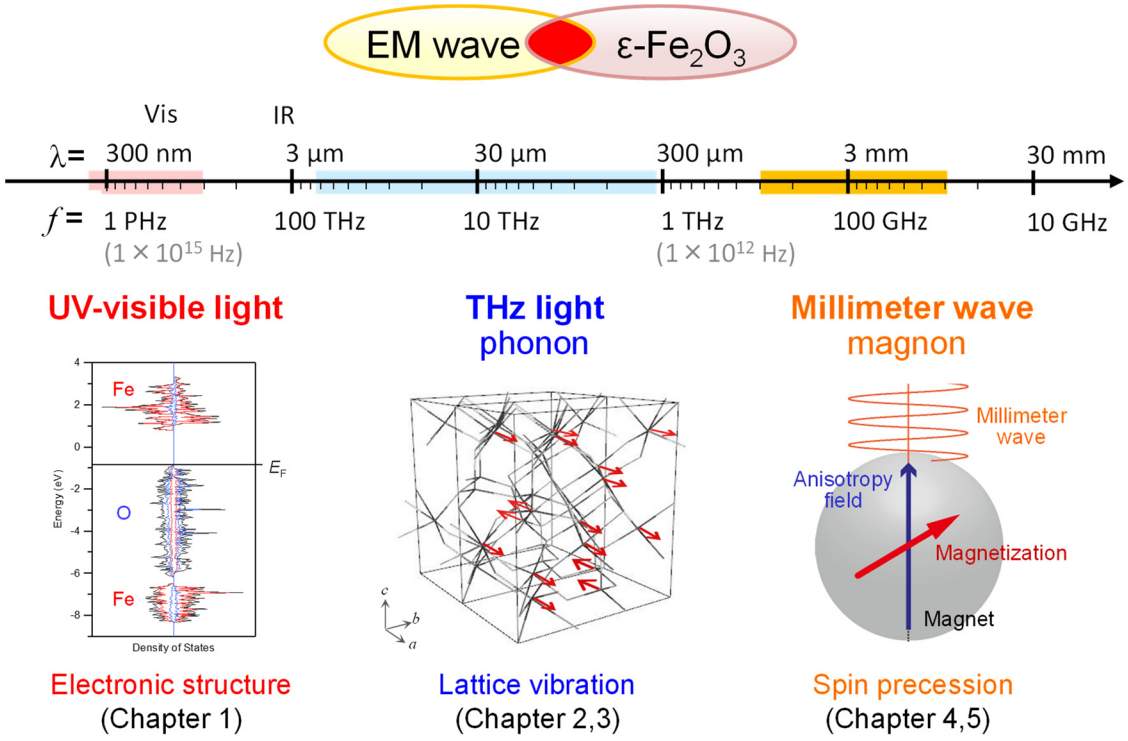

Figure 1.18 Diagram of the wavelength and frequency of electromagnetic (EM) waves indicating the physical properties that correlate with each wavelength/frequency range.

Chapter 2

Phonon mode calculation and lattice vibrations of ε-Fe_2O_3

Ferrite magnets have been known since the 7th century BC. Today, ferrite magnets are ubiquitous due to the abundance of iron. They are found in many forms such as Fe_2O_3, Fe_3O_4, and $BaFe_{12}O_{19}$. Applications range from everyday uses like headphones to diverse industrial products such as motors and generators.[2.1–2.9]

Iron oxide (Fe_2O_3) has four known phases: α-, β-, γ-, and ε-, of which α- and γ-Fe_2O_3 are naturally occurring and β- and ε-Fe_2O_3 are not. The phase affects the properties of iron oxide. For instance, γ-Fe_2O_3 is a ferrimagnet with a spinel structure,[2,10–2.12] while α-Fe_2O_3 is a weak ferromagnet with a corundum structure.[2.13–2.21] β-Fe_2O_3 is antiferromagnetic with a bixbyite structure.[2.22–2.24] ε-Fe_2O_3 is the least studied form since its pure phase was not synthesized until 2004. ε-Fe_2O_3 has with an orthorhombic crystal structure,[2.23,2.25,2.26] and was found to exhibit a large coercive field.[2.27] Researchers have been actively investigating the properties of ε-Fe_2O_3.[2.28–2.34]

This chapter investigates rod shaped ε-Fe_2O_3 with an emphasis on the synthesis, magnetic properties, and especially lattice vibrations by first-principles phonon mode calculations and far-infrared (Far-IR) spectroscopy measurement.

2.1. Experimental and computational details

Rod shaped ε-Fe_2O_3 were synthesized using reverse-micelle and sol-gel techniques. Two types of reverse-micelle solutions (I and II) were prepared using hexadecyltrimethylammonium bromide (38.8 mmol), *n*-butanol (157 mmol), octane (450

mmol), and water (1.3 mol). Reverse-micelle I, which consisted of iron(III) nitrate (2.9 mmol) and barium(II) nitrate (0.29 or 0.58 mmol) dissolved in the aqueous phase, and reverse-micelle-II, which consisted of ammonia (133 mmol) dissolved in the aqueous phase, were mixed and stirred. Next, tetraethyl orthosilicate (31 mmol) was injected, forming a precipitate. A centrifugal precipitator was used to extract the precipitate. After washing with chloroform and methanol, it was sintered at 980 or 1025 ºC for 4 h in ambient air. An aqueous sodium hydroxide solution at 70 ºC etched the calcined powder. Finally, the silica matrix covering the iron oxide rods was removed by washing with an aqueous hydrochloric acid solution to give ε-Fe_2O_3 rods.

This study employed a number of devices to collect spectroscopic data. A JEOL JEM 2000EX was used to aquire the TEM images. A Rigaku Ultima IV with Cu Kα irradiation (λ = 1.5418 Å) and Rigaku SmartLab were used to acquire the XRD patterns. A Quantum Design MPMS SQUID magnetometer was used for magnetic measurements. A JASCO 6100 spectrometer was used to acquire the far-IR spectra.

Theoretical calculations were carried out to elucidate the lattice vibrations of ε-Fe_2O_3. The Phonon code[2.35] in a Material Design MedeA package was used to determine the phonon modes. The atomic positions of ε-Fe_2O_3 were optimized with a 400-eV energy cutoff and 3 × 3 × 3 *k*-mesh until a 10^{-5} eV pm^{-1} force tolerance was satisfied. The phonon modes of ε-Fe_2O_3 were calculated using these optimized structures and the direct method implemented in Phonon code with 2-pm displacements.

2.2. Results and discussion

The ε-Fe_2O_3 rods measure several hundred nanometers in the longitudinal direction (SEM images) with an orthorhombic *Pna*2_1 (XRD pattern) and lattice constants of *a* =

5.08923(16) Å, b = 8.7858(3) Å, and c = 9.4766(2) Å (Table 2.1). The single crystal has a noncentrosymmetric structure with four different Fe sites. Figure 2.1 shows that Fe_AO_6 and Fe_BO_6 are distorted octahedral sites, Fe_CO_6 is a regular octahedral site, and Fe_DO_4 is a tetrahedral site. The electric polarization is along the crystallographic c-axis. Analysis of the TEM image indicates that the longitudinal direction of the nanorod is the crystallographic a-axis (Fig. 2.2).

Phonon mode calculations were performed to understand the lattice vibration in ε-Fe_2O_3. Table 2.2 lists all of the phonon modes accompanied by their symmetries and IR / Raman activities. Figure 2.3 shows the phonon dispersion and phonon density of states. ε-Fe_2O_3 has 117 optical phonon modes ranging from 2.51 to 20.53 THz. Figure 2-4b shows the calculated phonon mode spectrum between 5.4 and 12 THz.

The lattice vibrations of rod-shaped ε-Fe_2O_3 were measured by far-IR spectroscopy. Absorption peaks were observed at 2.62 THz (87.3 cm^{-1}), 3.31 THz (110.4 cm^{-1}), 3.65 THz (121.8 cm^{-1}), 3.87 THz (129.1 cm^{-1}), 4.45 THz (148.4 cm^{-1}), 4.73 THz (157.9 cm^{-1}), and 5.21 THz (173.8 cm^{-1}) in the frequency range of 2.2 THz (λ = 136 μm, 73 cm^{-1}) – 5.4 THz (λ = 56 μm, 180 cm^{-1}) (Fig. 2.4a, upper). Meanwhile, IR spectrum was simulated from the calculated phonon modes of ε-Fe_2O_3, which showed good agreement with the observed far-IR spectrum (Fig. 2.4a, lower). Therefore, the observed lattice vibration at 2.62 THz is assigned to the calculated optical phonon mode of 2.51 THz, which is assigned to the Fe atom vibration along the crystallographic a-axis with A_1 symmetry (Fig. 2.4b). Figure 2.g shows the far-IR spectrum in the 5.4–12-THz range.

2.3. Chapter summary

This chapter reports a rod-shaped single crystal bar magnet of ε-Fe_2O_3. The atomic

movements of ε-Fe_2O_3 was calculated by phonon mode calculations. The lowest frequency phonon mode in the ε-Fe_2O_3 bar magnet vibrates along the crystallographic *a*-axis, which is the growth direction of the bar magnet. The simulated IR spectrum from the phonon mode calculations showed good correspondence with the experimentally obtained far-IR spectrum.

References

[2.1] K. J. Gallagher, W. Feitknect, U. Mannweiler, *Nature* 217, 1118 (1968).

[2.2] G. A. Challis, *Nature* 255, 471 (1975).

[2.3] C. T. Yavuz, J. T. Mayo, W. W. Yu, A. Prakash, J. C. Falkner, S. Yean, L. Cong, H. J. Shipley, A. Kan, M. Tomson, D. Natelson, V. L. Colvin, *Science* 314, 964 (2006).

[2.4] T. P. Almeida, T. Kasama, A. R. Muxworthy, W. Williams, L. Nagy, T. W. Hansen, P. D. Brown, R. E. Dunin-Borkowski, *Nat. Commun.* 5, 5154 (2014).

[2.5] B. D. Cullity, C. D. Graham, *Introduction to Magnetic Materials, 2nd ed.*, Wiley-IEEE Press, New Jersey (2009).

[2.6] D. J. Craik, *Magnetic oxides*, Wiley-Interscience, London (1975).

[2.7] A. Goldman, *Modern Ferrite Technology, 2nd ed.*, Springer, New York (2006).

[2.8] S. Laurent, D. Forge, M. Port, A. Roch, C. Robic, L. V. Elst, R. N. Muller, *Chem. Rev.* 108, 2064 (2008).

[2.9] R. F. Ziolo, E. P. Giannelis, B. A. Weinstein, M. P. O'Horo, B. N. Ganguly, V. Mehrotra, M. W. Russell, D. R. Huffman, *Science* 257, 219 (1992).

[2.10] J. Park, K. An, Y. Hwang, J.-G. Park, H.-J. Noh, J.-Y. Kim, J.-H. Park, N.-M. Hwang, T. Hyeon, *Nat. Mater.* 3, 891 (2004).

[2.11] T. Sharifi, E. Gracia-Espino, H. R. Barzegar, X. Jia, F. Nitze, G. Hu, P. Nordblad, C.-W. Tai, T. Wågberg, *Nat. Commun.* 4, 2319 (2013).

[2.12] F. X. Redl, K.-S. Cho, C. B. Murray, S. O'Brien, *Nature* 423, 968 (2003).

[2.13] C. M. Eggleston, *Science* 320, 184 (2008).

[2.14] H. Dotan, O. Kfir, E. Sharlin, O. Blank, M. Gross, I. Dumchin, G. Ankonina, A. Rothschild, *Nat. Mater.* 12, 158 (2013).

[2.15] J. Li, S. K. Cushing, P. Zheng, F. Meng, D. Chu, N. Wu, *Nat. Commun.* 4, 2651 (2013).

[2.16] Y. Hou, D. Wang, X. H. Yang, W. Q. Fang, B. Zhang, H. F. Wang, G. Z. Lu, P. Hu, H. J. Zhao, H. G. Yang, *Nat. Commun.* 4, 1583 (2013).

[2.17] G. Klingelhöfer, R. V. Morris, B. Bernhardt, C. Shröder, D. S. Rodionov, P. A. de Souza Jr., A. Yen, R. Gellert, E. N. Evlanov, B. Zubkov, J. Foh, U. Bonnes, E. Kankeleit, P. Gütlich, D. W. Ming, F. Renz, T. Wdowiak, S. W. Squyres, R. E. Arvidson, *Science* 306, 1740 (2004).

[2.18] R. V. Jagadeesh, A.-E. Surkus, H. Junge, M.-M. Pohl, J. Radnik, J. Rabeah, H. Huan, V. Schünemann, A. Brückner, M. Beller, *Science* 342, 1073 (2013).

[2.19] I. Dzyaloshinsky, *J. Phys. Chem. Solids* 4, 241 (1958).

[2.20] T. Moriya, *Phys. Rev. Lett.* 4, 228 (1960).

[2.21] S. Chikazumi, *Physics of Ferromagnetism*, Clarendon Press, Oxford (1997).

[2.22] H. Braun, K. J. Gallagher, *Nature-Phys. Sci.* 240, 13 (1972)

[2.23] S. Sakurai, A. Namai, K. Hashimoto, S. Ohkoshi, *J. Am. Chem. Soc.* 131, 18299 (2009).

[2.24] R. Zboril, L. Machala, M. Mashlan, V. Sharma, *Cryst. Growth Des.* 4, 1317 (2004).

[2.25] J. Tuček, R. Zbořil, A. Namai, S. Ohkoshi, *Chem. Mater.* 22, 6483 (2010).

[2.26] E. Tronc, C. Chanéac, J. P. Jolivet, *J. Solid State Chem.* 139, 93 (1998).

[2.27] J. Jin, S. Ohkoshi, K. Hashimoto, *Adv. Mater.* 16, 48 (2004).

[2.28] A. Namai, M. Yoshikiyo, K. Yamada, S. Sakurai, T. Goto, T. Yoshida, T. Miyazaki, M. Nakajima, T. Suemoto, H. Tokoro, S. Ohkoshi, *Nat. Commun.* 3, 1035 (2012).

[2.29] M. Kurmoo, J.-L. Rehspringer, A. Hutlova, C. D'Orléans, S. Vilminot, C. Estournès, D. Niznansky, *Chem. Mater.* 17, 1106 (2005).

[2.30] S. Ohkoshi, S. Kuroki, S. Sakurai, K. Matsumoto, K. Sato, S. Sasaki, *Angew. Chem. Int. Ed.* 46, 8392 (2007).

[2.31] M. Gich, I. Fina, A. Morelli, F. Sánchez, M. Alexe, J. Gàzquez, J. Fontcuberta, A. Roig, *Adv. Mater.* 26, 4645 (2014).

[2.32] S. Ohkoshi, A. Namai, K. Imoto, M. Yoshikiyo, W. Tarora, K. Nakagawa, M. Komine, Y. Miyamoto, T. Nasu, S. Oka, H. Tokoro, *Sci. Rep.* 5, 14414 (2015).

[2.33] Y. Kusano, T. Fujii, J. Takeda, M. Fukuhara, A. Doi, Y. Ikeda, M. Takano, *Chem. Mater.* 20, 151 (2008).

[2.34] E. Taboada, M. Gich, A. Roig, *ACS Nano* 3, 3377 (2009).

[2.35] K. Parlinski, Z. Q. Li, Y. Kawazoe, *Phys. Rev. Lett.* 78, 4063 (1997).

Figures and Tables

Table 2.1 Crystallographic data and atomic positions of the mesoscopic ε-Fe_2O_3 rods obtained by Rietveld refinement of the XRD pattern. [Adapted with permission from Sci. Rep., 6, 27212 (2016). Copyright 2016 Springer Nature.]

Crystal system	Orthorhombic		
Space group	*Pna*2$_1$ (No.33)		
a (Å)	5.08923(16)		
b (Å)	8.7858(3)		
c (Å)	9.4766(2)		
V (Å^3)	423.73(2)		
Density (g cm^{-3})	5.01		
Z	8		
R_{wp} (%)	0.85		
S	1.4081		
	x / *a*	*y* / *b*	*z* / *c*
Fe_A	0.315(4)	0.347(3)	0.1561(8)
Fe_B	0.3204(17)	0.0322(8)	0.369(3)
Fe_C	0.3085(16)	0.6606(11)	0.371(2)
Fe_D	0.196(4)	0.845(4)	0.071(2)
O1	0.992(6)	0.003(4)	0.997(5)
O2	0.038(7)	0.337(5)	0
O3	1.018(8)	0.661(6)	0.015(4)
O4	0.166(10)	0.497(4)	0.276(3)
O5	0.166(11)	0.837(6)	0.2720(16)
O6	0.163(13)	0.166(7)	0.246(5)

Table 2.2 Optical phonon modes. Energy in frequency and wavenumber, symmetry, and activities of Raman and IR. [Adapted with permission from Sci. Rep., 6, 27212 (2016). Copyright 2016 Springer Nature.]

No.	THz	cm^{-1}	symmetry	Raman	IR
1	2.51	83.6	A_1	○	○
2	2.82	94.0	A_2	○	–
3	3.18	106.0	B_2	○	○
4	3.61	120.3	A_2	○	–
5	3.62	120.7	B_1	○	○
6	3.62	120.8	A_1	○	○
7	3.73	124.3	B_1	○	○
8	3.80	126.8	A_1	○	○
9	4.01	133.7	A_2	○	–
10	4.27	142.5	B_1	○	○
11	4.34	144.6	B_2	○	○
12	4.40	146.7	A_1	○	○
13	4.65	154.9	B_2	○	○
14	4.65	155.0	A_2	○	–
15	4.67	155.7	A_1	○	○
16	5.04	168.0	A_2	○	–
17	5.10	169.9	B_2	○	○
18	5.14	171.3	A_1	○	○
19	5.16	172.1	B_1	○	○
20	5.28	176.1	A_2	○	–
21	5.51	183.8	B_2	○	○
22	5.92	197.5	B_1	○	○
23	5.96	198.8	A_2	○	–
24	6.02	200.6	A_1	○	○
25	6.19	206.4	B_2	○	○
26	6.34	211.4	A_2	○	–
27	6.42	214.3	B_1	○	○
28	6.69	223.1	B_1	○	○
29	6.83	228.0	A_1	○	○
30	6.84	228.0	B_2	○	○
31	6.91	230.6	B_1	○	○
32	6.92	230.9	A_1	○	○
33	6.99	233.2	A_2	○	–
34	7.06	235.6	B_2	○	○
35	7.35	245.0	A_2	○	–
36	7.38	246.1	B_1	○	○
37	7.67	255.9	B_2	○	○
38	7.73	257.8	B_1	○	○
39	7.85	261.7	A_2	○	–
40	7.87	262.4	A_1	○	○
41	8.09	269.7	B_2	○	○
42	8.20	273.5	B_1	○	○
43	8.20	273.7	B_1	○	○
44	8.40	280.2	A_2	○	–
45	8.43	281.3	A_1	○	○
46	8.61	287.2	B_2	○	○
47	8.63	287.9	B_1	○	○
48	8.75	291.7	A_2	○	–
49	8.77	292.5	B_2	○	○
50	9.02	300.9	A_1	○	○
51	9.24	308.3	B_1	○	○
52	9.25	308.5	A_2	○	–
53	9.42	314.3	B_2	○	○
54	9.47	315.9	A_2	○	–
55	9.52	317.4	A_1	○	○
56	9.53	317.8	A_1	○	○
57	9.81	327.2	B_1	○	○
58	9.85	328.4	B_2	○	○
59	10.00	333.7	B_2	○	○
60	10.08	336.1	A_1	○	○
61	10.20	340.3	B_1	○	○
62	10.44	348.2	A_2	○	–
63	10.69	356.5	A_1	○	○
64	10.77	359.1	B_1	○	○
65	10.98	366.3	B_2	○	○
66	11.12	371.0	B_2	○	○
67	11.13	371.3	A_1	○	○
68	11.20	373.6	A_2	○	–
69	11.24	374.9	A_1	○	○
70	11.29	376.6	B_1	○	○
71	11.78	392.9	A_2	○	–
72	11.83	394.6	B_2	○	○
73	12.04	401.6	B_1	○	○
74	12.07	402.5	A_2	○	–
75	12.31	410.7	B_2	○	○
76	12.43	414.6	A_1	○	○
77	12.44	415.0	B_1	○	○
78	12.47	416.1	A_2	○	–
79	12.60	420.2	A_1	○	○
80	13.02	434.2	B_2	○	○
81	13.03	434.6	A_1	○	○
82	13.41	447.2	A_2	○	–
83	13.63	454.6	A_1	○	○
84	14.10	470.3	B_2	○	○
85	14.15	472.0	A_2	○	–
86	14.21	474.0	B_1	○	○
87	14.28	476.3	B_1	○	○
88	14.69	489.8	A_1	○	○
89	14.71	490.6	B_2	○	○
90	14.86	495.6	A_2	○	–
91	15.21	507.3	B_1	○	○
92	15.56	518.9	A_2	○	–
93	16.25	541.9	B_2	○	○
94	16.33	544.5	B_1	○	○
95	16.34	545.0	A_1	○	○
96	16.74	558.3	B_2	○	○
97	16.85	561.9	A_2	○	–
98	17.10	570.3	A_1	○	○
99	17.41	580.6	A_1	○	○
100	17.42	580.9	A_2	○	–
101	17.55	585.3	B_2	○	○
102	17.69	590.0	B_1	○	○
103	18.23	608.2	A_2	○	–
104	18.30	610.5	B_1	○	○
105	18.42	614.5	B_2	○	○
106	18.64	621.8	A_1	○	○
107	18.72	624.5	B_2	○	○
108	18.76	625.7	A_2	○	–
109	18.94	631.6	B_1	○	○
110	19.22	641.0	A_1	○	○
111	19.53	651.5	B_2	○	○
112	19.55	652.1	A_2	○	–
113	19.61	654.0	B_2	○	○
114	19.75	658.6	B_1	○	○
115	20.07	669.5	A_2	○	–
116	20.26	675.7	B_1	○	○
117	20.53	684.9	A_1	○	○

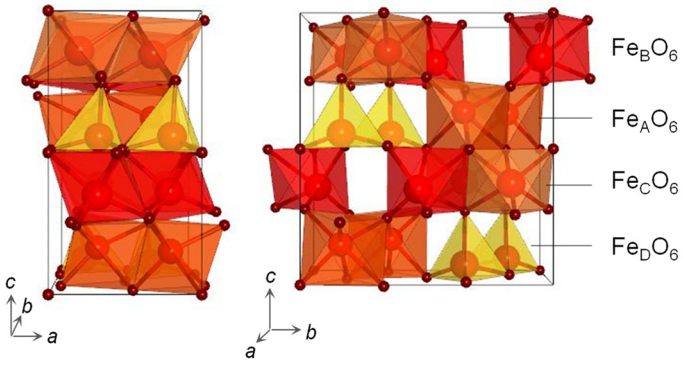

Figure 2.1 Crystallographic *b*-axis (left) and *a*-axis (right) views of the crystal structure of a mesoscopic ε-Fe_2O_3 rod. ε-Fe_2O_3 unit cell is orthorhombic ($Pna2_1$) with four nonequivalent Fe sites: Fe_AO_6 (red), Fe_BO_6 (crimson), Fe_CO_6 (orange), and Fe_DO_4 (yellow). [Adapted with permission from Sci. Rep., 6, 27212 (2016). Copyright 2016 Springer Nature.]

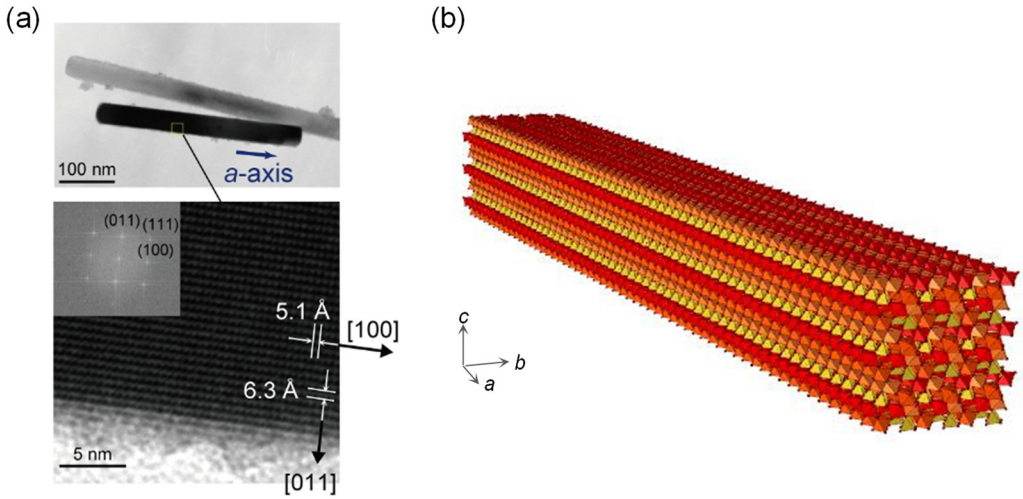

Figure 2.2 (a) HRTEM image where the longitudinal direction is along the crystallographic *a*-axis of ε-Fe_2O_3. Lower is the enlarged HRTEM and Fourier transformed (inset) images. (b) Depiction of the packing structure of a bar magnet. [Adapted with permission from Sci. Rep., 6, 27212 (2016). Copyright 2016 Springer Nature.]

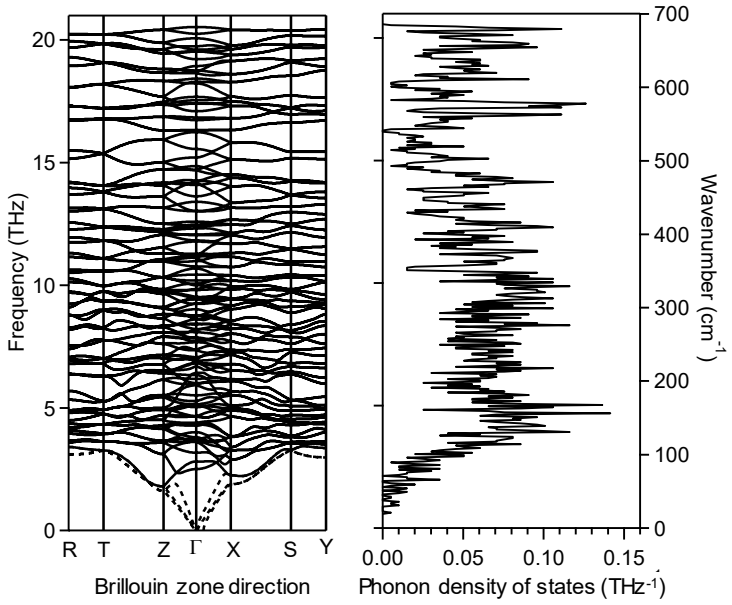

Figure 2.3 Calculated phonon mode spectrum from the phonon modes calculation of ε-Fe_2O_3. Phonon dispersion (lower left) and phonon density of states (lower right) of ε-Fe_2O_3. Solid and dotted lines of the phonon dispersion indicate optical phonon and acoustic phonon modes, respectively. [Adapted with permission from Sci. Rep., 6, 27212 (2016). Copyright 2016 Springer Nature.]

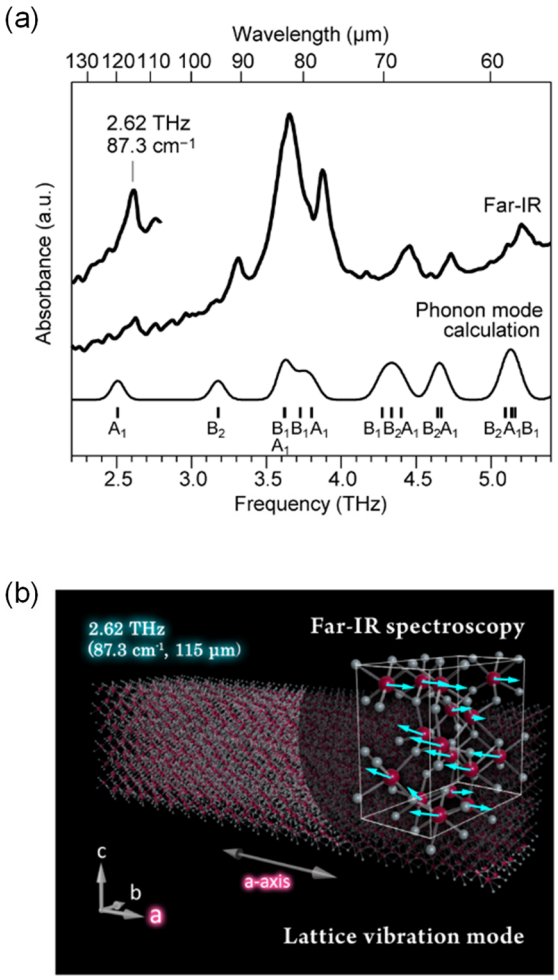

Figure 2.4 (a) Far-IR (thick lines) and calculated (thin line) spectra of ε-Fe_2O_3. Ticks denote calculated positions and vibrational symmetries of the phonon modes. (b) Atomic movement of the lowest frequency optical phonon mode of 2.62 THz (calc. 2.51 THz) with A_1 symmetry where Fe atoms vibrate in the longitudinal direction of the rod, which is parallel to the crystallographic *a*-axis. [Adapted with permission from Sci. Rep., 6, 27212 (2016). Copyright 2016 Springer Nature.]

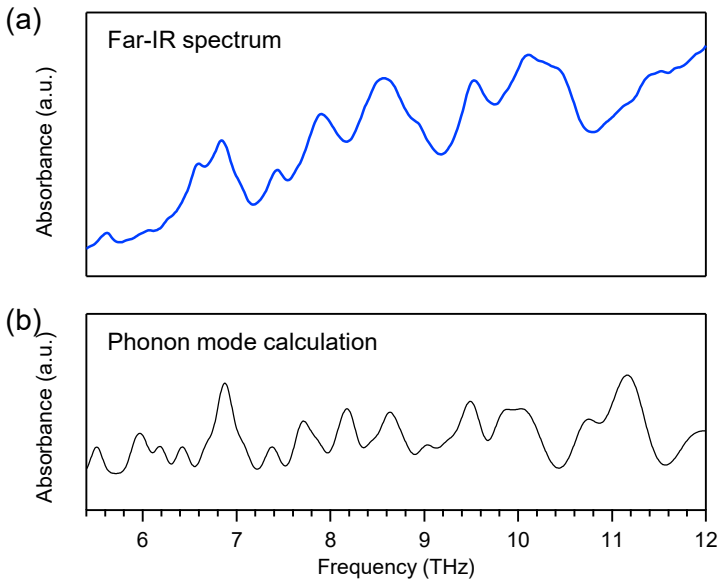

Figure 2.5 (a) Far-IR (thick lines) and calculated (thin line) spectra of ε-Fe_2O_3. Ticks denote calculated positions and vibrational symmetries of the phonon modes. [Adapted with permission from Sci. Rep., 6, 27212 (2016). Copyright 2016 Springer Nature.]

Chapter 3

Phonon mode calculations and lattice vibrations of ε-$Ga_xFe_{2-x}O_3$

Iron ferrites are found in a plethora of devices, including magnetic motors, magnetic recording media, magnetic fluids, and electromagnetic wave filters.[3.1–3.13] Of the four polymorphs of ferric oxide (Fe_2O_3), epsilon iron oxide (ε-Fe_2O_3) is intensely investigated due to its large coercive field of 25 kOe,[3.14,3.15] high-frequency millimeter-wave absorption,[3.16–3.18] and other useful properties.[3.19–3.28] Because its strong magnetic anisotropy supports downsizing to the sub-ten nanometer level, ε-Fe_2O_3 is the smallest hard magnetic ferrite discovered to date.[3.29]

Its physical properties have been investigated theoretically,[3.29–3.31] revealing, for example, that ε-Fe_2O_3 is a charge-transfer type insulator with a very wide bandgap.[3.29,3.30] Moreover, its strong magnetic anisotropy is attributed to the strong hybridization between Fe3d and O2p orbitals. Recently, the phonon modes have been calculated.[3.15]

Other studies have demonstrated that Fe^{3+} ion of ε-Fe_2O_3 can be substituted by other metal cations. Hence, its magnetic properties, optical properties, and millimeter-wave absorption properties can be tuned.[3.16–3.18,3.32,3.33] For example, rhodium-substituted ε-Fe_2O_3 enhances the coercive field to 31 kOe at room temperature, whereas indium-substituted ε-Fe_2O_3 exhibits a ferri-antiferromagnetic phase transition at a temperature that is about half of the Curie temperature. Moreover, gallium-substituted ε-Fe_2O_3 (ε-$Ga_{0.5}Fe_{1.5}O_3$) has a millimeter-wave absorption frequency, which is within the millimeter-wave radar frequency (76 GHz) for automobiles.

This study examines ε-$Ga_{0.5}Fe_{1.5}O_3$, where nonmagnetic Ga^{3+} ($S = 0$) replaces the

tetrahedral Fe^{3+} (S = 5/2) sites. First-principles phonon mode calculations are used to determine the phonon density of states, optical transition moments, and atomic movements. Magnetic measurements are carried out for a magnetically oriented film to investigate the magnetic property, and far- and mid-infrared (IR) and Raman spectroscopies reveal the optical phonon modes of ε-$Ga_{0.48}Fe_{1.52}O_3$ nanoparticles. Finally, the estimated thermodynamic parameters and the heat capacity measurements are compared.

3.1. Calculation and experimental details

For the first-principles phonon mode calculations, Phonon code[3.34] in the Material Design MedeA package was used to calculate the phonon modes of ε-$Ga_{0.5}Fe_{1.5}O_3$ via the direct method implemented with 2-pm displacements and 2×1×1 supercell optimized structures. The Vienna *ab initio* Simulation Package (VASP)[3.35,3.36] with a 520-eV energy cut-off and 5×3×3 *k*-mesh was used in the optimization, which continued until the 10^{-5} eV pm^{-1} force tolerance was satisfied. To calculate the transition moment for IR activity, longitudinal phonon modes and transversal phonon modes were split. The electronic energy of formation in reference to elements in the standard state was calculated using the standard generalized gradient approximation (GGA).

Synthesis of gallium-substituted ε-Fe_2O_3 with formulas close to ε-$Ga_{0.5}Fe_{1.5}O_3$ was done using the sol–gel technique reported in the literature.[3.16] Briefly, a NH_3 aqueous solution (1.3 mol dm^{-3}) was added to a mixed aqueous solution of $Fe(NO_3)_3$ (0.26 mol dm^{-3}) and $Ga(NO_3)_3$ (0.08 mol dm^{-3}) with rapid stirring. Adding tetraethoxysilane dropwise to the solution formed a silica matrix around the Fe, Ga hydroxide. After stirring for 20 h, the precipitate was extracted, washed, dried, and sintered in air at 1100 °C for 4

hours. The silica matrix was removed by chemical etching using a NaOH solution.

Two lots were synthesized, and elemental analyses were carried out using inductively coupled plasma-atomic emission spectroscopy (ICP-AES, Jarrel-Ash, IRIS/AP). The chemical formulas were determined to be $Ga_{0.45}Fe_{1.55}O_3$ (sample **1**) and $Ga_{0.48}Fe_{1.52}O_3$ (sample **2**). For samples **1** and **2**, JEOL 100CXII was used for transmission electron microscopy (TEM) measurements. Rigaku Ultima IV with Cu Kα radiation (λ = 1.5406 Å) at room temperature was employed to measure X-ray diffraction (XRD) profiles. Superconducting quantum interference device (SQUID) magnetometer (Quantum Design, MPMS 7) was used to assess magnetic properties. For sample **1**, JASCO FT-IR 6100 spectrometer was used to record the far-IR spectra (60–600 cm^{-1}) for samples rubbed on polyethylene plates in a vacuum chamber at room temperature. SHIMADZU FTIR-8200PC was used to collect the mid-IR spectra for pellets of ε-$Ga_{0.48}Fe_{1.52}O_3$ powder samples dispersed in KBr. Raman micro-spectrometer (JASCO NRS-5100) was used to acquire the Raman spectra. Physical property measurement system (PPMS) was used to measure the heat capacity.

To investigate the details of the magnetic property, a magnetically oriented thin film was prepared using sample **1**. For the film preparation, first, a mixed solution of urethane resin, acetylacetone, butyl stearate, and cyclohexanone, was stirred until homogeneous. Then a vinyl chloride polymer was added. After stirring overnight to remove agglomerations and bubbles, cyclohexanone was added to dilute the solution. Next, sample **1** was added, and the mixed solution of toluene and 2-butanone was stirred by shaking with zirconia beads in a plastic container. The obtained dispersion solution was dropped onto the surface of the polyester film supported on a glass plate, which was then placed in a superconducting magnet to apply an external magnetic field in the out-of-

plane direction of the film.

3.2. Results and discussion

ε-Fe_2O_3 has an orthorhombic structure (*Pna*2_1 space group) with four non-equivalent metal cation sites.[3.16] Similarly, ε-$Ga_{0.5}Fe_{1.5}O_3$ has four non-equivalent Fe^{3+} sites: Fe(A), Fe(B), and Fe(C) sites (octahedral) and Fe(D) site (tetrahedral). There are also six different O sites [O(1)–O(6)] (Figs. 3.1 a,b). Table 3.1 shows the atomic positions optimized by first-principles calculation.

First-principles phonon mode calculations showed that ε-$Ga_{0.5}Fe_{1.5}O_3$ has 117 optical phonon modes (fundamental vibrations) and 3 acoustic phonon modes (Table 3.2). There are four Raman active symmetries (A_1, A_2, B_1, and B_2) and three IR active ones (A_1, B_1, and B_2) (Table 3.2). The phonon modes in the low energy region of 20–370 cm^{-1} are due to the heavy elements (Fe and Ga). In contrast, the light element (O) contributes to the phonon modes in the energy range of 370–720 cm^{-1} (Fig. 3.2). Interestingly, Ga(D) and O(3), which are connected, impact the density of states in the high energy range of 570–720 cm^{-1} (Fig. 3-3b).

The lowest and highest energy transitions in the IR active phonon modes are at 87.79 cm^{-1} (A_1) and 725.9 cm^{-1} (B_1), respectively (Table 3.2 and Fig. 3.3). Of the 117 optical phonon modes between these energies, the following optical transitions have strong absorbances: 87.79 (A_1), 110.5 (B_2), 126.7 (A_1), 142.2 (B_2), 154.5 (B_2), 170.9 (B_2), 187.5 (B_2), 203.1 (B_1), 226.4 (B_2), 252.9 (B_2), 269.3 (B_2), 292.3 (B_2), 316.0 (B_1), 349.4 (B_2), 387.1 (B_2), 428.3 (B_1), 488.7 (B_2), 504.2 (B_2), 580.7 (B_2), 616.7 (B_1), 705.9 (B_2), and 725.9 cm^{-1} (B_1).

Figure 3-5 shows the calculated IR spectrum. In the phonon mode at 87.79 cm^{-1}

(A_1), the layers, which are parallel to the *ab*-plane and contain the Fe and Ga atoms, shift in the *a*-axis direction (Figs. 3.4 and 3.5a). For B_2 at 226.4 cm^{-1}, the two at D sites (Ga(D)–O(3) and Ga(D)O_4) twist and are accompanied by the bending mode of O(3)–Fe(B)–O(6) (Fig. 3.5b). The two bonds (Ga(D)–O(1) and Ga(D)–O(5)) at the tetrahedral Ga(D)O_4 site for B_2 at 387.1 cm^{-1} twist, stretch, and are accompanied by the bending mode of O(1)–Fe(C)–O(4) (Fig. 3.5c). Hence, Fe and Ga atoms contribute to the lattice vibrations in the low energy phonon modes. However, O movements are more influential in the higher energy region, as evidenced for B_1 at 428.3 cm^{-1}, which is a bending mode of O(1)–Ga(D)–O(5) at the tetrahedral Ga(D)O_4 site (Fig. 3.5d). For A_1 at 695.9 cm^{-1}, three bonds (Ga(D)–O(1), Ga(D)–O(3), and Ga(D)–O(5)) stretch simultaneously, altering the size of the Ga(D)O_4 tetrahedron. In a breathing-mode manner, the neighboring tetrahedra expand and contract in phase with each other (Fig. 3.5e). For B_1 at 725.9 cm^{-1}, the stretching mode of Fe(A)–O(4), Fe(A)–O(6), and Ga(D)–O(5) causes the O-containing plane parallel to the *ab*-plane to elevate in the *c*-axis direction (Figs. 3.5c and 3.5f).

The calculated thermodynamic parameters give a vibrational internal energy (U_{vib}) of 32.8 kJ mol^{-1} and a formation energy of −659.9 kJ mol^{-1} for the electronic structure (U_0) (Fig. 3.6). Their sum gives an internal energy (U) of −627.1 kJ mol^{-1} at 0 K. Due to phonon excitation, the internal energy increases as the temperature increases. Moreover, as the temperature increases, the vibrational entropy (S_{vib}) increases, but the Helmholtz energy (A) decreases due to the contribution of S_{vib}. At 300 K, the Helmholtz energy is −638.8 kJ mol^{-1}.

Morphologies of samples **1** and **2** were investigated by TEM. The samples were composed of spherical particles with average sizes of 25 ± 11 nm for sample **1**, and 32 ±

15 nm for sample **2** (insets of Figs. 3.7a, 3.8a). Crystal structures were characterized by XRD measurement and Rietveld analyses. Both samples were analyzed as a pure epsilon phase (Figs. 3.7a, 3.8a). The Ga ions mainly occupy the tetrahedral D site among the four nonequivalent cation sites (Tables 3.3, 3.4). The magnetic hysteresis loops of the randomly oriented powder samples were measured at room temperature. Saturation magnetization values at 5 Tesla were 28.7 emu g^{-1} (**1**) and 25.6 emu g^{-1} (**2**), and the coercive field values were 7.9 kOe (**1**) and 6.7 kOe (**2**) (Figs. 3.7b, 3.8b).

Details of the magnetic property were investigated using a magnetically oriented thin film composed of sample **1**. To determine the orientation direction of the magnetic nanoparticles, XRD measurement of the film was carried out. The XRD pattern contains one strong peak from the 200 reflection and weak peaks from the 122, 201, and 330 reflections (Fig. 3.8a), indicating that the *a*-axes of the magnetic nanoparticles are aligned in the out-of-plane direction of the film. Comparing the XRD peak intensities of the *hkl* reflections of the oriented sample ($I_o(hkl)$) to those of the non-oriented sample ($I_n(hkl)$) determined the degree of orientation (Table 3.4). The Lotgering factor (*F*), indicating the degree of orientation, is derived as:

$$F = \left(\frac{I_o(200)}{\sum I_o(hkl)} - \frac{I_n(200)}{\sum I_n(hkl)}\right) \Big/ \left(1 - \frac{I_n(200)}{\sum I_n(hkl)}\right). \qquad (2.1)$$

Using Eq. (2.1), the ε-$Ga_{0.45}Fe_{1.55}O_3$ film exhibits a high *F* factor of 0.94. The magnetic hysteresis loop was measured with the measurement magnetic field parallel to the out-of-plane direction of the film (Fig. 3.8b). A rectangular magnetic hysteresis was obtained with an H_c value of 9.7 kOe and magnetization value at 7T of 30.4 emu g^{-1}.

Next, IR measurement was carried out using sample **2**. Similar to the phonon mode calculations, the IR spectra below 200 cm^{-1} showed eight peaks (92, 113, 127, 131, 151, 159, 175, and 188 cm^{-1}) (Fig. 3.9a). For example, the peak at 92 cm^{-1} corresponds to the

atomic movement of the phonon mode calculated at 87.79 cm^{-1} (Fig. 3.5a). Six peaks are present between 200–400 cm^{-1} (222, 264, 296, 324, 352, and 389 cm^{-1}). The one at 222 cm^{-1} (389 cm^{-1}) is attributed to the atomic movement of the phonon modes calculated at 226.4 cm^{-1} (387.1 cm^{-1}) (Fig. 3.5b, c). Two large broad peaks exist near 440 cm^{-1} and 500 cm^{-1}. That at 440 cm^{-1} is due to the atomic movement of the phonon mode calculated at 428.3 cm^{-1} (Fig. 3.5d). The higher IR range has four peaks (635, 663, 698, and 727 cm^{-1}). The peak at 698 cm^{-1}(727 cm^{-1}) is assigned to the atomic movements of the phonon modes calculated at 695.9 cm^{-1} (725.9 cm^{-1}) (Fig. 3.5e, f). These high-energy phonon modes are attributed to the movements of Ga(D) and its surrounding O.

The Raman spectrum of sample **2** showed 17 strong peaks (93, 123, 151, 158, 176, 205, 239, 258, 302, 360, 389, 454, 507, 567, 655, 687, and 741 cm^{-1}) (Fig. 3.9b). Those observed at 93, 176, 360, 687, and 741 cm^{-1} are much stronger than the calculated ones. The Raman peaks at 93, 176, and 360 cm^{-1} correspond to the calculated Raman active modes at 97.77 cm^{-1} (A_2) (Fig. 3.5g), 173.9 cm^{-1} (A_2), and 363.4 cm^{-1} (A_2), respectively. The highest energy peaks at 687 and 741 cm^{-1} are stronger than the IR spectrum calculated using the Raman active phonon modes at 672.3 cm^{-1} (A_2) and 705.6 cm^{-1} (A_2) (Fig. 3.5h).

The heat capacity (C_p) of sample **2** was used to calculate the thermodynamic parameters (Fig. 3.10b). The calculated $C_{v,vib}$ curve agrees well with the observed C_p plots. The plots can be reproduced using an equation based on the two-Debye model,[3.37] which is expressed as

$$C_{v,vib}(T) = \sum_{i=1}^{2} 9Rc_i(T/\theta_i)^3 \int_0^{\theta_i/T} x^4 e^x/(e^x\text{-}1)^2 dx \qquad (2.2)$$

where R is the gas constant, c_i is the coefficient, θ_i is the Debye temperature, x is $\hbar\omega/k_B T$, $\hbar$ is the reduced Planck constant, ω is phonon frequency, and k_B is the Boltzmann constant.

The refined parameters of Eq. (2.2) are c_1 = 3.77(6), c_2 = 1.67(9), θ_1 = 8.5(18) × 102 K, and θ_2 = 3.24(8) × 102 K. Additionally, the enthalpy (H), entropy (S), and Gibbs energy (G) can be derived by transforming the observed C_p values and the fitted curve (Fig. 3.10a, c, d) using equations (2.3) – (2.5):

$$H(T) = H(0) + \int_0^T C_P(T)\mathrm{d}T \quad (2.3)$$

$$S(T) = \int_0^T C_P(T)\mathrm{d}lnT \quad (2.4)$$

$$G(T) = H(T)\text{-}TS(T) \quad (2.5)$$

Assuming that Gibbs energy can approximate the Helmholtz energy for a solid material, the obtained curves and the calculated thermodynamic parameters of U, $C_{V,vib}$, S_{vib}, and A from the first-principles phonon mode calculations agree well.

3.3. Chapter summary

ε-$Ga_{0.5}Fe_{1.5}O_3$, a distinct and useful analog of ε-Fe_2O_3 for industrial applications, holds promise as a millimeter-wave absorber in car radars. ε-$Ga_{0.5}Fe_{1.5}O_3$ has 117 optical phonon modes (fundamental vibrations) with symmetries of A_1, A_2, B_1, and B_2. The lower energy region is influenced by the movements of Fe and Ga, while the higher energy region is affected by the movements of O. The observed and calculated spectra agree well. Additionally, the phonon modes reveal the thermodynamic properties.

References

[3.1] K. J. Standley, *Oxide Magnetic Materials*, *2nd ed.*, Clarendon Press, Oxford (1972).

[3.2] J. Smit, *Magnetic properties of materials*, Mcgraw-Hill, New York (1971).

[3.3] D. J. Craik, *Magnetic Oxides*, Wiley, London (1975).

[3.4] Z. G. Zhou, *Magnetic Ferrite Materials*, Science Press, Beijing (1981).

[3.5] K. H. J. Buschow, *Handbook of Magnetic Materials*, Elsevier, Amsterdam, Vol. 8 (1995).

[3.6] É. T. Lacheisserie, D. Gignoux, M. Schlenker, *Magnetism: II-Materials and Applications*, Kluwer, Norwell (2002).

[3.7] R. M. Cornell, U. Schwertmann, *The Iron Oxide: Structure, Properties, Reactions, Occurrence and Uses*, Wiely-VCH, Weinheim (2003).

[3.8] A. Goldman, *Modern Ferrite Technology*, *2nd ed*., Springer, New York (2006).

[3.9] B. D. Cullity, C. D. Graham, *Introduction to Magnetic Materials*, *Second Edition*, Wiley-IEEE Press, Hoboken (2008).

[3.10] J. M. D. Coey, *Magnetism and Magnetic Materials*, Cambridge University Press, Cambridge (2010).

[3.11] J. David, *Introduction to magnetism and magnetic materials*, CRC Press, Boca Raton (2015).

[3.12] J. Tuček, R. Zbořil, A. Namai, S. Ohkoshi, *Chem. Mater*. 22, 6483 (2010).

[3.13] S. Sakurai, A. Namai, K. Hashimoto, S. Ohkoshi, *J. Am. Chem. Soc*. 131, 18299 (2009).

[3.14] J. Jin, S. Ohkoshi, K. Hashimoto, *Adv. Mater.* 16, 48 (2004).

[3.15] S. Ohkoshi, A. Namai, T. Yamaoka, M. Yoshikiyo, K. Imoto, T. Nasu, S. Anan, Y. Umeta, K. Nakagawa, H. Tokoro, *Sci. Rep.* 6, 27212 (2016).

[3.16] S. Ohkoshi, S. Kuroki, S. Sakurai, K. Matsumoto, K. Sato, S. Sasaki, *Angew. Chem. Int. Ed*. 46, 8392 (2007).

[3.17] A. Namai, S. Sakurai, M. Nakajima, T. Suemoto, K. Matsumoto, M. Goto, S. Sasaki, S. Ohkoshi, *J. Am. Chem. Soc.* 131, 1170 (2009).

[3.18] A. Namai, M. Yoshikiyo, K. Yamada, S. Sakurai, T. Goto, T. Yoshida, T. Miyazaki, M. Nakajima, T. Suemoto, H. Tokoro, S. Ohkoshi, *Nat. Commun.* 3, 1035 (2012).

[3.19] E. Tronic, C. Chanéac, J. P. Jolivet, J. M. Grenèche, *J. Appl. Phys*. 98, 053901 (2005).

[3.20] M. Kurmoo, J.-L. Rehspringer, A. Hutlova, C. D'Orléans, S. Vilminot, C. Estournès, D. Niznansky, *Chem. Mater.* 17, 1106 (2005).

[3.21] T. Nakamura, Y. Yamada, K. Yano, *J. Mater. Chem.* 16, 2417 (2006).

[3.22] Y. Ding, J. R. Morber, R. L. Snyder, Z. L. Wang, *Adv. Funct. Mater.* 17, 1172 (2007).

[3.23] Y. Kusano, T. Fujii, J. Takada, M. Fukuhara, A. Doi, Y. Ikeda, M. Takano, *Chem. Mater*. 20, 151 (2008).

[3.24] Y.-C. Tseng, N. M. Souza-Neto, D. Haskel, M. Gich, C. Frontera, A. Roig, M. Veenendaal, J. Nogués, *Phys. Rev. B* 79, 094404 (2009).

[3.25] D. A. Balaev, I. S. Poperechny, A. A. Krasikov, K. A. Shaikhutdinov, A. A. Dubrovskiy, S. I. Popkov, A. D. Balaev, S. S. Yakushkin, G. A. Bukhtiyarova, O. N. Martyanov, Y. L. Raikher, *J. Appl. Phys.* 117, 063908 (2015).

[3.26] J. Kohout, P. Brázda, K. Závěta, D. Kubániová, T. Kmječ, L. Kubíčková, M. Klementová, E. Šantavá,; A. Lančok, *J. Appl. Phys.* 117, 17D505 (2015).

[3.27] J. López-Sánchez, A. Serrano, A. Del Campo, M. Abuín, *Chem. Mater.* 28, 511 (2016).

[3.28] S. Lee, H. Xu, *J. Phys. Chem. C* 120, 13316 (2016).

[3.29] S. Ohkoshi, A. Namai, K. Imoto, M. Yoshikiyo, W. Tarora, K. Nakagawa, M. Komine, Y. Miyamoto, T. Nasu, T. Oka, H. Tokoro, *Sci. Rep.* 5, 14414 (2015).

[3.30] M. Yoshikiyo, K. Yamada, A. Namai, S. Ohkoshi, *J. Phys. Chem. C* 116, 8688 (2012).

[3.31] A. Erlebach, H.-D. Kurland, J. Grabow, F. A. Müller, M. Sierka, *Nanoscale* 7, 2960 (2015).

[3.32] M. Yoshikiyo, A. Namai, M. Nakajima, K. Yamaguchi, T. Suemoto, S. Ohkoshi, *J. Appl. Phys.* 115, 172613 (2014).

[3.33] S. Ohkoshi, A. Namai, M. Yoshikiyo, K. Imoto, K. Tamasaki, K. Matsuno, O. Inoue, T. Ide, K. Masada, M. Goto, T. Goto, T. Yoshida, T. *Angew. Chem. Int. Ed.* 55, 11403 (2016).

[3.34] K. Parlinski, Z. Q. Li, Y. Kawazoe, *Phys. Rev. Lett.* 78, 4063 (1997).

[3.35] G. Kresse, J. Hafner, *Phys. Rev. B* 48, 13115 (1993).

[3.36] G. Kresse, J. Furthmüller, *Phys. Rev. B* 54, 11169 (1996).

[3.37] D. G. Tomuta, S. Ramakrishnan, G. J. Nieuwenhuys, J. A. Mydosh, *J. Phys.: Condens. Matter.* 13, 4543 (2001).

Figures and Tables

Table 3.1 Optimized atomic positions of ε-$Ga_{0.5}Fe_{1.5}O_3$ used in the phonon mode calculations. [Adapted with permission from J. Phys. Chem. C, 121, 5812 (2017). Copyright 2017 American Chemical Society.]

Crystal system		Orthorhombic	
Space group		$Pna2_1$	
a / Å		5.0887	
b / Å		8.7705	
c / Å		9.4353	
V / Å^3		421.10	
Z		4	
Atoms	x/a	y/b	z/c
Fe (A)	0.30841	0.34625	0.15780
Fe (B)	0.32114	0.03176	0.37189
Fe (C)	0.30667	0.65931	0.38236
Ga (D)	0.17701	0.84814	0.07460
O1	0.02019	0.32632	0.00396
O2	0.98483	0.01271	0.00881
O3	0.01811	0.66855	0.01449
O4	0.15435	0.49728	0.27405
O5	0.15532	0.84020	0.27188
O6	0.15319	0.16904	0.24935

Table 3.2 First-principles calculations of the optical phonon modes of ε-$Ga_{0.5}Fe_{1.5}O_3$. [Adapted with permission from J. Phys. Chem. C, 121, 5812 (2017). Copyright 2017 American Chemical Society.]

cm^{-1}	sym.	R	IR	cm^{-1}	sym.	R	IR	cm^{-1}	sym.	R	IR
87.79	A_1	○	○	265.3	A_1	○	○	432.4	B_2	○	○
97.77	A_2	○	–	269.3	B_2	○	○	450.2	A_1	○	○
110.5	B_2	○	○	270.8	B_1	○	○	452.6	B_2	○	○
118.8	A_2	○	–	280.6	B_1	○	○	464.3	A_2	○	–
121.6	A_1	○	○	283.1	A_2	○	–	471.5	A_1	○	○
121.9	B_1	○	○	286.5	A_1	○	○	488.7	B_2	○	○
123.5	B_1	○	○	292.3	B_2	○	○	488.8	B_1	○	○
126.7	A_1	○	○	293.7	B_1	○	○	494.4	A_2	○	–
132.8	A_2	○	–	300.2	B_2	○	○	504.2	B_2	○	○
142.2	B_2	○	○	301.7	A_2	○	–	509.9	A_2	○	–
143.9	A_1	○	○	305.1	A_1	○	○	512.9	B_1	○	○
145.4	B_1	○	○	309.3	A_2	○	–	514.5	A_1	○	○
154.0	A_1	○	○	316.0	B_1	○	○	534.4	B_1	○	○
154.5	B_2	○	○	318.9	A_2	○	–	545.9	A_2	○	–
159.3	A_2	○	–	320.1	A_1	○	○	564.6	B_2	○	○
165.2	A_2	○	–	328.6	B_2	○	○	580.7	B_2	○	○
170.9	B_2	○	○	336.4	B_2	○	○	585.7	A_1	○	○
172.3	A_1	○	○	339.9	A_1	○	○	590.8	A_2	○	–
173.9	A_2	○	–	342.8	B_1	○	○	592.5	A_2	○	–
174.6	B_1	○	○	349.4	B_2	○	○	604.2	A_1	○	○
187.5	B_2	○	○	352.6	B_1	○	○	612.8	B_1	○	○
197.5	A_1	○	○	353.5	A_1	○	○	616.7	B_1	○	○
202.6	B_1	○	○	362.3	A_1	○	○	624.2	B_2	○	○
203.1	B_1	○	○	363.4	A_2	○	–	625.3	A_1	○	○
203.4	A_2	○	–	377.4	B_2	○	○	637.2	B_2	○	○
207.7	B_2	○	○	378.7	A_1	○	○	641.1	A_1	○	○
217.3	A_2	○	–	380.4	B_1	○	○	642.4	B_1	○	○
223.2	B_1	○	○	386.8	A_2	○	–	647.7	B_2	○	○
224.2	A_1	○	○	387.1	B_1	○	○	649.4	A_2	○	–
226.4	B_2	○	○	387.1	B_2	○	○	654.4	B_1	○	○
233.0	A_2	○	–	391.9	A_1	○	○	663.3	A_2	○	–
235.3	B_2	○	○	403.1	B_2	○	○	670.2	B_2	○	○
235.5	B_1	○	○	408.0	A_2	○	–	672.3	A_2	○	–
239.3	A_1	○	○	409.8	B_1	○	○	675.6	A_1	○	○
243.6	A_2	○	–	419.4	A_2	○	–	680.8	B_1	○	○
252.9	B_2	○	○	423.4	A_1	○	○	695.8	A_1	○	○
253.9	B_1	○	○	428.3	B_1	○	○	705.6	A_2	○	–
260.5	B_1	○	○	430.7	A_2	○	–	705.9	B_2	○	○
263.0	A_2	○	–	432.4	A_1	○	○	725.9	B_1	○	○

Table 3.3 Rietveld analysis of the crystal structure parameters of sample **1**, ε-$Ga_{0.48}Fe_{1.52}O_3$. [Adapted with permission from J. Phys. Chem. C, 121, 5812 (2017). Copyright 2017 American Chemical Society.]

			ε-$Ga_{0.45}Fe_{1.55}O_3$	
Crystal system			Orthorhombic	
Space group			$Pna2_1$ (#33)	
a / Å			5.08822(18)	
b / Å			8.7748(3)	
c / Å			9.4383(3)	
V / Å^3			421.40(2)	
	x	*y*	*z*	Ga occupancy (%)
A	0.309(2)	0.3489(12)	0.1537(14)	0*
B	0.3227(9)	0.0321(4)	0.3631(15)	1
C	0.3077(7)	0.6579(5)	0.3770(14)	21
D	0.1775(14)	0.8473(10)	0.0723(14)	68
O_1	0.986(4)	0.007(2)	0.988(4)	
O_2	0.023(4)	0.326(3)	0	
O_3	0.008(4)	0.658(3)	0.012(2)	
O_4	0.164(4)	0.4944(2)	0.266(2)	
O_5	0.167(4)	0.833(3)	0.2652(15)	
O_6	0.156(4)	0.165(2)	0.233(2)	

Table 3.4 Rietveld analysis of the crystal structure parameters of sample **2**, ε-$Ga_{0.48}Fe_{1.52}O_3$. [Adapted with permission from J. Phys. Chem. C, 121, 5812 (2017). Copyright 2017 American Chemical Society.]

Crystal system	Orthorhombic			
Space group	$Pna2_1$			
a / Å	5.0881(2)			
b / Å	8.7733(4)			
c / Å	9.4347(3)			
V / Å^3	421.16(3)			
Z	4			
S	0.99			
Atoms	x	y	z	Ga Occpancy / %
Fe (A)	0.3187	0.3469	0.1566	0
Fe (B)	0.3236	0.0325	0.3623	0
Fe (C)	0.3104	0.6590	0.3771	24(2)
Fe (D)	0.1869	0.8471	0.0765	72(2)
O1	0.0243	0.3290	0.0000	
O2	0.9728	0.0123	0.0034	
O3	0.0075	0.6618	1.0074	
O4	0.1652	0.4992	0.2572	
O5	0.1713	0.8396	0.2576	
O6	0.1620	0.1655	0.2311	

Table 3.5 Peak intensities of the *hkl* reflections of the crystallographically oriented sample $I_o(hkl)$ and non-oriented sample $I_n(hkl)$ in the XRD pattern. [Adapted with permission from J. Phys. Chem. C, 121, 5812 (2017). Copyright 2017 American Chemical Society.]

hkl	$I_o(hkl)$	$I_n(hkl)$
1 2 2	188	93159
2 0 0	30491	14665
2 0 1	666	14642
2 1 0	141	3058
3 3 0	150	21177
4 0 1	480	2701

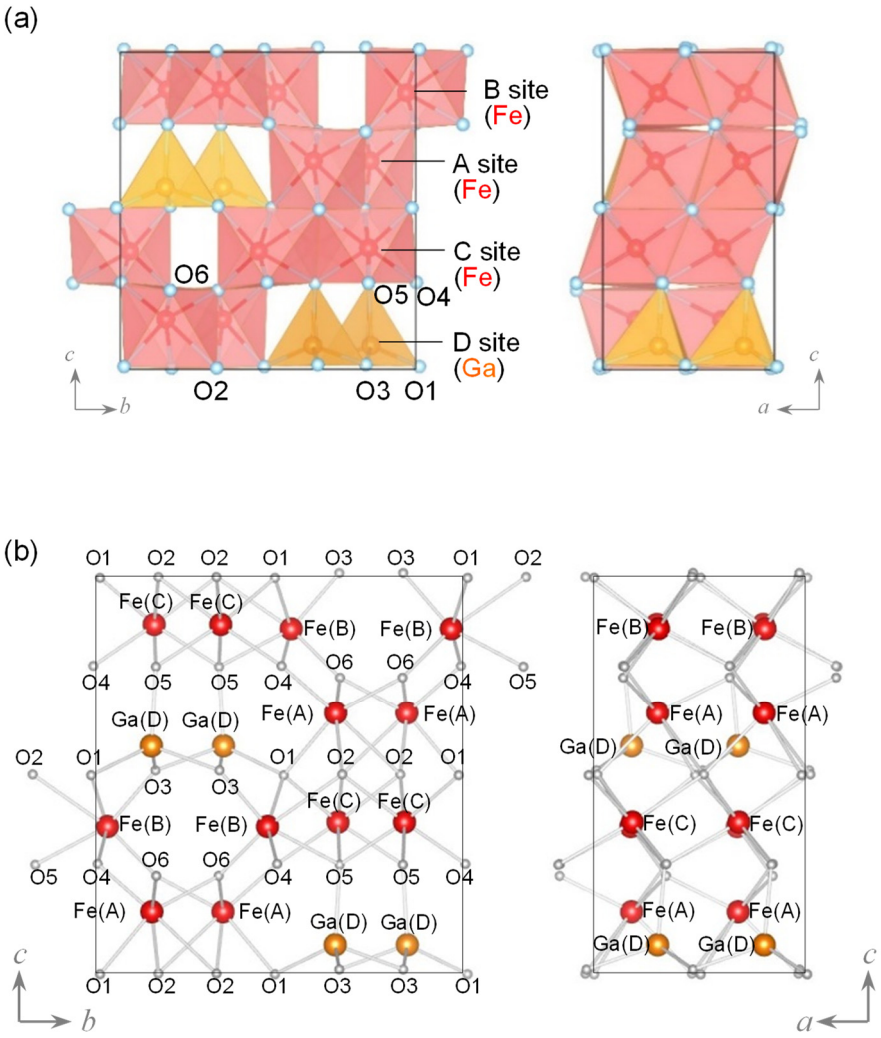

Figure 3.1 (a) Crystal structure of ε-$Ga_{0.5}Fe_{1.5}O_3$ depicted as polyhedra with Fe at A, B, and C sites (red), Ga at D sites (orange), and O sites (blue). (b) Ball and stick diagram of the crystal structure of ε-$Ga_{0.5}Fe_{1.5}O_3$ with Fe at A, B, and C sites (red), Ga at D sites (orange), and O sites (white). [Adapted with permission from J. Phys. Chem. C, 121, 5812 (2017). Copyright 2017 American Chemical Society.]

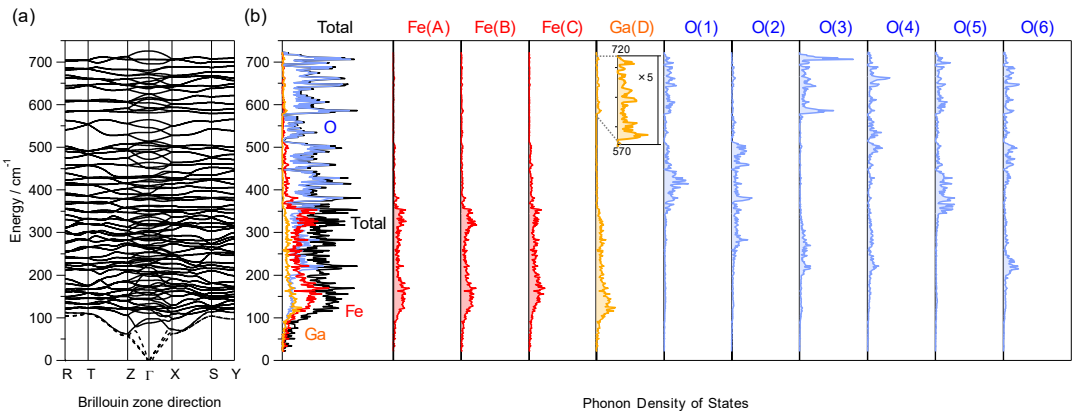

Figure 3.2 (a) Optical phonon dispersion (black lines) and acoustic phonon dispersion (dotted lines) of ε-$Ga_{0.5}Fe_{1.5}O_3$. (b) Calculated phonon density of states of ε-$Ga_{0.5}Fe_{1.5}O_3$ with the contributions of Fe (red), Ga (yellow), O (blue). Total phonon density of states (black) and partial phonon density of states of Fe(A)–Fe(C), Ga(D), and O(1)–O(6) sites are also shown. [Adapted with permission from J. Phys. Chem. C, 121, 5812 (2017). Copyright 2017 American Chemical Society.]

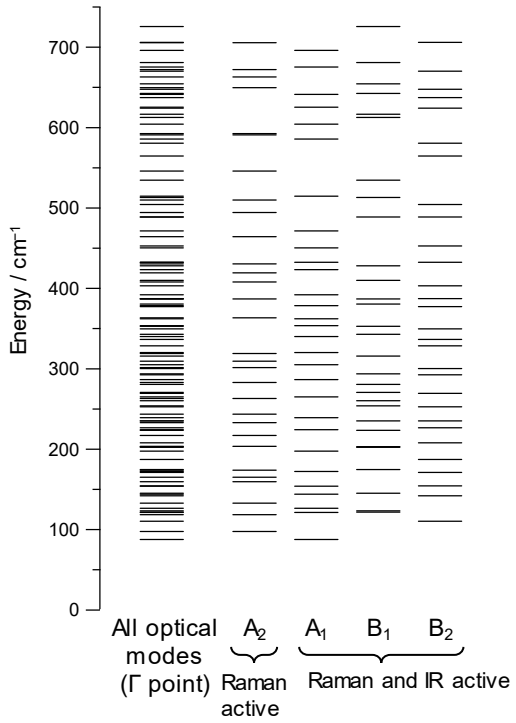

Figure 3.3 Energy diagram of the calculated optical phonon frequencies of ε-$Ga_{0.5}Fe_{1.5}O_3$ at the Γ point and each symmetry mode. [Adapted with permission from J. Phys. Chem. C, 121, 5812 (2017). Copyright 2017 American Chemical Society.]

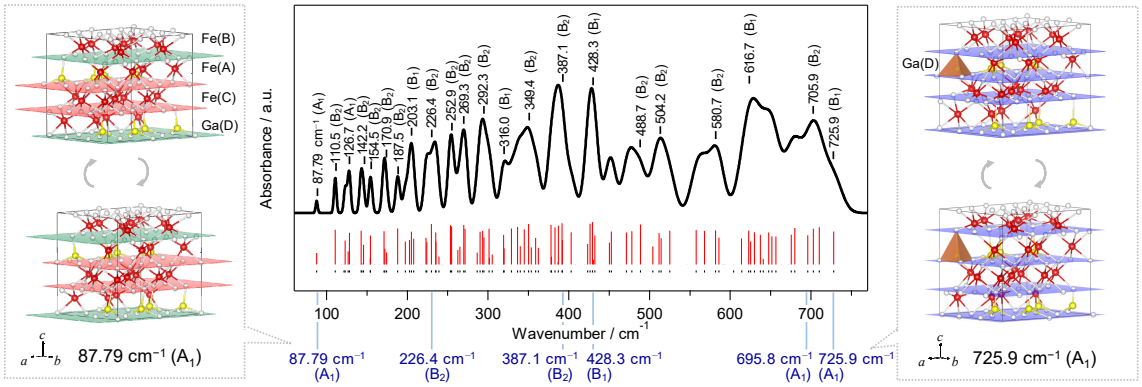

Figure 3.4 Atomic movements of Fe (red), Ga (yellow), and O (white) atoms for the representative phonon modes of ε-$Ga_{0.5}Fe_{1.5}O_3$ at 87.79 cm^{-1} (left) and 725.9 cm^{-1} (right). Center shows the calculated IR spectrum of ε-$Ga_{0.5}Fe_{1.5}O_3$ with the IR active modes (black tick marks) and IR intensities of the phonon mode (red bars). [Adapted with permission from J. Phys. Chem. C, 121, 5812 (2017). Copyright 2017 American Chemical Society.]

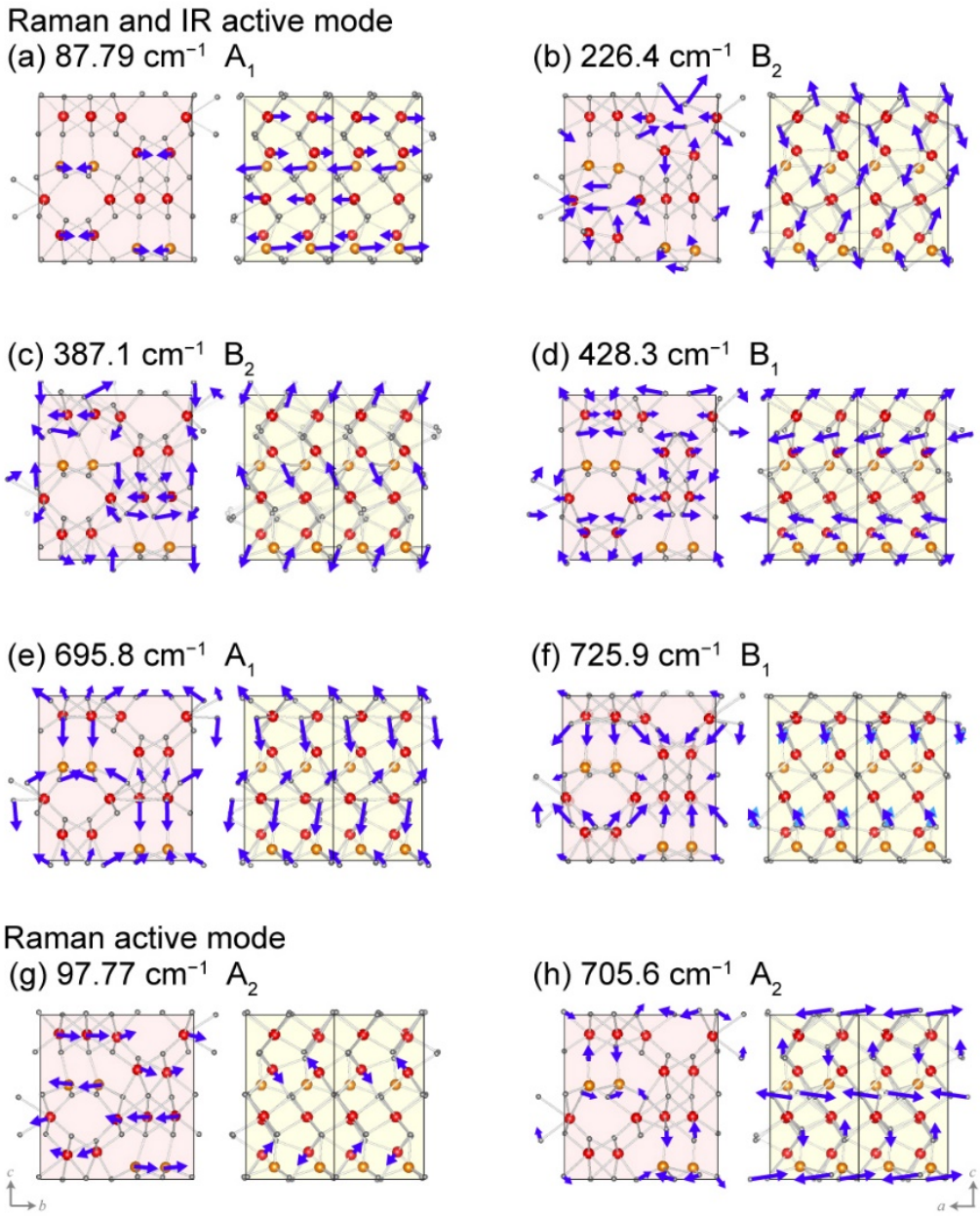

Figure 3.5 Atomic movements (blue arrows) of Fe (red), Ga (orange) and O (blue) atoms for representative phonon modes of ε-$Ga_{0.5}Fe_{1.5}O_3$ at (a) 87.79 cm^{-1}, (b) 226.4 cm^{-1}, (c) 387.1 cm^{-1}, (d) 428.3 cm^{-1}, (e) 695.8 cm^{-1}, (f) 725.9 cm^{-1}, (g) 97.77 cm^{-1}, and (h) 705.6 cm^{-1}. [Adapted with permission from J. Phys. Chem. C, 121, 5812 (2017). Copyright 2017 American Chemical Society.]

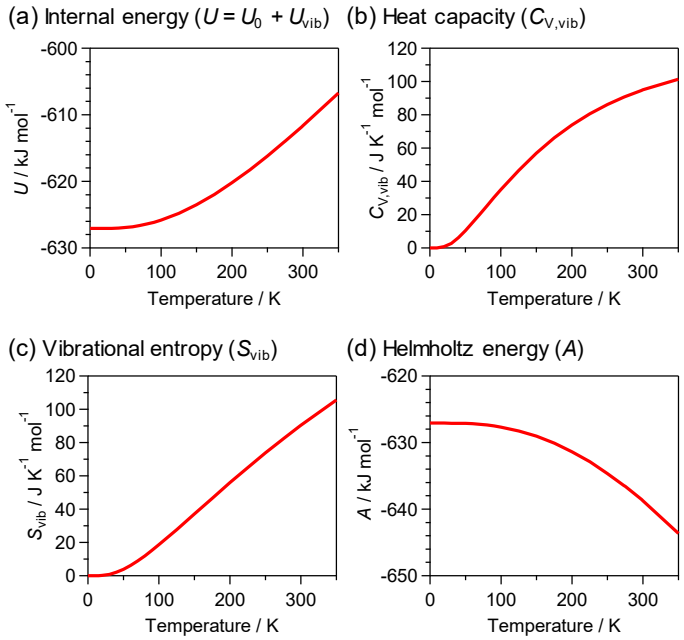

Figure 3.6 (a) Internal energy (U), (b) heat capacity ($C_{V,vib}$), (c) vibrational entropy (S_{vib}), and (d) Helmholtz energy (A) of ε-$Ga_{0.5}Fe_{1.5}O_3$ as functions of temperature obtained from first-principles phonon mode calculations. [Adapted with permission from J. Phys. Chem. C, 121, 5812 (2017). Copyright 2017 American Chemical Society.]

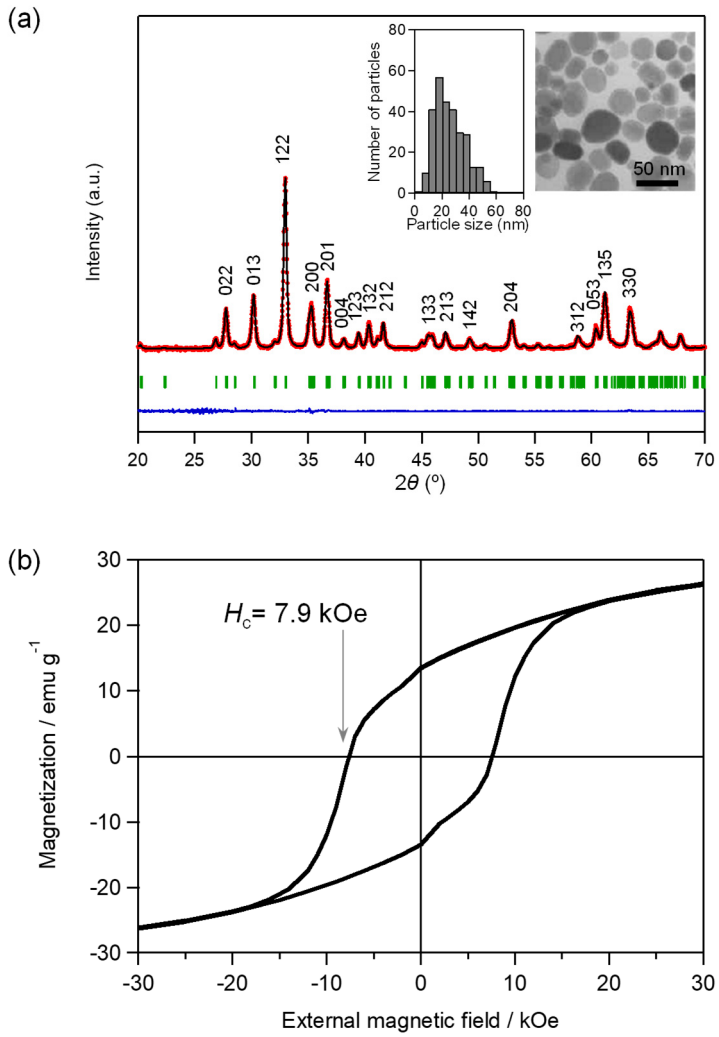

Figure 3.7 (a) Observed (red crosses), calculated (black line), and difference (gray line) of the XRD pattern of ε-$Ga_{0.48}Fe_{1.52}O_3$ and calculated positions of the Bragg reflections (black tick marks). (b) Magnetic hysteresis loop of ε-$Ga_{0.48}Fe_{1.52}O_3$ measured at 300 K. Inset is the millimeter-wave absorption spectrum measured at room temperature. [Copyright 2018 Wiley. Used with permission from Eur. J. Inorg. Chem., 847 (2018).]

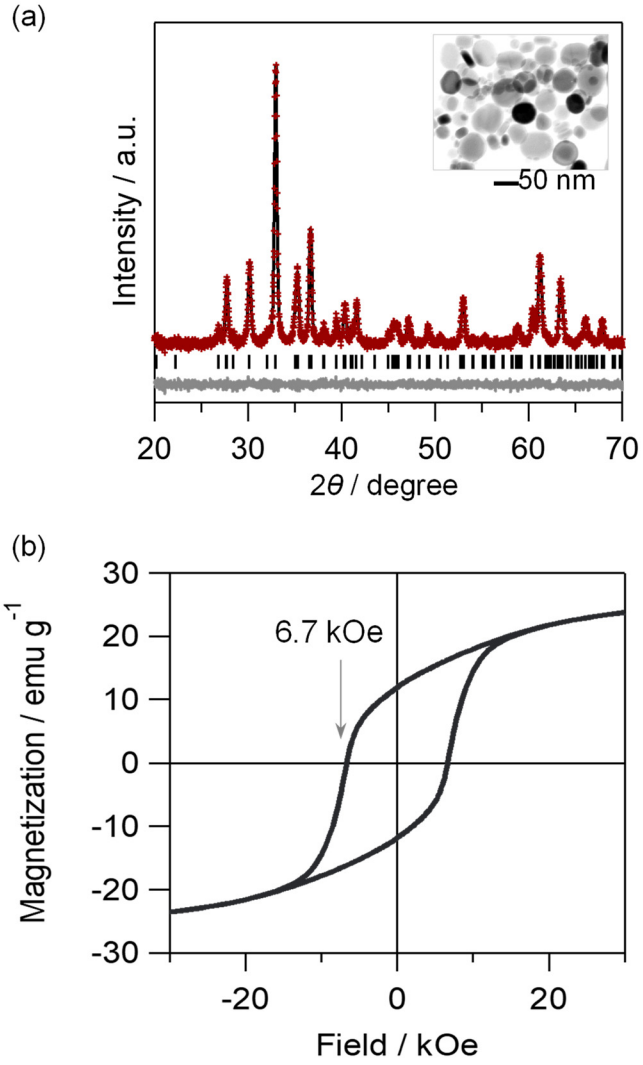

Figure 3.8 (a) Observed (red crosses), calculated (black line), and difference (gray line) of the XRD pattern of ε-$Ga_{0.48}Fe_{1.52}O_3$ and calculated positions of the Bragg reflections (black tick marks). (b) Magnetic hysteresis loop of ε-$Ga_{0.48}Fe_{1.52}O_3$ measured at 300 K. Inset is the millimeter-wave absorption spectrum measured at room temperature. [Adapted with permission from J. Phys. Chem. C, 121, 5812 (2017). Copyright 2017 American Chemical Society.]

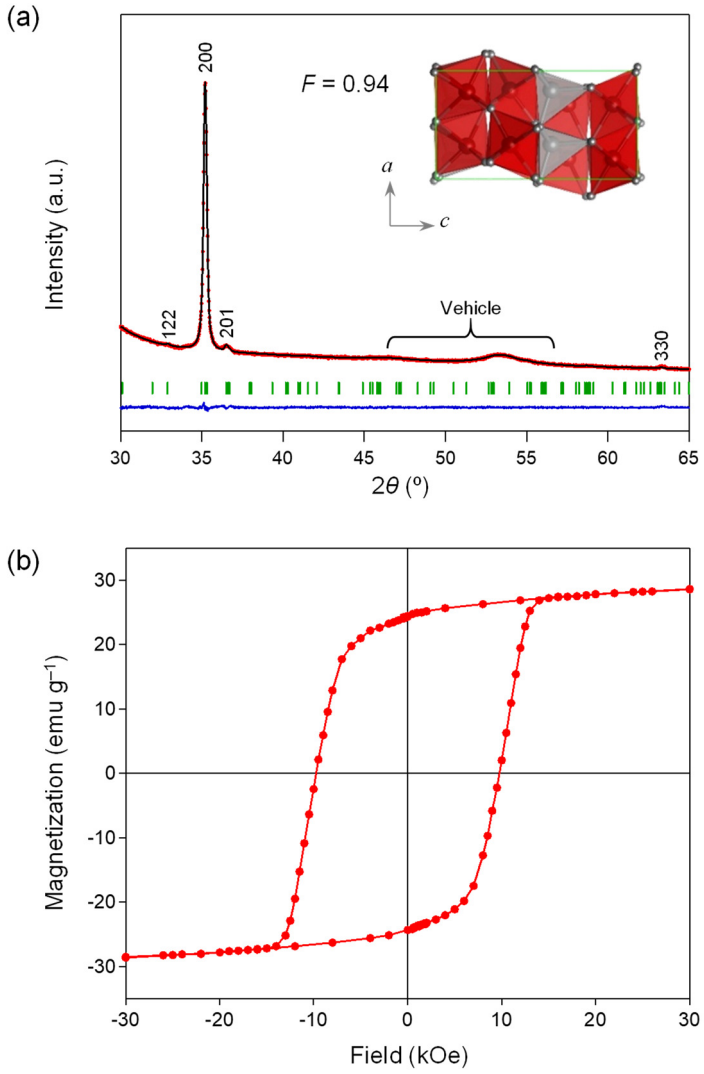

Figure 3.9 (a) XRD pattern and Rietveld analyses of magnetic-field oriented ε-$Ga_{0.45}Fe_{1.55}O_3$ film. Inset is an *a*-axis view of the crystal structure. (b) Magnetization vs. external magnetic field curve of the crystallographically oriented ε-$Ga_{0.45}Fe_{1.55}O_3$ magnetic film (red). [Copyright 2018 Wiley. Used with permission from Eur. J. Inorg. Chem., 847 (2018).]

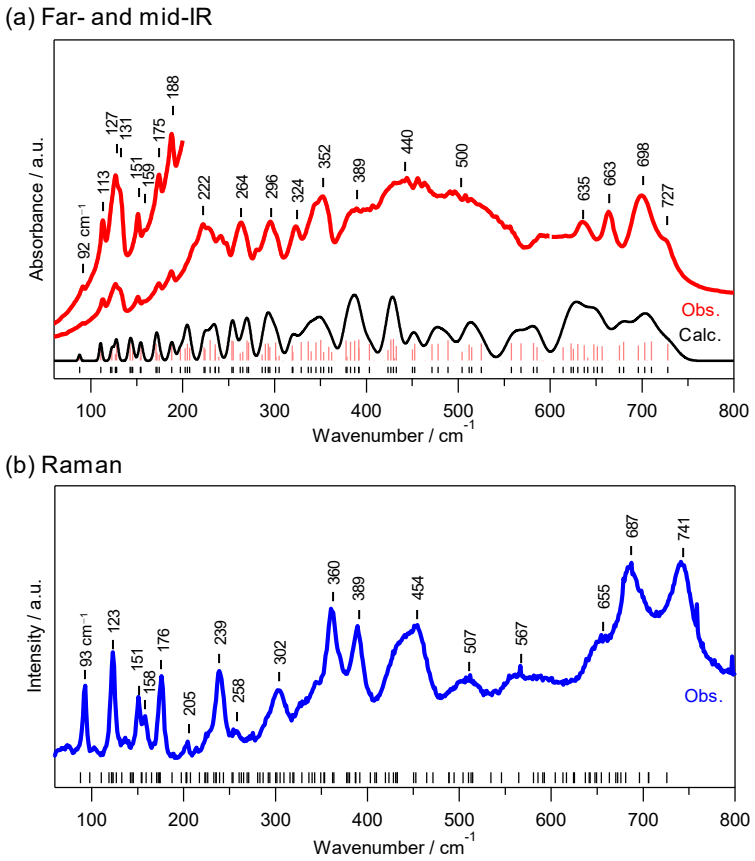

Figure 3.10 (a) Observed (red) and calculated (black) far-IR and mid-IR spectra of ε-$Ga_{0.48}Fe_{1.52}O_3$, positions of IR active modes (black tick marks) and IR intensities (red bars). Far-IR spectrometer measured between 60–600 cm^{-1} and mid-IR measured above 600 cm^{-1}. (b) Raman spectrum of ε-$Ga_{0.48}Fe_{1.52}O_3$ the calculated positions of the Raman active modes (black tick marks). [Adapted with permission from J. Phys. Chem. C, 121, 5812 (2017). Copyright 2017 American Chemical Society.]

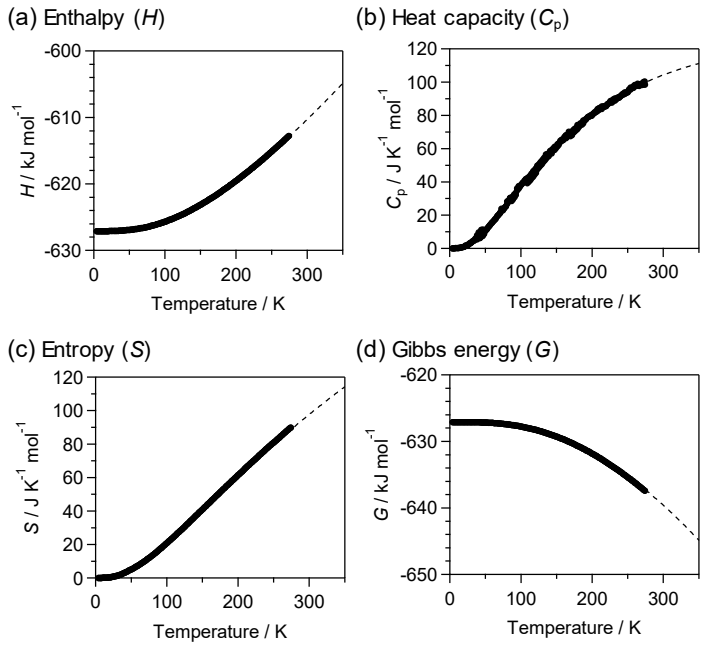

Figure 3.11 (a) Enthalpy (H), (b) heat capacity (C_p), (c) entropy (S), and (d) Gibbs energy (G) of ε-$Ga_{0.48}Fe_{1.52}O_3$ plotted as functions of temperature. Parameters determined from heat capacity measurements where C_p represent the observed data (black dots) and the fitted curve based on the two-Debye model (dotted). H, S, and G are transformed from C_p. [Adapted with permission from J. Phys. Chem. C, 121, 5812 (2017). Copyright 2017 American Chemical Society.]

Chapter 4

Millimeter-wave absorption property of ε-$In_xFe_{2-x}O_3$

Iron oxides are ubiquitous.[4.1–4.4] Because α-Fe_2O_3 (hematite) and γ-Fe_2O_3 (maghemite) are the most abundant minerals on Earth, they are well studied and used in many commercial applications.[4.5,4.6] In contrast, β-Fe_2O_3 and ε-Fe_2O_3 are rare, and research has been hindered by fabrication challenges of pure phases.[4.7–4.9] For example, our group was the first to synthesize of a pure phase of ε-Fe_2O_3 nanoparticles to reveal the huge coercive field at room temperatrure.[4.10–4.13]

Since then, ε-Fe_2O_3 has been intensively studied using diverse techniques, including Mössbauer spectroscopy, neutron diffraction, and X-ray magnetic circular dichroism.[4.14–4.23] ε-Fe_2O_3 exhibits many promising magnetic properties. It displays a gigantic coercive field (H_c) of 20 kOe and has a zero-field ferromagnetic (natural) resonance of 182 GHz. This is the highest zero-field ferromagnetic resonance frequency for a ferromagnetic material.[4.24,4.25]

Besides the aforementioned features, Fe^{3+} ions can be substituted by other metals,[4.26–4.31] drastically expanding its potential for practical applications. ε-Fe_2O_3 nanorods undergo a phase transition from ferrimagnetism to antiferromagnetism upon indium substitution.[4.26,4.27] This chapter reports the synthesis, crystal structure, magnetic properties, and millimeter-wave absorption properties of spherical-type ε-$In_xFe_{2-x}O_3$ nanoparticles.

4.1. Experimental details

The reverse-micelle technique was combined with the sol-gel technique to fabricate

indium-substituted ε-Fe_2O_3 (Fig. 4.1). Cetyl trimethyl ammonium bromide (CTAB, $CH_3(CH_2)_{15}N(CH_3)_3Br$) and 1-butanol in *n*-octane at a molar ratio of H_2O:CTAB = 31:1 were mixed to form two different microemulsion systems. Microemulsion I was an aqueous solution of $Fe(NO_3)_3$ and $In(NO_3)_3$ with a total concentration of 0.50 mol dm^{-3}. Microemulsion II was a 5 mol dm^{-3} NH_3 aqueous solution. Microemulsions I and II were mixed while rapidly stirring, and then tetraethyl orthosilicate ($Si(C_2H_5O)_4$) was added to yield a final ratio of [Si] / [Fe + In] of 1.5. This mixture was stirred for 20 h. After extracting via centrifugation and drying the precipitate, it was sintered at 1000 °C for 4 h in air. Finally, the SiO_2 matrices were etched by a 5 mol dm^{-3} NaOH solution for 24 h at 60 °C.

Samples with different indium substitution rates were prepared. This was achieved by varying the molar ratios of Fe and In ions ([In] / [In + Fe]). The ratios used were 0.025, 0.050, 0.075, and 0.100. The sol-gel method was employed to synthesize the unsubstituted sample.[4.32] Elemental analyses using inductively coupled plasma mass spectroscopy (ICP-MS) confirmed the sample compositions.

Multiple devices were used to measure the properties of $In_xFe_{2-x}O_3$. Transmission electron microscopy (TEM) was used to determine the sample morphology. X-ray diffraction (XRD) measurement and Rietveld analyses were carried out to investigate the crystal structures.[4.33] A superconducting quantum interference device (SQUID) magnetometer was used to determine the magnetic properties. Terahertz time-domain spectroscopy (THz-TDS) was used to evaluate the electromagnetic wave absorption in the millimeter-wave region (30–300 GHz).

Specifically, for THz-TDS, a mode-locked Ti:sapphire femtosecond pulse laser with a time duration of 20 femtoseconds and a 76-MHz repetition rate was used. For TDS,

the output was divided into two: the pump beam and the probe beam. For THz, a dipole-type low-temperature-grown GaAs photoconductive antenna was used as the wave emitter and a bowtie-type one was used as the detector. Placing the sample between a pair of paraboloidal mirrors concentrated the THz wave at the sample location. Adjusting the delay time between the pump and probe pulses changed the temporal waveforms of the electric component.

For the measurements, pelletized samples were used. Each sample was prepared by pressing a powder sample into a 13 mmϕ pellet. The thickness and filling ratio depended on the sample: 3.5 mm and 52.0 vol% (x = 0.04), 3.4 mm and 52.4 vol% (x = 0.09), 3.7 mm and 49.2 vol% (x = 0.13), and 3.6 mm and 49.7 vol% (x = 0.18). The powder sample for x = 0 was put into a paper container with a 4.8-mm thickness and 30% filling ratio. All measurements were performed at room temperature.

4.2. Results and discussion

The indium substitution ratio (x) in $In_xFe_{2-x}O_3$ of this study were 0, 0.04, 0.09, 0.13, and 0.18 from the elemental analyses. TEM images showed that all samples are composed of spherical nanoparticles. The average particle sizes were 29 ± 13 nm (x = 0), 14 ± 6 nm (x = 0.04), 15 ± 6 nm (x = 0.09), 16 ± 7 nm (x = 0.13), and 18 ± 8 nm (x = 0.18) (Fig. 4.1, inset).

The crystal structure of ε-$In_xFe_{2-x}O_3$ is an orthorhombic (space group $Pna2_1$) with four different Fe sites (A–D sites) (Fig. 4.2a). The A–C sites are octahedral (FeO_6), and the D site is tetrahedral (FeO_4) (Fig. 4.2b). Additionally, the samples include a trace amount of the α-phase. As the indium content increases, the cell parameters of ε-$In_xFe_{2-x}O_3$ monotonously increase: a-axis 5.0917 (3) Å (x = 0) → 5.1284 (12) Å (x = 0.18), b-

axis: 8.7857 (5) Å (x = 0) → 8.829 (2) Å (x = 0.18), c-axis: 9.4783 (8) Å (x = 0) → 9.529 (2) Å (x = 0.18). Similarly, the cell volume increases from 424.00 (5) Å^3 (x = 0) to 431.43 (15) Å^3 (x = 0.18) (Table 4.1). Indium substitution is site selective (Fig. 4.1c). In^{3+} prefers Fe^{3+} at the B site. However, substitution can also occur at the A and C sites. For x = 0.13, the occupancy of In^{3+} is 5% (A), 13% (B), 9% (C), and 0% (D) (Table 4.1). The distortion among the sites is reflected by the standard deviation of the Fe–O bond lengths: 0.20 Å (A site), 0.22 Å (B site), 0.11 Å (C site), and 0.10 Å (D site). The A and B sites deviate from the ideal octahedral geometry. Since In^{3+} has a larger ionic radius (0.80 Å) than Fe^{3+} (0.65 Å), it is difficult for In^{3+} to occupy the small tetrahedral D site. Consequently, the distorted octahedral B (or A) site are preferentially occupied.[4.34]

From the magnetic property measurements, the Curie temperature (T_C) decreases as the indium content increases: 500 K (x = 0), 488 K (x = 0.04), 464 K (x = 0.09), 445 K (x = 0.13), and 420 K (x = 0.18) (Table 4.2). However, the saturation magnetization (M_s) decreases as the indium content increases: 17.6 emu g^{-1} (x = 0), 17.1 emu g^{-1} (x = 0.04), 15.5 emu g^{-1} (x = 0.09), 14.7 emu g^{-1} (x = 0.13), and 14.4 emu g^{-1} (x = 0.18). The spin configuration of ε-$In_xFe_{2-x}O_3$ can explain the M_s value. ε-Fe_2O_3 is a collinear ferrimagnet with positive sublattice magnetizations on the B and C sites and negative sublattice magnetizations on the A and D sites (Fig. 4.3).[4.14,4.31] Hence, the nonmagnetic In^{3+} (S = 0) ion mainly replaces the Fe^{3+} (S = 5/2) at the B site, reducing the total magnetization. The coercive field (H_c) at 300 K decreases with increasing x (Fig. 4.4a). H_c is 21.9 kOe (x = 0), 12.2 kOe (x = 0.04), 11.6 kOe (x = 0.09), 7.8 kOe (x = 0.13), and 5.9 kOe (x = 0.18).

The resonance frequency (f_r) in the millimeter-wave absorption spectra (Fig. 4.4b) linearly decreases as the indium content increases (Fig. 4.5a). The resonance frequency (f_r) is 182 GHz (x = 0), 160 GHz (x = 0.04), 143 GHz (x = 0.09), 123 GHz (x = 0.13), and

110 GHz (x = 0.18).

The dependence of the uniaxial magnetic anisotropy constant (K_u) of ε-$In_xFe_{2-x}O_3$ on the indium content can be expressed using H_c and M_s as $K_u = 1.037 \times M_s H_c$ for randomly oriented single magnetic domain particles with uniaxial magnetic anisotropy.[4.35–4.37] As the indium content increases, both the magnetic anisotropy (Fig. 4.5b) and Fe^{3+} occupancy of the B site decrease (Fig. 4.5c). Consequently, Fe^{3+} in the B site is related to K_u. First-principles calculations and molecular orbital calculations both demonstrate that that Fe^{3+} at the distorted B site contributes to the large magnetic anisotropy of ε-Fe_2O_3 .[4.38] The strong hybridization between the Fe 3*d* orbital and the O 2*p* orbital induces a strong hybridization (Fig. 4.5d), leading to a partial charge transfer from the O 2*p* orbital to the Fe 3*d* orbital. This in turn generates orbital angular momentum on Fe, which induces magnetic anisotropy through spin-orbit interactions. Hence, substitution of the B site with nonmagnetic In^{3+} in ε-$In_xFe_{2-x}O_3$ is responsible for the decrease in H_c and f_r.

4.3. Chapter summary

The influences of indium substitution in spherical ε-$In_xFe_{2-x}O_3$ nanoparticles (20-nm average size) on the crystal structure, magnetic properties, and millimeter-wave absorption are examined. For nanoparticles prepared by a reverse-micelle and sol-gel combination technique, In^{3+} selectively occupies Fe^{3+} at the largely distorted B site. As the indium substitution increases, the magnetic properties (T_C, M_s, and H_c) become smaller. In high-frequency millimeter-wave absorption, f_r decreases from 182 GHz (x = 0) to 110 GHz (x = 0.18) because nonmagnetic In^{3+} substitutes for Fe^{3+} at B sites and B sites are important for magnetic anisotropy. In the field of electromagnetic wave

absorbing material,[4.39–4.47] ε-$In_xFe_{2-x}O_3$ has potential in future millimeter-wave wireless communications.[4.48–4.50] The resonance frequency of the sample for $x = 0.09$ is particularly interesting because it corresponds to the 140-GHz window of air in wireless communications.

References

[4.1] D. J. Craik, *Magnetic Oxides*, Wiley-Interscience Publication, London (1975).

[4.2] R. M. Cornell, U. Schwertmann, *The Iron Oxide: Structure, Properties, Reactions, Occurrence and Uses*, Wiley-VCH, Weinheim (1999).

[4.3] K. J. Standley, *Oxide Magnetic Materials*, Clarendon Press, Oxford (1972).

[4.4] K. H. J.Buschow, *Hand Book of Magnetic Materials*, vol. 20, Elsevier, Oxford (2012).

[4.5] I. Dzyaloshinsky, *J. Phys. Chem. Solids* 4, 241 (1958).

[4.6] T. Moriya, *Phys. Rev. Lett.* 4, 228 (1960).

[4.7] R. Zbořil, L. Machala, M. Mashlan, V. Sharma, *Cryst. Growth Des.* 4, 1317 (2004).

[4.8] C.-W. Lee, S.-S. Jung, J.-S. Lee, *Mater. Lett.* 62, 561 (2008).

[4.9] E. Tronc, C. Chanéac, J. P. Jolivet, *J. Solid State Chem.* 139, 93 (1998).

[4.10] J. Jin, S. Ohkoshi, K. Hashimoto, *Adv. Mater.* 16, 48 (2004).

[4.11] J. Jin, K. Hashimoto, S. Ohkoshi, *J. Mater. Chem.* 15, 1067 (2005).

[4.12] S. Sakurai, J. Shimoyama, K. Hashimoto, S. Ohkoshi, *Chem. Phys. Lett.* 458, 333 (2008).

[4.13] S. Sakurai, A. Namai, K. Hashimoto, S. Ohkoshi, *J. Am. Chem. Soc.* 131, 18299 (2009).

[4.14] M. Gich, C. Frontera, A. Roig, E. Taboada, E. Molins, *Chem. Mater.* 18, 3889 (2006).

[4.15] K. Kelm, W. Mader, *Z. Anorg. Allg. Chem*. 631, 2383 (2005).

[4.16] E. Tronc, C. Chaneac, J. P. Jolivet, J. M. Greneche, *J. Appl. Phys.* 98, 053901 (2005).

[4.17] M. Kumoo, J. Rehspringer, A. Hutlova, C. D'Orleans, S. Vilminot, C. Estoumes, D. Niznansky, *Chem. Mater.* 17, 1106 (2005).

[4.18] T. Nakamura, Y. Yamada, K. Yano, *J. Mater. Chem.* 16, 2417 (2006).

[4.19] M. Hermanek, R. Zboril, *Chem. Mater.* 20, 5284 (2008).

[4.20] Y. Kusano, T. Fujii, J. Takada, M. Fukuhara, A. Doi, Y. Ikeda, M. Takano, *Chem. Mater.* 20, 151 (2008).

[4.21] J. Tucek, R. Zboril, A. Namai, S. Ohkoshi, *Chem. Mater.* 22, 6483 (2010).

[4.22] S. Ohkoshi, H. Tokoro, *Bull. Chem. Soc. Jpn.* 86, 897 (2013).

[4.23] J. Tucek, S. Ohkoshi, R. Zboril, *Appl. Phys. Lett.* 99, 253108 (2011).

[4.24] A. Namai, S. Sakurai, M. Nakajima, T. Suemoto, K. Matsumoto, M. Goto, S. Sasaki, S. Ohkoshi, *J. Am. Chem. Soc.* 131, 1170 (2009).

[4.25] S. Ohkoshi, S. Kuroki, S. Sakurai, K. Matsumoto, K. Sato, S. Sasaki, *Angew. Chem. Int. Ed.* 46, 8392 (2007).

[4.26] S. Sakurai, S. Kuroki, H. Tokoro, K. Hashimoto, S. Ohkoshi, *Adv. Funct. Mater.* 17, 2278 (2007).

[4.27] K. Yamada, H. Tokoro, M. Yoshikiyo, T. Yorinaga, A. Namai, S. Ohkoshi, *J. Appl. Phys.* 111, 07B506 (2012).

[4.28] M. Nakajima, A. Namai, S. Ohkoshi, T. Suemoto, *Opt. Express* 18, 18260 (2010).

[4.29] M. Yoshikiyo, A. Namai, M. Nakajima, T. Suemoto, S. Ohkoshi, *J. Appl. Phys.* 111, 07A726 (2012).

[4.30] A. Namai, M. Yoshikiyo, K. Yamada, S. Sakurai, T. Goto, T. Yoshida, T. Miyazaki, M. Nakajima, T. Suemoto, H. Tokoro, S. Ohkoshi, *Nat. Commun.* 3, 1035 (2012).

[4.31] S. Ohkoshi, A. Namai, S. Sakurai, *J. Phys. Chem. C* 113, 11235 (2009).

[4.32] A. Namai, M. Yoshikiyo, S. Umeda, T. Yoshida, T. Miyazaki, M. Nakajima, K. Yamaguchi, T. Suemoto, S. Ohkoshi, *J. Mater. Chem. C* 1, 5200 (2013).

[4.33] F. Izumi, K. Momma, *Solid State Phenom.* 130, 15 (2007).

[4.34] R. D. Shannon, *Acta Crystallogr., Sect. A: Cryst. Phys., Diffr., Theor. Gen. Crystallogr.* 32, 751 (1976).

[4.35] S. Chikazumi, *Physics of Ferromagnetism*, Oxford University Press, New York (1997).

[4.36] J. M. D. Coey, *Magnetism and Magnetic Materials*, Cambridge University Press, New York (2010).

[4.37] H. Kronmüller, S. Parkin, *Handbook of Magnetism and Advanced Magnetic Materials*, Wiley, London (2007).

[4.38] M. Yoshikiyo, K. Yamada, A. Namai, S. Ohkoshi, *J. Phys. Chem. C* 116, 8688 (2012).

[4.39] K. J. Vinoy, R. M. Jha, *Radar Absorbing Materials*, Kluwer, Boston (1996).

[4.40] S. Celozzi, R. Araneo, G. Lovat, *Electromagnetic Shielding*, Wiley-Interscience: IEEE Press, New Jersey (2008).

[4.41] C. M. Watts, X. Liu, W. J. Padilla, *Adv. Mater.* 24, OP98 (2012).

[4.42] Y. Naito, K. Suetake, *IEEE Trans. Magn.* 19, 65 (1971).

[4.43] R. K. Selvan, V. Krishnan, C. O. Augustin, H. Bertagnolli, C. S. Kim, A. Gedanken, *Chem. Mater.* 20, 429 (2008).

[4.44] J. Lee, Y.-K. Hong, W. Lee, G. S. Abo, J. Park, R. Syslo, W.-M. Seong, S.-H. Park, W.-K. Ahn, *J. Appl. Phys.* 111, 07A516 (2012).

[4.45] S. Sugimoto, S. Kondo, K. Okayama, H. Nakamura, D. Book, T. Kagotani, M. Homma, H. Ota, M. Kimura, R. Sato, *IEEE Trans. Magn*. 35, 3154 (1999).

[4.46] Y. Chen, T. Sakai, T. Chen, S. D. Yoon, A. L. Geiler, C. Vittoria, V. G. Harris, *Appl. Phys. Lett.* 88, 062516 (2006).

[4.47] K. A. Korolev, J. S. McCloy, M. N. Afsar, *J. Appl. Phys.* 111, 07E113 (2012).

[4.48] M. J. W. Rodwell, *High Speed Integrated Circuit Technology, towards 100 GHz Logic*, World Scientific, Singapore (2001).

[4.49] K. C. Huang, Z. Wang, *Millimeter Wave Communication Systems*, Wiley-IEEE Press, New Jersey (2011).

[4.50] J. Capmany, M. Novak, *Nature Photon.* 1, 319 (2007).

Figures and Tables

Table 4.1 Rietveld analysis of the crystal structure parameters of ε-$In_xFe_{2-x}O_3$. [Reproduced from J. Appl. Phys., 115, 172613 (2014), with the permission of AIP Publishing.]

		$x = 0$	$x = 0.04$	$x = 0.09$	$x = 0.13$	$x = 0.18$
a (Å)		5.0917 (3)	5.0932 (9)	5.1081 (11)	5.1194 (5)	5.1284 (12)
b (Å)		8.7857 (5)	8.7953 (12)	8.8120 (13)	8.8247 (8)	8.829 (2)
c (Å)		9.4783 (8)	9.4818(10)	9.4953 (10)	9.5163 (7)	9.529 (2)
V (Å^3)		424.00 (5)	424.74 (10)	427.41 (12)	429.92 (7)	431.43 (15)
Rwp (%)		6.66	0.38	0.44	0.42	0.43
S		1.1324	1.1566	1.2590	1.1660	1.1436
In occupancy (%)	A	0	0	3.2 (11)	4.6 (9)	13.1 (8)
	B	0	4.2 (4)	7.4 (6)	12.8 (5)	14.0 (4)
	C	0	3.8 (4)	7.4 (12)	8.6 (11)	8.9 (9)
	D	0	0	0	0	0

Table 4.2 Magnetic properties of ε-$In_xFe_{2-x}O_3$ after calibrating the magnetization values of the ε-phase using the method in Ref. 4.32. [Reproduced from J. Appl. Phys., 115, 172613 (2014), with the permission of AIP Publishing.]

x	T_C (K)	H_c (kOe)	M_s (emu/g)
0	500	21.9	17.6
0.04	488	12.2	17.1
0.09	464	11.6	15.5
0.13	445	7.8	14.7
0.18	420	5.9	14.4

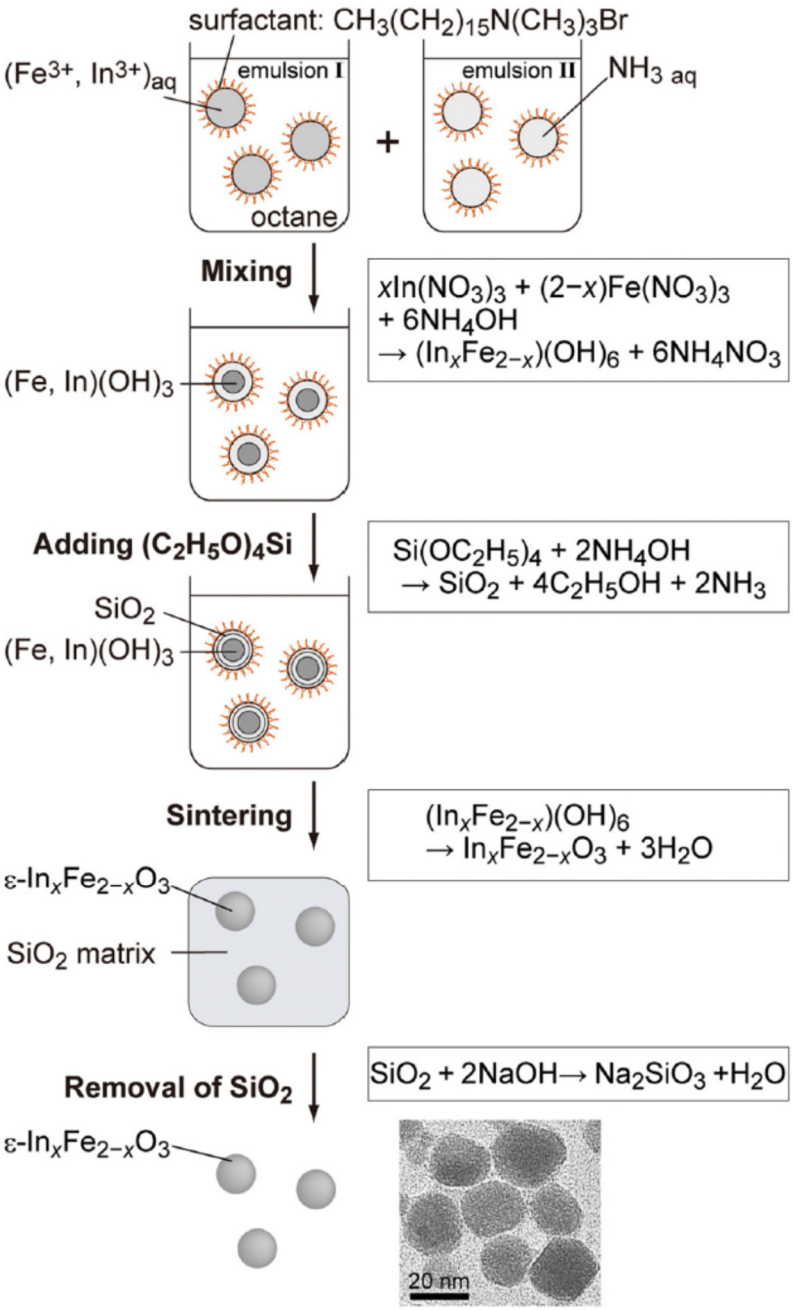

Figure 4.1 Synthesis ε-$In_xFe_{2-x}O_3$. (inset) TEM image of the sample for x = 0.18. [Reproduced from J. Appl. Phys., 115, 172613 (2014), with the permission of AIP Publishing.]

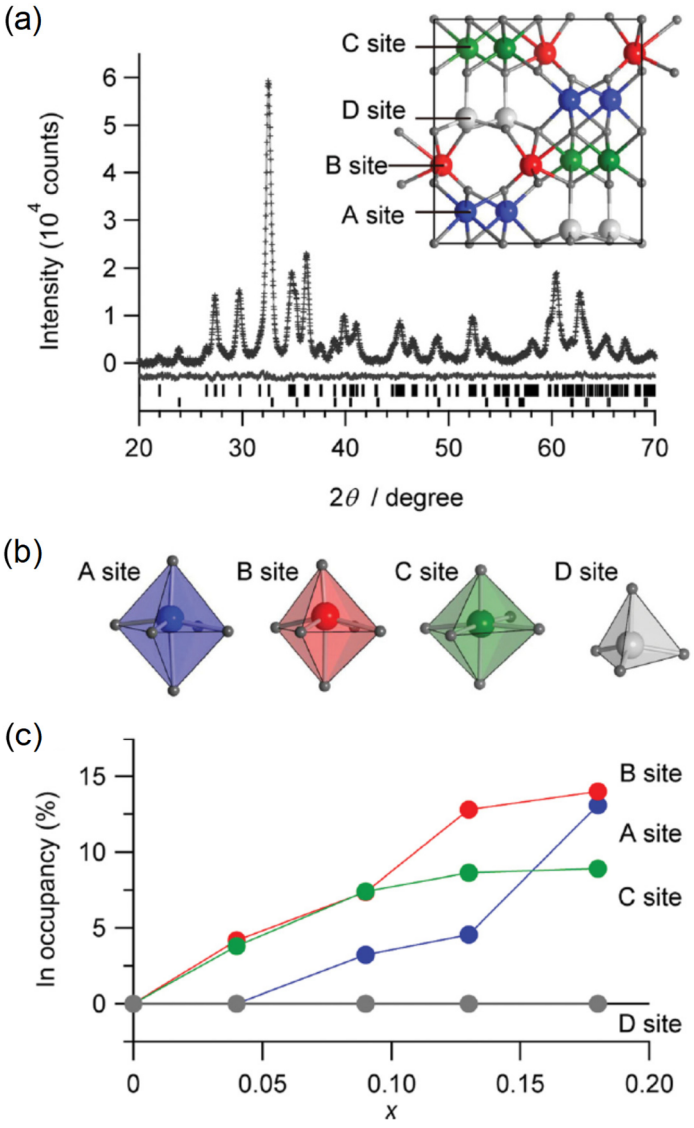

Figure 4.2 (a) Rietveld analysis result of the XRD pattern for x = 0.18 sample. (inset) Crystal structure of ε-$In_xFe_{2-x}O_3$. (b) Surrounding coordination geometry for each Fe site and (c) In occupancy at each Fe site for ε-$In_xFe_{2-x}O_3$ for A (red), B (blue), C (green), and D (gray) sites. [Reproduced from J. Appl. Phys., 115, 172613 (2014), with the permission of AIP Publishing.]

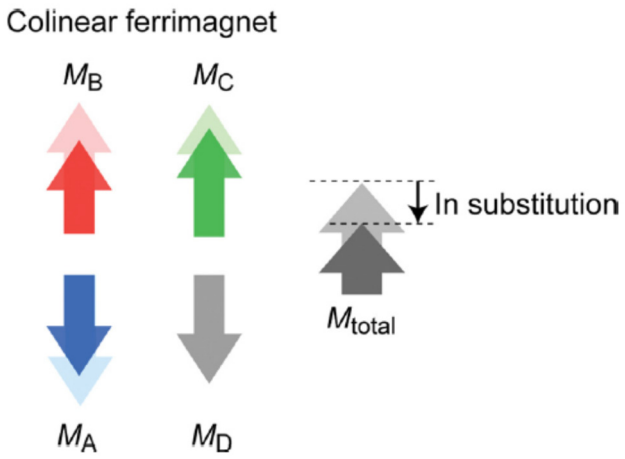

Figure 4.3 Spin configuration of ε-Fe_2O_3 (light arrows) and ε-$In_{0.18}Fe_{1.82}O_3$ (dark arrows) for the sublattice magnetization for A (blue), B (red), C (green), and D (gray) sites and total magnetization (black). [Reproduced from J. Appl. Phys., 115, 172613 (2014), with the permission of AIP Publishing.]

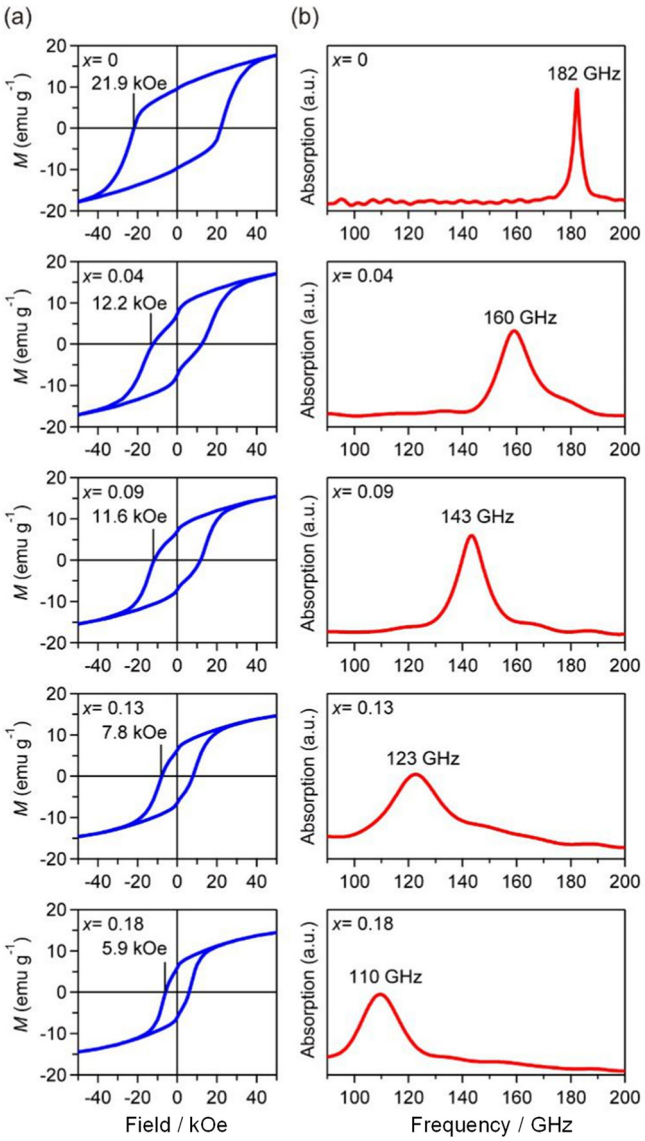

Figure 4.4 (a) Magnetization as a function of external field at 300 K and (b) electromagnetic wave absorption spectra at room temperature measured using THz-TDS. [Reproduced from J. Appl. Phys., 115, 172613 (2014), with the permission of AIP Publishing.]

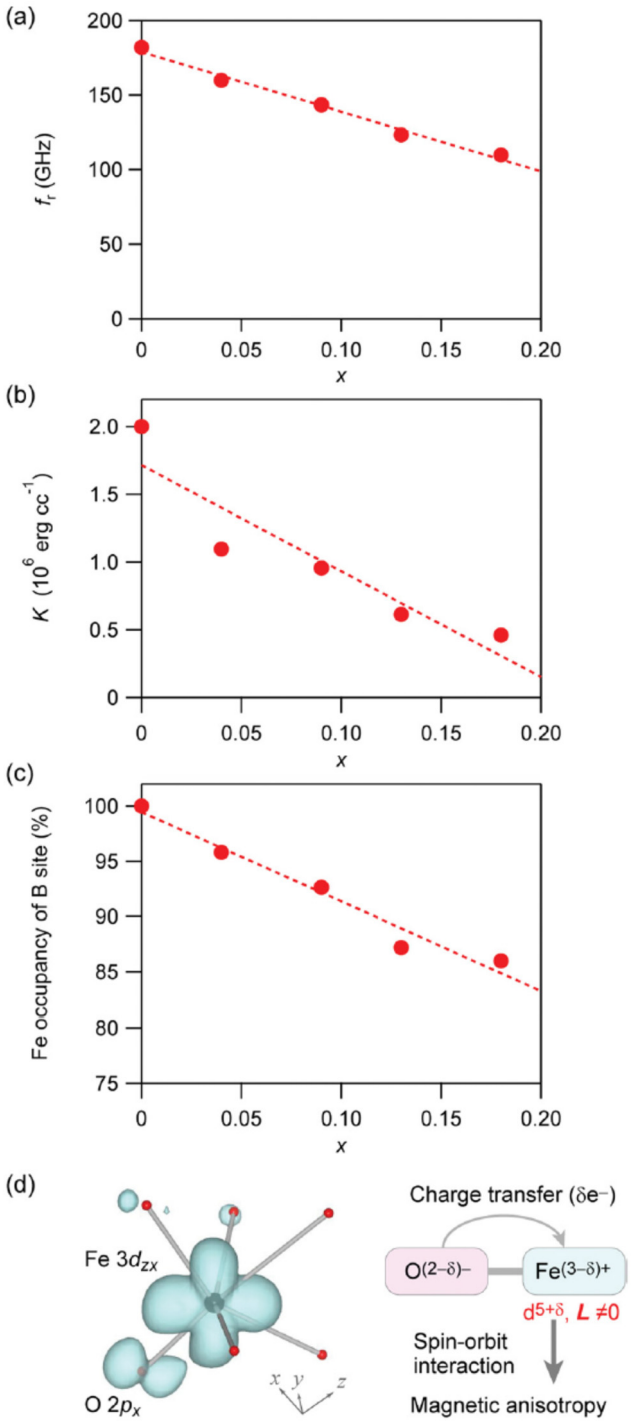

Figure 4.5 (a) Zero-field ferromagnetic resonance frequency (f_r), (b) uniaxial anisotropy constant (K_u), and (c) Fe^{3+} occupancy at the B site as functions of the x plot of ε-$In_xFe_{2-x}O_3$. (d) Charge density map of the Fe 3*d* orbital at the B site hybridizing with the O 2*p* orbital.[4.38] (e) Effect of the hybridization between Fe and O on the magnetic anisotropy. [Reproduced from J. Appl. Phys., 115, 172613 (2014), with the permission of AIP Publishing.]

Chapter 5

Millimeter-wave rotation property of ε-$Al_xFe_{2-x}O_3$

Recently, carrier frequencies for wireless communication devices have been shifting to the millimeter-wave region (30–300 GHz) in order to increase the data transfer rate. For example, when the carrier frequency is 100 GHz, the data transfer rate would be one thousand times faster than that of the Wi-Fi system (2.4 GHz).[5.1] From this angle, millimeter-wave wireless communication technology for 100 GHz is drawing attention.[5.2–5.4] However, currently used magnetic ferrites cannot be applied in such a high frequency region. Our research group observed millimeter-wave resonance of ε-Fe_2O_3 and metal-substituted ε-Fe_2O_3.[5.5,5.6] We have reported the resonance frequency of aluminum substituted ε-Fe_2O_3 (ε-$Al_xFe_{2-x}O_3$) for x = 0.06, 0.09, 0.21, 0.30, and 0.40 using terahertz time-domain spectroscopy (THz-TDS) and for x = 0.49 and 0.66 using backward wave oscillator (BWO) spectroscopy.[5.7,5.8] In this section, we investigated the millimeter-wave absorption and rotation properties of ε-$Al_{0.47}Fe_{1.53}O_3$, which is tuned to resonate at 100 GHz, using THz-TDS.

5.1. Material: ε-$Al_{0.47}Fe_{1.53}O_3$

The target material was prepared by the sol-gel method, based on the previous report.[5.5] A mixed aqueous solution of iron nitride, aluminum nitride, and ammonium aqueous solution was prepared, and tetraethyl orthosilicate was added. The solution was stirred for twenty hours to form a precipitate. The precipitate was filtered, washed, and dried, and then sintered in air at 1100 ºC for four hours. The produced silica matrix around the iron oxide nanoparticles was removed from the calcinated material by chemical

etching using NaOH aqueous solution to obtain the final product as brown powder. Inductively coupled plasma atomic emission spectrometry (ICP-AES) measurement showed that the chemical formula of the sample is $Al_{0.47}Fe_{1.53}O_3$ (calcd: Al, 8.68%; Fe, 58.47%; O, 32.85%; found: Al, 8.52%; Fe, 56.90%; O, 34.58%).

The crystal structure was analyzed by Rietveld refinement of the powder X-ray diffraction (PXRD) pattern, which showed that the sample was composed of a single phase of an orthorhombic structure with space group of $Pna2_1$, the same as ε-Fe_2O_3 (Fig. 5.1(a)). Combined with the elemental analysis result, the sample was characterized as ε-$Al_{0.47}Fe_{1.53}O_3$, and the Al ions selectively occupy the tetrahedral D site among the four nonequivalent Fe sites (A–D). This selectivity is consistent with the Al-substituted ε-Fe_2O_3 reported in the previous literature.[5.7]

The magnetic property was measured using a physical property measurement system (PPMS). The magnetic hysteresis loop at 300 K shows that ε-$Al_{0.47}Fe_{1.53}O_3$ exhibits a H_c value of 10.4 kOe as shown in Figure 5.1(b). The saturation magnetization (M_s) value at 9 T is 29.1 emu g^{-1}, and remanent magnetization (M_r) value is 12.9 emu/g.

5.2. Millimeter-wave absorption

Millimeter-wave absorption property of ε-$Al_{0.47}Fe_{1.53}O_3$ was measured by THz-TDS (Fig. 5.2a). The measurement was carried out using pellet-form samples. The thickness of the pellet-form samples were d = 1.130 mm, 2.339 mm, and 3.549 mm. The filling ratios (V) were 55.4%, 54.5%, and 54.0%, respectively. V is defined as V [volume percent] = (volume of the sample [cm^3])/(volume of the pellet [cm^3]) × 100, and the remaining is air.

Figure 5.3 shows the observed temporal wave form of the transmission THz pulse

light. The reference wave (black dotted line) is the temporal wave form without a sample. With the presence of the ε-$Al_{0.47}Fe_{1.53}O_3$ pellet sample, the main pulse intensity decreases, and the decrease in the intensity became more notable with increasing the pellet thickness increased. The time delay of the THz pulse also became larger with increasing the pellet thickness. From the complex amplitude transmittance obtained by Fourier transformation of the temporal THz waveform, the absorption was calculated by (absorption) = −10 log (transmittance)^2. Figure 5.4 shows the absorption spectra. All of the pellet-form samples show absorption peaks at 100 GHz. It is noted that the raw data has fringe patterns originating from the multiple reflectance within the pellet sample. The raw absorption spectra were analyzed taking into account the multiple reflection (Fig. 5.5). Absorption (A) due to $k = 0$ magnon is expressed as:

$$A = -20 \log|(\{1 - [(\sqrt{\mu_r \varepsilon_r} - 1) / (\sqrt{\mu_r \varepsilon_r} + 1)]^2\} \exp(-2i\pi f d\sqrt{\mu_r \varepsilon_r} / c)) / \{1 - [(\sqrt{\mu_r \varepsilon_r} - 1) / (\sqrt{\mu_r \varepsilon_r} + 1) \exp(-2i\pi f d\sqrt{\mu_r \varepsilon_r} / c)]^2\}| \quad (5.1)$$

, where d, μ_r, and ε_r are thickness, relative magnetic permeability, and relative dielectric constant of the sample, respectively, i is the imaginary unit, and c is the speed of light. μ_r, which is a function of frequency (f), is derived from the Landau-Lifshitz equation[36,37] describing the motion of the magnetization against the intrinsic magnetic anisotropy field of the magnet and the magnetic field of the THz wave;

$$\mu_r' = \mu_r''_{max} \sin\phi\cos\phi + 1 \quad (5.2)$$

$$\mu_r'' = \mu_r''_{max} \sin^2\phi \quad (5.3)$$

$$\phi = \arctan[\Delta f/2(f_r - f)] \quad (5.4)$$

, where f_r is the resonance frequency, $\mu_r''_{max}$ is the maximum value of μ_r'', and Δf is the full width at half maximum of μ_r'' peak.

Figure 5.6 shows the analyzed spectra of the absorption itself after removing the

fringe patterns due to the multiple reflection within the pellet sample. The maximum absorption intensity was 5.4 dB (100.5 GHz) for d = 1.130 mm, 12.8 dB (100.5 GHz) for d = 2.339 mm, and 19.3 dB (100.3 GHz) for d = 3.549 mm. The absorption values are proportional to the normalized pellet thickness. Here, the pellet thickness was normalized to full packing ratio, $d_{100\%} = d \times V/100$. The slope of the fitted line in Figure 5.6 inset corresponds to the absorption intensity per 1 mm thickness (full packing ratio) of 10 dB mm^{-1}.

5.3. Millimeter-wave rotation

Next, to study the millimeter-wave rotation properties, the ε-$Al_{0.47}Fe_{1.53}O_3$ pellet-form samples were magnetized along the out-of-plane direction of the pellet by a pulsed magnetic field of 8 T. After magnetizing, the pellet-form samples had remanent magnetization. Using wire grid polarizers, we performed THz-TDS measurements. As a result, rotation angle and ellipticity of the transmitted THz light was obtained by recording the parallel and perpendicular polarizations.[5.9,5.10] Figure 5.6 shows the ellipticity and rotation angle of the d = 2.339 mm pellet-form sample. Let me show the details of the observed data. When the THz light was irradiated from the N-pole direction of the pellet, the ellipticity showed a peak centering at the resonance frequency with a value of +0.7 at 99.6 GHz. The frequency versus rotation angle shows a dispersive-type behavior centering at the resonance frequency. The minimum and maximum of the rotation angle were −25º at 97.0 GHz and +25º at 102.2 GHz, respectively. On the contrary, when the direction of the poles of the pellet was inverted, the signs of the rotation angle and ellipticity also turned over. Hence, the observed millimeter-wave rotation originates from the direction of the remanent magnetization. That is, the direction of the rotation

depends on the direction of the magnetic poles. Additionally, the ellipticity and rotation angle were proportional to the pellet thickness. From the results of the d = 1.130 mm and 2.339 mm pellets, the ellipticity and the maximum rotation angle of ε-$Al_{0.47}Fe_{1.53}O_3$ per 1 mm thickness (full packing ratio) at 100 GHz were evaluated to be 0.3 mm^{-1}, 11 degree mm^{-1}, and 20 degree mm^{-1}, respectively. As for the pellet of d = 3.549 mm, the millimeter-wave rotation was saturated.

The observed millimeter-wave rotation in this section originates from zero-field ferromagnetic resonance.[5.6,5.10] By the THz light pulse, the spontaneous magnetization is tilted away from the magnetic easy-axis due to the magnetic field component of the THz wave through the gyromagnetic effect. This force generates a precession of the spontaneous magnetization around the easy-axis. The precession causes magnetic rotation of the propagated millimeter-wave and affects the ellipticity and the rotation angle.

5.4. Faraday rotation of ε-Fe_2O_3 dispersed thin film

The rotation phenomenon described in the previous section is caused the magnetic field component of the electromagnetic wave (magnetic rotation). In contrast, the generally known Faraday rotation phenomenon is caused by the electric field component and is observed in the ultraviolet-visible light region. As a reference experiment, I prepared a transparent thin film of ε-Fe_2O_3 and measured the Faraday spectrum.

To fabricate the thin film, an aqueous ammonia solution (25%) was slowly added to an aqueous dispersion of iron oxide hydroxide nanoparticles (3-nm in size). The solution was stirred at 50 °C for 30 minutes. A colloidal solution was formed after adding tetraethoxysilane and stirring for 20 h. The obtained solution was spin-coated at 1000 rpm for 10 seconds onto a quartz substrate. This step was repeated 27 times. After sintering at

1005 °C for 4 h in air, an orange transparent thin film composed of pure ε-Fe_2O_3 nanoparticles in a SiO_2 matrix was formed on a quartz substrate (Fig. 5.8a). To characterize the film, SEM and TEM images were acquired, and XRD measurement was carried out to confirm the crystal structure. A JASCO V-670 spectrometer was used to measure the ultraviolet-visible (UV-vis) spectra, and a JASCO E-250 was used to measure the Faraday effect of ε -Fe_2O_3 in a SiO_2 matrix film at room temperature.

XRD pattern showed that all of the peaks are assigned to ε-Fe_2O_3, except the hollow peak at $2\theta = 21°$ attributed to amorphous SiO_2 (Fig. 5.8b). ε-Fe_2O_3 has an orthorhombic structure (space group $Pna2_1$) with lattice constants of a = 5.079(7) Å, b = 8.821(11) Å, and c = 9.469(7) Å (Fig. 5.8b, inset). According to Scherrer's equation, the estimated particle size is 8.8 ± 0.8 nm. The film thickness and morphology were investigated by SEM and TEM. From the cross-section SEM image, ε-Fe_2O_3/SiO_2 matrix film was found to be 570-nm thick (0.57 μm) with a roughness of 10 nm (0.01 μm) (Fig. 5.9a). Since the film is composed of 27 spin-coated layers, each layer is assumed to be *ca.* 20 nm. The estimated volume of ε-Fe_2O_3 and SiO_2, which is based on the feed ratio between Fe and Si, is 1 : 16. Figure 5.9a (inset) illustrate the ε-Fe_2O_3 in a SiO_2 matrix film. The ε-Fe_2O_3 nanoparticles (*ca.* 9 nm) are homogeneously dispersed in the SiO_2 matrix without porosity (Fig. 5.9b). The SEM and TEM results agree well with the XRD data.

UV-Vis absorption measurement showed that the film of ε-Fe_2O_3 in a SiO_2 matrix has an absorbance of 0.043 at 500 nm (Fig. 5.10). The film shows Faraday rotation around 380 nm, 420 nm, and 500 nm (Fig. 5.11a). The external magnetic field dependence of the Faraday ellipticity at 390 nm exhibited a hysteresis loop with a coercive field (H_c) of 3.0 ± 0.2 kOe (Fig. 5.11b).

5.5. Chapter summary

In ε-$Al_{0.47}Fe_{1.53}O_3$, millimeter-wave absorption at 100 GHz was observed. The absorption was 10 dB (90%) per 1 mm. Additionally, millimeter-wave polarization plane measurement of the magnetized ε-$Al_{0.47}Fe_{1.53}O_3$ pellet showed magnetic rotation. As a reference experiment, Faraday rotation in the UV-visible light region was measured using a film of ε-Fe_2O_3 in SiO_2 matrix. Since ε-$Al_{0.47}Fe_{1.53}O_3$ is economically low cost, a series of Al-substituted ε-Fe_2O_3 is expected to be used as commercial millimeter-wave absorbers or isolators.

References

[5.1] J. Federici, L. Moeller, *J. Appl. Phys.* 107, 111101 (2010).

[5.2] M. J. W. Rodwell, *High speed integrated circuit technology, towards 100 GHz logic*, World Scientific, Singapore (2001).

[5.3] R. D. Paolis, M. Kaynak, *IEEE Microwave and Wireless Components Lett.* 26, 225 (2016).

[5.4] K. S. Lee, Y. S. Kim, Y. K. Hong, Y. H. Jeong, *IEEE Electron Device Lett.* 28, 672 (2007).

[5.5] S. Ohkoshi, S. Kuroki, S. Sakurai, K. Matsumoto, K. Sato, S. Sasaki, *Angew. Chem. Int. Ed.* 46, 8392 (2007).

[5.6] A. Namai, M. Yoshikiyo, K. Yamada, S. Sakurai, T. Goto, T. Yoshida, T. Miyazaki, M. Nakajima, T. Suemoto, H. Tokoro, S Ohkoshi, *Nat. Commun.* 3, 1035 (2012).

[5.7] A. Namai, S. Sakurai, M. Nakajima, T. Suemoto, K. Matsumoto, M. Goto, S. Sasaki, S. Ohkoshi, *J. Am. Chem. Soc.* 131, 1170 (2009).

[5.8] M. N. Afsar, Z. Li, K. A. Korolev, A. Namai, S. Ohkoshi, *J. Appl. Phys.* 109, 07E316 (2011).

[5.9] O. Morikawa, A. Quema, S. Nashima, H. Sumikura, T. Nagashima, M. Hangyo, *J. Appl. Phys.* 100, 033105 (2006).

[5.10] M. Nakajima, A. Namai, S. Ohkoshi, T. Suemoto, *Opt. Express* 18, 18260 (2010).

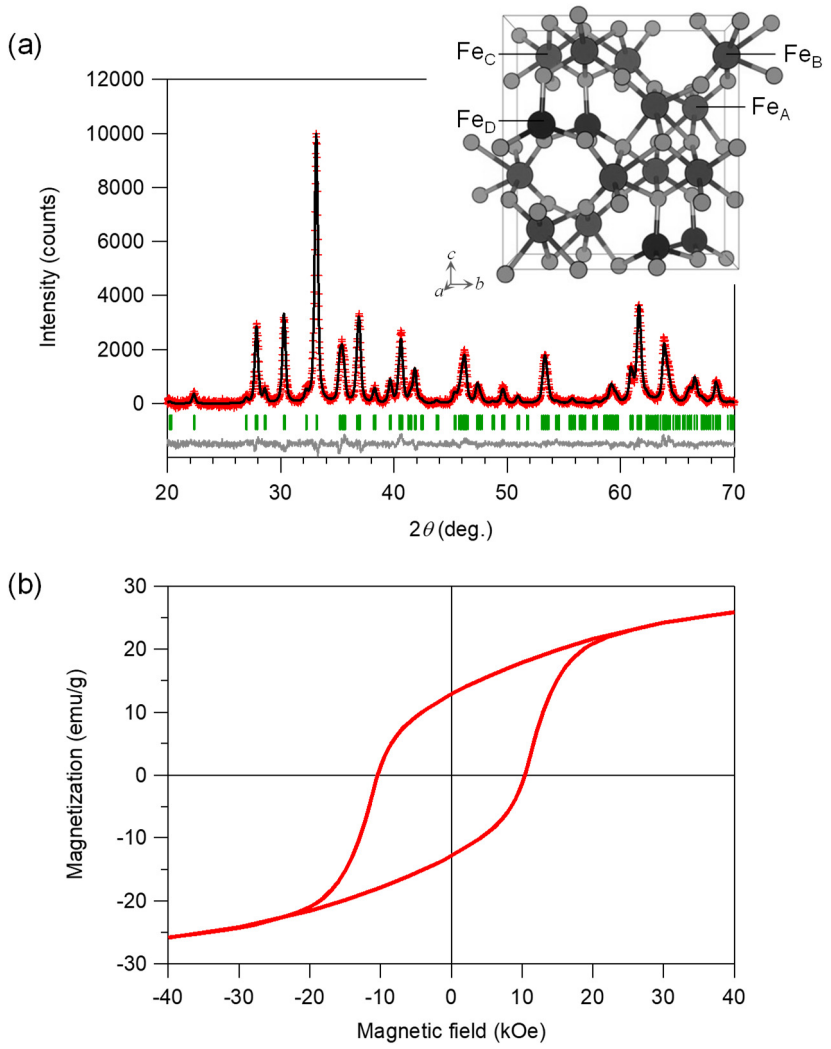

Figure 5.1 (a) PXRD pattern and Rietveld analysis of ε-$Al_{0.47}Fe_{1.53}O_3$. Red marks, black line, and gray line are the observed pattern, calculated pattern, and their difference, respectively. Green tick marks are the calculated positions of the Bragg peaks. Inset is the crystal structure viewed from the *a*-axis direction. (b) Magnetic hysteresis loop of ε-$Al_{0.47}Fe_{1.53}O_3$ at 300 K. [© 2016 IEEE. Adapted with permission from IEEE Magn. Lett., 7, 5506704 (2016).]

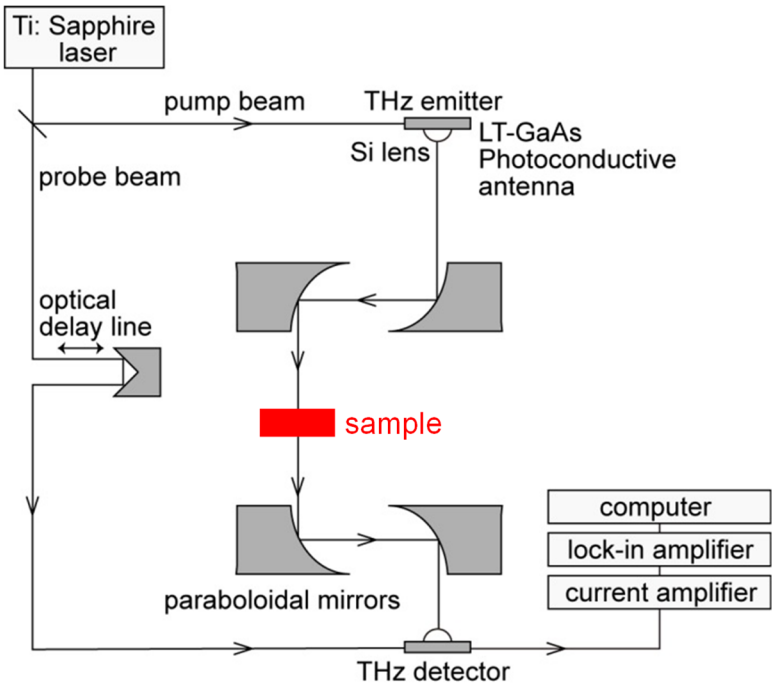

Figure 5.2 Diagram of the terahertz-time domain spectroscopy (THz-TDS) measurement system. [© 2016 IEEE. Adapted with permission from IEEE Magn. Lett., 7, 5506704 (2016).]

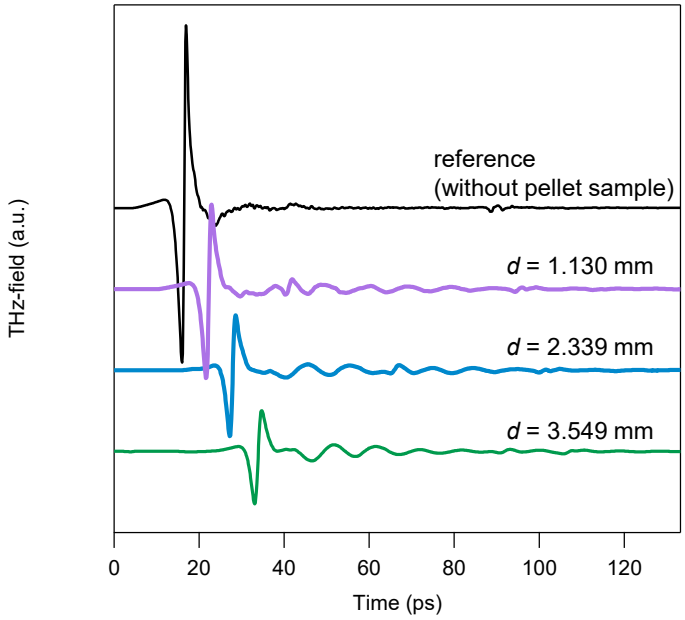

Figure 5.3 Temporal waveforms of the input THz pulse light and the transmitted THz light from the ε-$Al_{0.47}Fe_{1.53}O_3$ pellet samples. [© 2016 IEEE. Adapted with permission from IEEE Magn. Lett., 7, 5506704 (2016).]

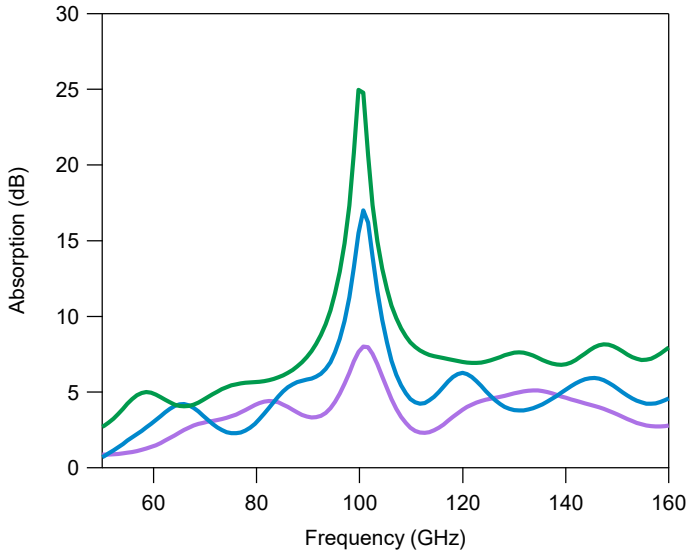

Figure 5.4 Absorption spectra of ε-$Al_{0.47}Fe_{1.53}O_3$ pellet samples for d = 1.130 mm (purple), 2.339 mm (blue), and 3.549 mm (green). [© 2016 IEEE. Adapted with permission from IEEE Magn. Lett., 7, 5506704 (2016).]

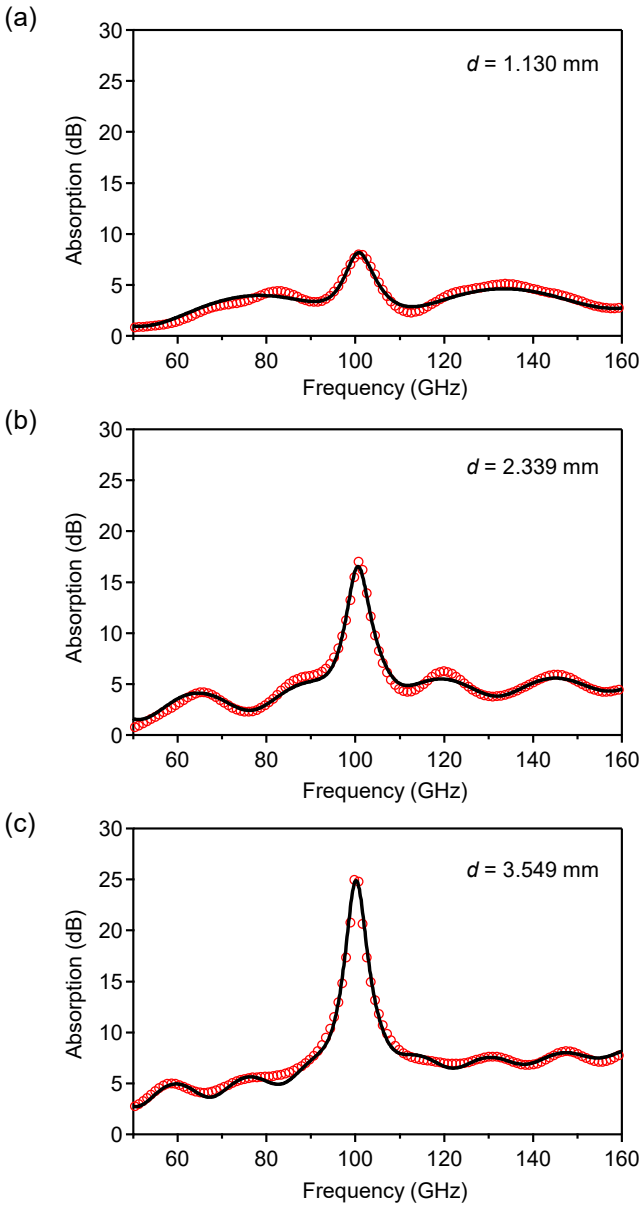

Figure 5.5 Spectral fitting of the absorption of ε-$Al_{0.47}Fe_{1.53}O_3$ pellet samples for (a) *d* = 1.130 mm, (b) 2.339 mm, and (c) 3.549 mm. Red open circles and solid lines indicate the observed spectra and fitted spectra, respectively.

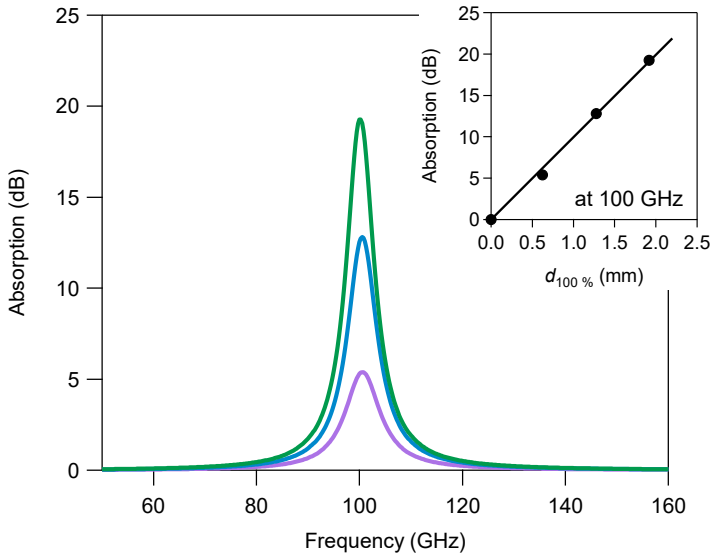

Figure 5.6 Analyzed absorption spectra of ε-$Al_{0.47}Fe_{1.53}O_3$ pellet samples for d = 1.130 mm (purple), 2.339 mm (blue), and 3.549 mm (green). Inset figure shows the absorption intensity at 100 GHz versus sample thickness converted to 100% filling ratio. [© 2016 IEEE. Adapted with permission from IEEE Magn. Lett., 7, 5506704 (2016).]

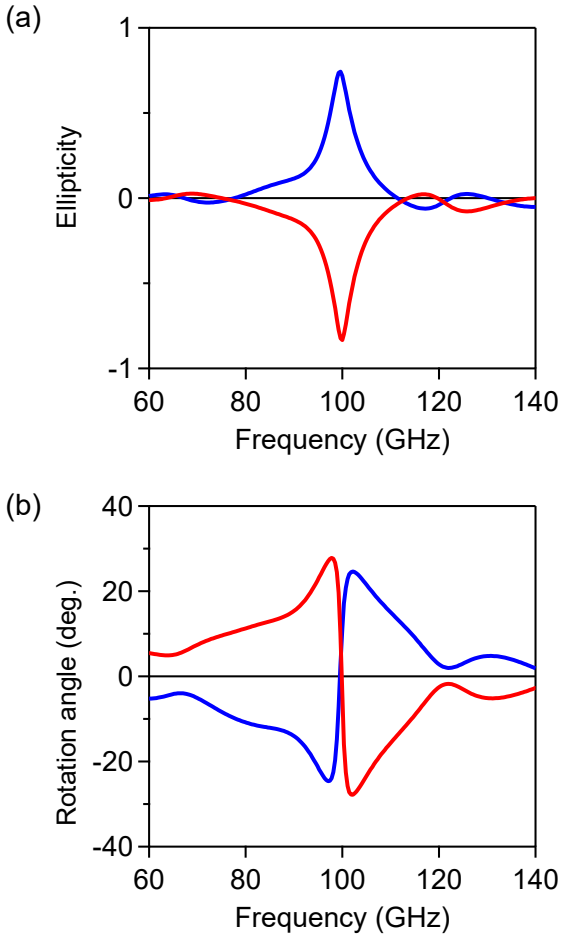

Figure 5.7 Frequency dependence of the (a) ellipticity and (b) rotation angle of the magnetized ε-$Al_{0.47}Fe_{1.53}O_3$ pellet-form samples (d = 2.339 mm). Blue and red lines denote the results measured by irradiating from the N-pole direction and the S-pole direction, respectively. [© 2016 IEEE. Adapted with permission from IEEE Magn. Lett., 7, 5506704 (2016).]

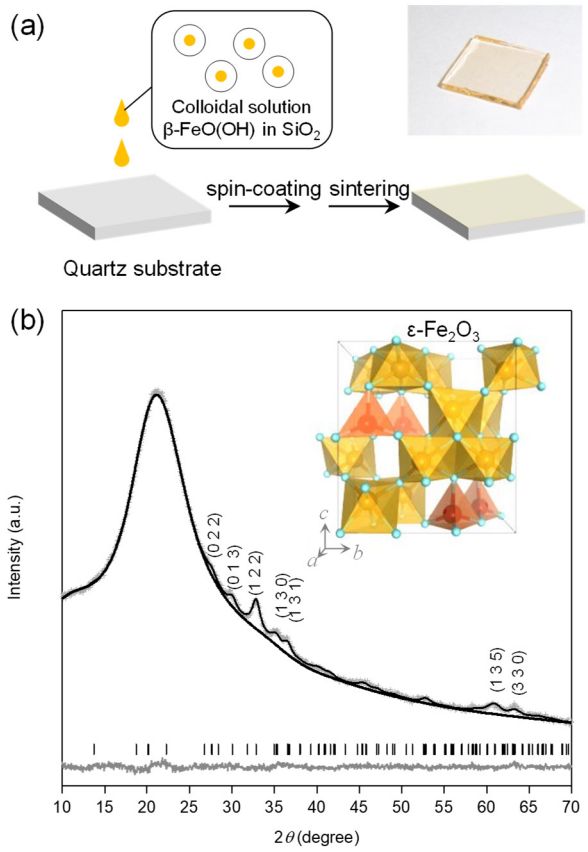

Figure 5.8 (a) Overview of ε-Fe_2O_3/SiO_2 film fabrication and photograph of the film sample. (b) Observed (gray crosses), calculated (black line), and difference (gray line) patterns of the XRD pattern with Rietveld analysis of the ε-Fe_2O_3/SiO_2 film. Additionally, the calculated positions of the Bragg reflections (black bars) and crystal structure (inset) are shown. [Reproduced from AIP Adv., 7, 056218 (2017), with the permission of AIP Publishing.]

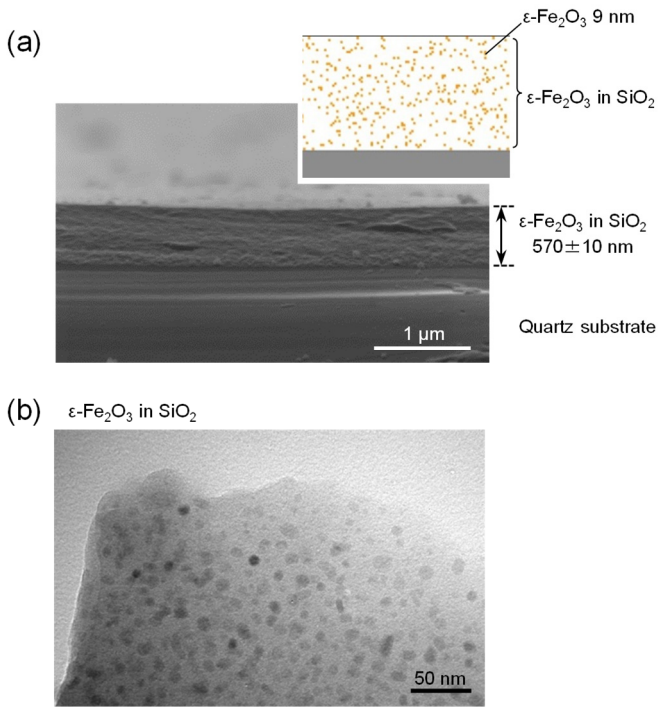

Figure 5.9 (a) Cross section SEM image, (inset) illustration, and (b) TEM image of ε-Fe_2O_3/SiO_2 film on a quartz substrate. [Reproduced from AIP Adv., 7, 056218 (2017), with the permission of AIP Publishing.]

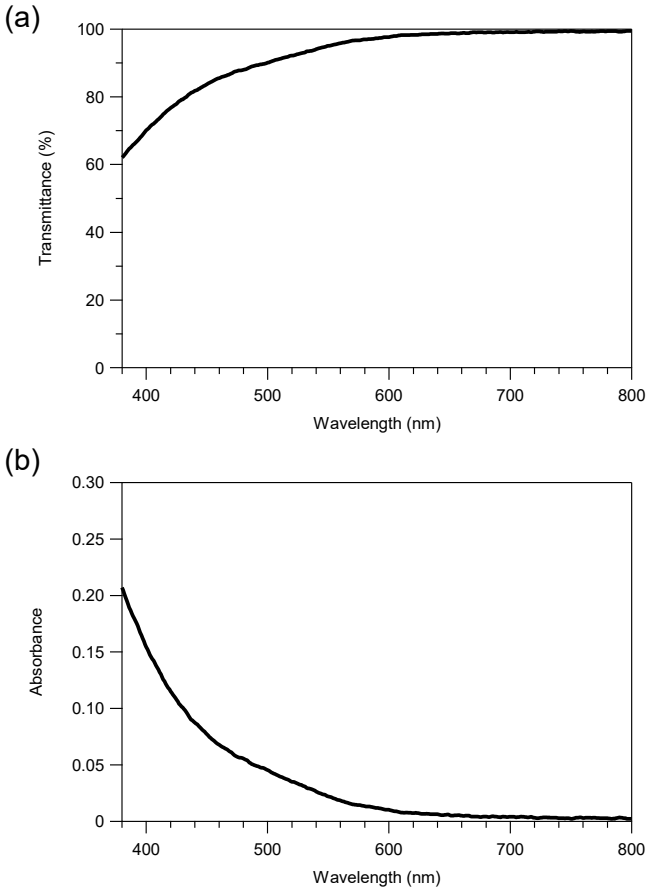

Figure 5.10 UV-vis spectra of the ε-Fe_2O_3/SiO_2 film. (a) Transmittance and (b) absorbance plotted as functions of wavelength. [Reproduced from AIP Adv., 7, 056218 (2017), with the permission of AIP Publishing.]

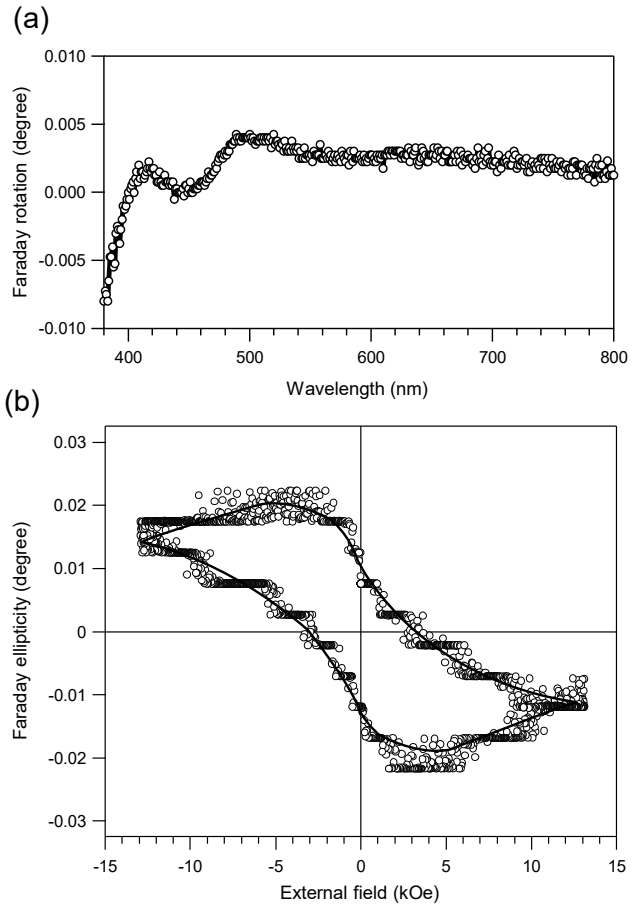

Figure 5.11 (a) Faraday rotation angle spectra for the ε-Fe_2O_3/SiO_2 film. (b) Faraday ellipticity of the ε-Fe_2O_3/SiO_2 film as a function of external field at 390 nm. Black line is to highlight the shape. [Reproduced from AIP Adv., 7, 056218 (2017), with the permission of AIP Publishing.]

Chapter 6

Summary and perspective

The present doctoral thesis focuses on the spectroscopic study of ε-Fe_2O_3 and ε-$M_xFe_{2-x}O_3$ in the range from millimeter-waves to terahertz-waves. Chapter 1 shows the background knowledge concerning ε-Fe_2O_3, which exhibits a huge coercive field at room temperature. This is an exceptionally large value among metal oxide based magnets, and this huge coercivity also enables millimeter-wave absorption at a very high frequency due to zero-field ferromagnetic resonance, so-called natural resonance. Furthermore, several metal-substituted series, ε-$M_xFe_{2-x}O_3$ (M = In, Ga, Al), have been reported, and the magnetic properties and millimeter-wave absorption properties can be widely controlled by metal-substitution. Therefore, this material is expected to be used in future magnetic recordings and electromagnetic wave absorbers. In order to optimize the performance to meet the needs, it is important to understand the fundamental properties of the material from both experimental and theoretical approaches, which had still be underway.

Chapter 2 reports a mesoscopic single crystal bar magnet composed of ε-Fe_2O_3. The atomic movements of ε-Fe_2O_3 were calculated by phonon mode calculations. The lowest frequency phonon mode of 2.51 THz in ε-Fe_2O_3 shows a movement of the Fe atoms oscillating along the crystallographic *a*-axis, which is the growth direction of the bar magnet. The simulated IR spectrum from the phonon mode calculations showed good correspondence with the experimentally obtained far-IR spectrum. The lowest frequency absorption peak was observed at 2.62 THz, corresponding to the A_1 symmetry phonon mode at 2.51 THz.

In chapter 3, first-principles phonon mode calculations of ε-$Ga_{0.5}Fe_{1.5}O_3$ were carried out, which showed 117 optical phonon modes (fundamental vibrations) with symmetries of A_1, A_2, B_1, and B_2, ranging from 2.63 THz to 21.76 THz. The movements of Fe and Ga contribute to the phonon modes in the lower energy region, while the movements of O contribute to the phonon modes in the higher energy region. Far- and mid-IR and Raman spectroscopic measurements confirmed that the calculated spectra agree well with the observed spectra. Additionally, a crystallographically oriented magnetic film was prepared, which showed a rectangular magnetic hysteresis loop with a coercive field of 9.7 kOe.

In chapter 4, the influences of indium substitution on the crystal structure, magnetic properties, and millimeter-wave absorption for spherical ε-$In_xFe_{2-x}O_3$ nanoparticles are described. For nanoparticles prepared by a reverse-micelle and sol-gel combination technique, In^{3+} selectively occupies Fe^{3+} at the largely distorted B site. As the In-substitution increased, the coercive field was found to decrease from 21.9 kOe (x = 0) to 5.9 kOe (x = 0.18). In high-frequency millimeter-wave absorption, the resonance frequency decreased with In-substitution because the nonmagnetic In^{3+} substitutes for Fe^{3+} at B sites, which is considered to be an important site contributing to the magnetic anisotropy of the material. In the field of electromagnetic wave absorbing material, ε-$In_xFe_{2-x}O_3$ has potential in future millimeter-wave wireless communications. The resonance frequency of the sample for x = 0.09 is particularly interesting because it corresponds to the 140-GHz window of air in wireless communications.

In chapter 5, ε-$Al_{0.47}Fe_{1.53}O_3$ was prepared and millimeter-wave absorption property was measured using THz-TDS. An absorption peak due to natural resonance was observed at 100 GHz with an intensity of 10 dB (90%) per 1 mm. In addition, millimeter-

wave polarization plane measurement of the magnetized ε-$Al_{0.47}Fe_{1.53}O_3$ pellet was carried out to obtain the rotation data of the transmitted millimeter-wave. Since ε-$Al_{0.47}Fe_{1.53}O_3$ is eco-friendly and has high durability, a series of Al-substituted ε-Fe_2O_3 is expected to be used as millimeter-wave absorbers or isolators.

As a perspective of the present thesis, spectroscopic study of ε-Fe_2O_3 in the frequency region between terahertz-waves and millimeter-waves is an interesting research direction. Since the millimeter-wave absorption of ε-Fe_2O_3 due to $k = 0$ magnon (0.18 THz) and the optical phonon due to lattice vibration (2.54 THz) are energetically close, ε-Fe_2O_3 is a suitable material for future investigation of the phonon-magnon coupling effect. I would like to plan measurements to observe such coupling effects. Another direction of future research is the investigation of ε-Fe_2O_3 for a new methodology of optomagnetic recording. Considering the fact that ε-Fe_2O_3 is commercialized as a material for magnetic recording and also for high-frequency millimeter-wave absorbers, research development could be further extended by adding the characteristic of millimeter-wave absorption to the magnetic recording technology. Currently, magnetic recording tapes and hard disc drives are facing the "trilemma of magnetic recording," a common issue in the magnetic recording industry. In order to increase the recording density to store the increasing amount of information, there are three important aspects: signal to noise (S/N) ratio, thermal stability, and writability. To increase the S/N ratio, the magnetic particle size must be downsized, but small magnetic particles lose thermal stability. To maintain thermal stability while downsizing, the magnetic anisotropy of the material must be increased. Then, however, the writing head cannot record with the current magnetic field. This trade-off between the three aspects is the "trilemma of magnetic recording." To overcome this challenge, several approaches have been proposed,

e.g., heat-assisted magnetic recording (HAMR). The idea of HAMR is to heat the magnetic media close to Curie temperature so that the magnetization could be flipped by a small magnetic field. In the case of ε-Fe_2O_3, precession or tilting of the magnetization can be triggered by irradiating millimeter-waves. This phenomenon indicates that there is a possibility to inverse the magnetic pole direction by irradiating intense millimeter-wave. Ohkoshi, et al. has recently proposed a new recording method of "focused millimeter-wave assisted magnetic recording (F-MIMR)". To test this methodology, Ohkoshi and his colleagues prepared magnetic films using epsilon iron oxide and irradiated an intense millimeter-wave focused by a metal ring, under an external magnetic field slightly weaker than the coercive field. Magnetic force microscopy (MFM) measurement indicated a magnetic pole flip of the epsilon iron oxide film, proving the concept of this new recording method that could contribute to raising the magnetic recording density in the big data era. Further investigations will be done to introduce this concept to actual applications.

List of publications related to the thesis

1. "Mesoscopic bar magnet based on ε-Fe_2O_3 hard ferrite"
   S. Ohkoshi, A. Namai, T. Yamaoka, M. Yoshikiyo, K. Imoto, T. Nasu, S. Anan, Y. Umeta, K. Nakagawa, and H. Tokoro
   Scientific Reports, 6, 27212/1–10 (2016).

2. "Phonon-mode calculation, far- and mid-infrared, and Raman spectra of an ε-$Ga_{0.5}Fe_{1.5}O_3$ magnet"
   S. Ohkoshi, M. Yoshikiyo, Y. Umeta, M. Komine, R. Fujiwara, H. Tokoro, K. Chiba, T. Soejima, A. Namai, Y. Miyamoto, and T. Nasu
   J. Phys. Chem. C, 121, 5812–5819 (2017).

3. "Highly oriented magnetic film composed of Ga-substituted ε-iron oxide and the angular dependence of the magnetic hysteresis loops"
   M. Yoshikiyo, A. Namai, K. Imoto, H. Tokoro, and S. Ohkoshi
   Eur. J. Inorg. Chem., 847–851 (2018).

4. "High-frequency millimeter wave absorption of indium-substituted ε-Fe_2O_3 spherical nanoparticles"
   M. Yoshikiyo, A. Namai, M. Nakajima, K. Yamaguchi, T. Suemoto, and S. Ohkoshi
   J. Appl. Phys., 115, 172613/1–5 (2014).

5. "Millimeter wave rotation in ε-$Al_{0.47}Fe_{1.53}O_3$ at one hundred gigahertz"
   A. Namai, M. Yoshikiyo, and S. Ohkoshi
   IEEE Magn. Lett., 7, 5506704/1–4 (2016).

6. "Magnetic glass-film based on single-nanosize ε-Fe_2O_3 nanoparticles"
   M. Yoshikiyo, A. Namai, K. Nakagawa, and S. Ohkoshi
   AIP Adv., 7, 056218/1–6 (2017).

Acknowledgements

I would like to express my deepest gratitude to my supervisor, Prof. Shin-ichi Ohkoshi for leading my way into this research on ε-Fe_2O_3. He has looked after my work with tender care and has given me so many advices and suggestions. It is greatly owing to his heartfelt guidance that I am here right now, continuing my career as a researcher in this laboratory. He has given me an invaluable chance and a constant sense of security to take on the challenge in this field. I am always stimulated by Prof. Ohkoshi's pure curiosity and inquisitive mind toward science, and doing research under his supervision is continuing to teach me the great pleasure of doing research. The more I dig into the research, the deeper I understand the significance of our work on ε-Fe_2O_3 and other novel functional materials developed in the group. Especially, ε-Fe_2O_3 is an amazing material with extraordinary physical properties, and I am very grateful to be able to take part in this research. In addition to the fundamental aspect of research on ε-Fe_2O_3, I learned from Prof. Ohkoshi the great joy of working on the development toward industrial applications. Thanks to the chance of participating in the collaboration research, my network of researchers have greatly expanded, and I am stimulated by each member working in different fields. I cannot thank Prof. Ohkoshi enough for this opportunity.

I would also like to give my great thanks to Dr. Asuka Namai for all of the guidance in the research. From the very beginning, when I first started research in Ohkoshi lab for bachelor thesis, she has taught me the basic techniques and the attitude toward research. She has cared for not only my research work but also for my daily life in the group. Even when I am feeling down, she would encourage me and support me to bring myself up. Her presence and working with her has encouraged me many times, and she has always

given me great comfort. This work could not have been done without her support.

I am also thankful to Dr. Koji Nakabayashi, Dr. Kosuke Nakagawa, and Dr. Kenta Imoto of Ohkoshi lab, and Prof. Hiroko Tokoro of Tsukuba University for their scientific guidance and numerous support for this research. They have also greatly supported me as a staff member of the research group.

I would like to give my thanks to Dr. Kouji Chiba of Molsis Inc. for the attentive guidance in the first-principles calculations. I would also like to thank Prof. Tohru Suemoto, Prof. Makoto Nakajima, and Dr. Keita Yamaguchi for their support with terahertz time-domain spectroscopy measurements. I would like to thank Mr. Takeo Soejima for the support with Raman measurements. I am grateful to Mr. Yoshida, and Mr. Miyazaki of DOWA Electronics Materials Co,. Ltd. for the support with sample preparation and for valuable discussions. I am also thankful to all of the Ohkoshi lab members and graduates for their kind support and cooperation.

Last but not least, I would like to thank my family for their heartfelt support.

Marie Yoshikiyo
November 2020